A Hybrid Approach for Nonlinear Soil-Structure Interaction Analysis of Pile-Supported Bridges

by

Hooman Torabi

A thesis submitted to the Faculty of Graduate and Postdoctoral Affairs in partial fulfillment of the requirements for the degree of

Doctor of Philosophy

in

Civil Engineering

Carleton University
Ottawa, Ontario

Abstract

The large-diameter reinforced concrete pile shafts are commonly designed as an economical solution for foundation of highway bridges in soft soils. The substructure method is a widely used technique for seismic SSI analysis of pile-supported bridges due to its remarkable computational efficiency. In the substructure modelling, the complex-valued impedance functions are used to represent the stiffness and energy dissipation characteristics of the soil-pile interaction system. While characteristics of the pile head impedance functions have been decently determined for linear soil-pile interaction, the effects of inelastic interaction on the impedance function still remain unclear. In fact, this study is an attempt to overcome the limitations of linear elastic soil and rigid soil-pile interface bonding assumptions that have been used in substructure analysis.

This thesis aims to develop numerical and analytical frameworks to (i) investigate seismic response of a representative bridge superstructure supported by a large-diameter pile shaft under fully coupled inelastic soil-pile-structure interaction, and (ii) compute the equivalent-linear (EL) pile head impedance functions under the controlled dynamic and earthquake loading modes. Hence, a three-dimensional finite element (FE) model of the soil-pile system, as a rigorous direct method of SSI analysis is developed. The pile shaft lateral capacity is designed following to the AASHTO LRFD guidelines. The developed model is verified using data from centrifuge tests. In order to compute EL impedance functions from the continuum FE model, an algebraic solution is derived for the system of dynamic equilibrium equations in substructure analysis. In this frequency-domain solution, the Fourier transform of the force and displacement values obtained from the time-domain

FE analysis are inserted, while the closed-form solution for the pile head impedance matrix is derived in terms of infinite series.

Results of parametric FE analyses indicate that except for the extreme near-fault motions, the residual structural drift and the pile bending moment of the system would hardly exceed the design limits. The computed EL impedances provide insight into the damping evolution and stiffness reduction due to inelastic interaction over a frequency range of interest. As a key conclusion, it is shown that soil and interface inelasticity can drastically alter the impedance values compared to their fully elastic counterpart.

ACKNOWLEDGEMENTS

I would like to express my gratitude to my research advisor, Dr. Mohammad Rayhani, for his support, guidance, motivation and patience throughout the five years of my doctoral study. I would like to thank Professors Ertugrul Taciroglu from University of California, Los Angeles, Siva Sivathayalan and Dariush Motazedian from Carleton University and Julio angel Infante Sedano from university of Ottawa for serving on my dissertation committee and their insightful comments.

Heartfelt thanks to my parents and little sister for their unconditional love and support through all these years, and finally my greatest appreciation to my wife, Mahshid, for her support, patience, sacrifices and understanding throughout all these years, which enabled me to keep focus on my study.

Dedication

To my family . . .

Table of Content

List of Figures

List of Tables

Vita

B.Sc., Civil Engineering, Sharif University of Technology, Tehran, Iran, 2007.

M.Sc., Geotechnical Engineering, Sharif University of Technology, Tehran, Iran, 2010.

Publications (this study)

- Torabi H., Rayhani M. (2016) "*Comprehensive nonlinear seismic ground response analysis of sensitive clays, case study: Leda clay in Ottawa, Cana*da." Bulletin of Earthquake Engineering.

- Torabi H., Rayhani M. (2014) "*Three-dimensional finite element modelling of seismic soil-structure interaction in soft soil.*" Computers and Geotechnics; 60, PP: 9-19.

- Torabi H., Rayhani M. (2013) "*Finite Element Modelling of Nonlinear Seismic Site Response in Soft Clay*", 66th Canadian Geotechnical Conference. Montreal, Canada.

Chapter 1 : Introduction

1.1. Overview

Evidences from previous earthquakes have shown that bridge structures are vulnerable to severe damage because of potentially defective seismic design. Overturning Hanshin expressway during the 1995 Kobe earthquake as shown in Fig. 1.1 was one of the most catastrophic bridge collapses. Underestimation of seismic demands as a result of neglecting detrimental impacts of the soil-structure interaction (SSI) was identified to be the main cause of the collapse (Mylonakis, 2006). Fig. 1.2 shows the tragic collapse of Cypress street viaduct on the interstate 880 in Oakland, California during the 1989 Loma Prieta earthquake. The main cause of collapse was the Joint shear failures due to inadequate reinforcement in the pier columns. In both case histories, the interaction between bridge foundation and the underlying soft soil resulted in the aggravated seismic shear and displacement demands, which had not been predicted with the traditional seismic design

methods. In fact, these failures highlight the necessity for detailed analysis of the nonlinear interaction between geotechnical and structural components of bridge structures.

Upon an earthquake incident, the soil-structure interaction is defined as mutual effect of vibrational properties of the soil and structure on each other, which has two components: kinematic and inertial interactions. The softer soil supporting the structure-foundation system provides a compliant base which enables foundation to undergo translational and rotational displacement relative to the surrounding soil. As a result, the foundation input motion would be different from the ground surface motion known as free field. This mechanism is referred to as kinematic interaction. The response of the foundation and its surrounding soil may also be significantly altered by the inertial interaction because of the massive inertial forces and moments transferred to the foundation. In fact, these two mechanisms operate in a coupled manner whose accurate estimation requires fully coupled analysis of the soil-foundation-structure system. Since 1970s, significant progress has been made in characterizing the SSI phenomenon. Through these studies, SSI has been shown to modify the system's response in terms of both frequency content and amplitude level, compared to the response of a system with the assumption of the base fixity against relative displacements, which is a common perception in structural engineering community. Generally, SSI leads to period lengthening of the system and reduction or increase of seismic structural demands, pertaining to subsurface soil conditions, seismic site response and frequency content of incident earthquake motion. Accordingly, SSI can be both beneficial and detrimental to seismic performance of structures. Thus, if SSI effects are neglected or poorly estimated, the predicted critical response of the structure would be very approximate and erroneous, which in turn would result in an unsafe or conservative design.

The crucial aspect of any soil-structure system is the dynamic load-transfer mechanism between the foundation and the adjacent soil. Soil-foundation stiffness (force-deformation), energy dissipating mechanisms and interface nonlinearities are the elements that contribute to the dynamic soil-foundation interaction. Radiation and soil hysteretic damping are components of the energy dissipation. The former is highly frequency-dependent and caused by the stiffness contrast at the soil-foundation interface, while the latter damping is frequency-independent, and induced as a result of hysteresis behaviour of the soil. The radiation damping is pronounced at high frequencies and affected by level of soil hysteretic damping and the gap between the soil and foundation.

Generally, the interaction mechanisms involved in the soil-structure systems are simulated using two different approaches, namely continuum modelling and substructure method. In the continuum technique, the whole system of soil-foundation-structure is modelled in a fully coupled manner, providing potentially a rigorous solution for estimation of fully coupled kinematic and inertial interactions. Moreover, the continuum technique bears high fidelity in predicting realistic interaction problems if advanced soil constitutive models and interface elements are implemented in order to capture nonlinear response of the foundation soil and geometrical interface nonlinearities (gap, slippage), respectively. However, development and analysis of such sophisticated continuum model is challenging and computationally expensive. Despite this fact, emerge of high performance computation tools has significantly expedited analysis process of the continuum simulations.

In the substructure method, a set of linear/nonlinear springs and dashpots are used to represent the stiffness and damping of the foundation soil. This would lead to ample reduction of computational effort, which in turn would make this approach appealing to

practice engineers. Substructuring method, pseudo-static and dynamic *p-y* methods (API 2007) are well-recognized approaches in research and practice communities. Gazioglu and O'Neill (1984), Wilson (1998), and Finn (2005) raised concerns on reliability of the API-based *p-y* method in estimation of the seismic pile response. Despite simplicity, these methods involve serious drawbacks mainly attributed to the system uncoupling. Ignoring the coupled effect of inertial and kinematic interactions on stiffness degradation of the foundation soil, uncoupling responses of the soil-foundation in rotational and translational degrees of freedom, and neglecting the soil inertia are the source of uncertainties in these simplified approaches. These deficiencies may result in unreliable estimation of seismic SSI effects in pile foundations embedded in soft clay, due to the large contact area between the pile foundation and its surrounding soil, and also highly nonlinear response of the soft clay. Pile foundations are very susceptible to the coupled effects of soil-structure interaction in soft soils.

While significant research has been devoted to characterizing the seismic soil-pile-structure interaction (SPSI), few has been done on fully coupled nonlinear SPSI with the realistic details taken into account. Interface nonlinearities (gap, slippage), 3D inelastic soil behaviour and the above-ground structural components are critical for the seismic SPSI analysis of infrastructure systems like bridges. Another area which requires special attention is characterizing the coupled equivalent-linear impedance function for pile foundations used in substructure method in order to improve performance of the computationally-inexpensive and simplified approaches for nonlinear SSI analysis.

Figure 1.1. Collapse of Hanshin Expressway Bridge during the 1995 Kobe earthquake, Japan

Figure 1.2. Collapse of Cypress street viaduct of Interstate 880, Oakland, California, during the 1989 Loma Prieta earthquake

1.2. Objectives and Features

In addition to the lack of studies on fully coupled nonlinear SPSI analysis for pile-supported bridge structures, throughout the extensive literature review, the gap in the knowledge of using substructure method for nonlinear SPSI problems was identified. To this end, several studies have assessed seismic response of bridges under influence of the soil-pile-structure interaction through simplified spring methods (e.g., Mylonakis et al. (1997), and Zhang and Makris (2002) using the substructure method, and Hutchinson et al (2001) using the dynamic Beam-on-Nonlinear-Winkler-Foundation (BNWF) approach). Owing to the disadvantages of these methods, described in the previous section, a research study is proposed to evaluate the seismic soil-pile-structure interaction for bridge structures in a more realistic manner. Therefore, this study is intended to evaluate comprehensively the seismic soil-structure interaction for bridge structures supported by deep foundations, with emphasis on detailed concepts underlying the realistic soil-structure interaction phenomenon. The principal issues involved in the soil-pile interaction in soft clay are geometrical and material nonlinearities which are interactive in a coupled manner.

The first objective of this study is to quantify the effects of various components of the coupled nonlinear SPSI on inelastic response of bridge structures sitting on soft clay deposits using the rigorous three-dimensional continuum modelling of the soil-pile system. This investigation is done by conducting a comprehensive parametric study on the key geotechnical and structural components involved in SPSI phenomenon. Furthermore, continuum analysis as a rigorous means of SPSI analysis generates a reliable dataset for approximating the equivalent-linear impedance function. The key features of this part of the thesis can be outlined as follows:

- A verified equation for determination of the small-strain shear modulus (G_{max}) of the Ottawa's soft clay (Leda clay) was proposed based on results from geophysical experiments and cyclic laboratory tests.
- Capability of the employed soil constitutive model and 3D continuum model of the soil-pile interaction are assessed by utilizing the data set from strong ground motion recordings and centrifuge tests.
- Extensive parametric study is carried out to identify influence of the following parameters on the seismic inelastic SPSI for RC shafts: *structural elements*: kinematic constraints at the deck-pier column joint, frequency of the superstructure, and *soil-foundation properties*: frequency content of the soil domain's vibration, boundary condition at the pile tip and soil-pile interface inelsticity.

The second objective of this thesis is to develop a hybrid method for derivation of the equivalent-linear impedance function for the substructure SSI analysis of RC shaft supported bridges. The methodology relies mainly on analytical solution of the substructure formulation in conjunction with closed-form solution of the pile head impedance matrix A large data set generated by the 3D continuum models are used to estimate the equivalent-linear impedance functions. The original features of this part are as follows:

- A simple analytical solution is proposed for coupled analysis of the dynamic equations of motion for the soil-pile-structure system.
- Polynomial approximation of the complex pile head impedance functions is developed.

- The developed hybrid method quantifies effects of soil and soil-pile interface inelasticity on the pile head impedance functions, enhancing capability of the substructure method in simulating nonlinear SPSI problems.
- The equivalent-linear dynamic pile head stiffness and damping are computed under controlled harmonic loadings prescribed at the pile head, representing the structural inertial loads transmitted to the pile head. The harmonic time histories involve variety of frequency content and amplitude range in order to capture the frequency and amplitude-dependent characteristics of the impedance function.
- The hybrid method is applied to a series of complete soil-pile-structure interaction systems under real-world earthquake records in order to compute the impedance function under the coupled inertial soil-structure interaction as seismic waves propagate through the soil domain.

1.3. Organization of the Dissertation

This dissertation consists of seven additional chapters and one appendix. The organization of this dissertation toward achieving the research objectives is outlined as follows:

Chapter 2 provides an integrated literature review of the most relevant research works on existing analytical, numerical and hybrid methodologies for simulation of SSI, with a detailed overview of the substructure modelling approach.

In Chapter 3, ingredients of the finite element platform used for continuum modelling of SSI problem are presented in detail. It begins with an introductory overview of the finite program, followed by explanation of constitutive models used for simulation of inelastic stress-strain behaviour of soil, structural materials and soil-pile interface. This chapter is

concluded by providing an overview on the numerical procedure used for modelling of the soil-pile interaction.

Chapter 4 presents a procedure for calibration of dynamic strength properties of Leda Clay in eastern Canada as a target realistic soil for SSI analysis, based on experimental data. Verification of the proposed equation for variation of small-strain shear modulus with depth is then demonstrated. This is accomplished by conducting a site response model in the finite element framework using recorded earthquake motions.

Chapter 5 describes procedure of developing and validating a 3D finite element model of inelastic soil-pile-structure interaction as well as its application for evaluating seismic response of RC-shaft supported bridges in soft soil. First, validation of the SSI continuum models with results from two sets of centrifuge tests is presented. Second, results of a comprehensive parametric study with focus on detrimental impacts of near-fault ground motions are discussed. The parametric study involves evaluation of the bending moment profile along the pile shaft and the drift ratio of the pier column as the damage criteria for two practical applications of the RC shaft, two types of column-deck joints and different column heights.

Chapters 6 and 7 demonstrate the efforts made to characterize pile head impedances for substructure analysis under inelastic soil-pile interaction. In Chapter 6, scheme of the proposed hybrid approach devised to recover the average equivalent-linear impedances is described. First, the substructure formulations used for analysis of the soil-pile interaction under controlled pile head dynamic loadings and seismic motions are provided. Second, derivation of the closed-form pile head impedance functions and a procedure for polynomial representation of them are demonstrated. Finally, the algebraic solution for

computing the impedances from dynamic equilibrium equation is presented. Chapter 7 presents results of back-calculating the impedances from continuum models of soil-pile interaction using the hybrid approach. Validation of the hybrid approach is demonstrated by comparing results from analytical solutions. The pile head stiffness and damping under the controlled pile head dynamic loading are recovered for a wide frequency range of interest as well as various inelasticity levels. Furthermore, behaviour of the recovered impedances under kinematic and inertial effects of seismic loading is studied.

A summary of the thesis, drawn conclusions and recommendations for future research are provided in Chapter 8.

Chapter 2 : Seismic soil-pile-structure interaction

2.1. Introduction

Pile foundations are widely used in bridges underlain by problematic geological settings like loose sand or soft clay deposits. In design practice, although group piles are usually used for bridges, single reinforced concrete (RC) shaft is used as an end-bearing pile foundation for single or multi-column highway bridges. Due to their large diameter and consequently large cross-sectional moment of inertia, they also provide substantial lateral capacity against lateral loads like earthquake-induced ones. Consideration of soil flexibility as a means of SSI recognition has been suggested by several seismic design codes such as NIST (2012), Caltrans (2013) and AASHTO (2012). However, these design provisions either do not prescribe specific guidelines on how to account for the SSI or suggest a very simplified method which would make the seismic design of bridges very uncertain.

Accordingly, current seismic design practice often ignores SSI effects on basis of the assumption that SSI is beneficial to the bridge response, or the effect of soil flexibility is taken into account using an equivalent-static force-based approach (Song et al., 2006). While this perceived SSI's beneficial role might be valid in stiff soil deposits, several studies have reported detrimental impacts of SSI on seismic bridge response. Mylonakis and Gazetas (2000) showed that SSI has a distinct detrimental influence on seismic bridge response in soft soils by increasing the ductility demand of the bridge pier column. It was also shown that SSI would not necessarily lead to reduction of spectral response of bridge in spite of significant period lengthening of the bridge system caused by the SSI in soft soils. Moreover, they concluded that the dynamic nature of SSI phenomenon, including resonance between input motion, soil and structure cannot be captured by simplified equivalent-static methods. The study by Jeremic et al. (2004) supports this conclusion by showing that the ground motion characteristics plays crucial role in evaluation of the SSI influences. Hutchinson et al. (2001) reported high vulnerability of the RC shaft supported bridges to input ground motions with the long-duration pulses (near-fault motion) using dynamic BNWF analysis.

Considering the importance of SSI analysis as an indispensable part of seismic bridge analysis, it is essential to have deep understanding of the mechanisms underlying seismic soil-pile-structure interaction and the existing approaches for SSI simulation. Basically, two issues must be considered in any soil-pile-structure interaction analysis: first, the technic used to capture soil-pile interaction, second, simulation methodology for seismic soil-pile-structure interaction analysis. To this end, different approaches have been proposed to address these issues, which are discussed in the following sections.

2.2. Direct Modelling of SPSI Problems

Soil-structure interaction problems under seismic and dynamic loadings involve wave propagation in unbounded soil domains where two distinct conceptual domains including near-field which is the structure and its surrounding soil, and far-field which is the semi-infinite soil domain free of the structure's influence. One approach to solve this problem is direct modelling of the entire domain using standard numerical methods such as finite element and finite difference which are referred to as continuum modelling. These methods which allow for coupled simulation of SSI problems solve the following equation of motion over the problem domain by discretizing it in time and space:

$$M\ddot{U} + C\dot{Y} + KY = 0 \tag{2.1}$$

where M, C and K are the mass, damping and stiffness matrices of the whole system, respectively. U denotes the total displacement vector, and Y denotes the relative displacement vector with respect to the reference input motion.

The continuum modelling has been recognized as one of the most rigorous tools for SSI simulation, in particular for inelastic problems where time-varying response of the system is captured by the time-stepping numerical integration of the above equation of motion. For realistic continuum modelling of the inelastic SPSI problem, inelastic soil-pile interface and soil stress-strain behaviour should be taken into account in the simulation. This would require the interface element and elastoplastic soil constitutive models to be adopted in the finite element formulation.

Since it is not possible to model an unbounded domain in the finite element framework, only a truncated soils-structure subdomain is often simulated. Thus, the boundary conditions must be treated appropriately to replicate effects of the truncated unbounded

domain on wave transmission at the boundaries. To the extent of author's knowledge, domain reduction method (DRM) (Bielak et al., 2003 and Yoshimura et al., 2013) has been recognized as the only effective method for reducing the semi-infinite SSI domain of analysis to the near-field domain under remote seismic excitation. In this approach, the semi-infinite domain is partitioned into two subdomains including the near field SSI and the semi-infinite exterior domains by a boundary layer in which the corresponding displacement responses from an auxiliary free filed analysis are stored. However, validity of this method is limited to the linear elastic behaviour of geologic materials in the exterior domain. Thus, one potential application of this approach can be SSI simulation in deep soil deposits with shallow soft material.

To this end, several research have been conducted on continuum modelling of seismic inelastic soil-pile interaction using advanced soil constitutive models. Trochanis et al. (1991) studied effects of soil and interface inelasticity on static and cyclic response of piles using 3D finite element analysis with Dracker-Prager yielding criteria for soil. Elgamal et al. (2008), and Kwon and Elnashai (2008) conducted 3D full scale continuum modelling of nonlinear soil-pile interaction for bridges using kinematic hardening multi-yield surface constitutive model of soil (Prevost, 1978 and1985, Parra 1996). Jeremic et al. (2009) investigated inelastic SPSI problem for a bridge in a non-uniform soil stratum by developing a full scale continuum model with a kinematic hardening elasto-plastic constitutive model of soil. Cheng and Jeremic (2009) developed continuum model of soil-pile interaction in a liquefiable soil using a critical-state based soil constitutive model proposed by Dafalias and Manzari (2004).

2.3. Substructure Modelling of SPSI problems

Dynamic substructuring of SSI problems relies on decomposition of the whole SSI system to its substructure components, assuming linear elastic behaviour of the system. This method which is also known as the three-step method (Kausel et al., 1978), is the most appealing analysis tool in common practice due to its time-efficient procedure. According to Kausel (2010), dynamic substructuring of a SSI system involves: (i) *kinematic interaction*, which determines response of a massless structure and foundation embedded in the soil deposit and subjected to the seismic wave field in the free field soil. (ii) *foundation stiffness (impedance)*, which describes the dynamic force-deformation behaviour at the soil-foundation interface, and (iii) *inertial interaction*, where the response of the structure supported on the impedances from the second step and subjected to the input motion from the first step is determined. This procedure is equivalent to partitioning Eq. 2.1 to the following two matrix equations (Kausel et al., 1978):

$$M_1\ddot{U}_1 + C\dot{Y}_1 + KY_1 = 0 \tag{2.2}$$

$$M\ddot{Y}_2 + C\dot{Y}_2 + KY_2 = -M_2\ddot{U}_1 \tag{2.3}$$

where $U_1 = Y_1 + U_g$, $U = Y_2 + U_1$, $Y = Y_1 + Y_2$ and $M = M_1 + M_2$, M denotes mass matrix of the structure, M_1 denotes mass matrix of the soil domain, and U_g denotes the imposed ground motion vector at the base of the system. Solution to Eq. 2.2 determines response of the system including massless structure to seismic excitation in the free field (kinematic interaction), while solution to Eq. 2.3 determines the response of the system including the massless soil domain to the inertial force ($M_2\ddot{U}_1$) by the structure under the input kinematic

motion from Eq. 2.2. Fig. 2.1 shows schematically the three-step procedure for substructure analysis of a simple soil-structure interaction problem.

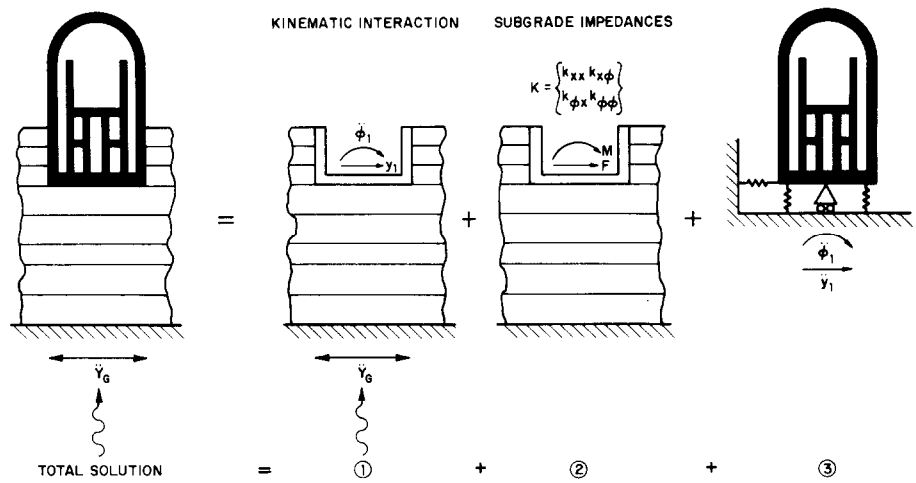

Figure 2.1. Three-step solution for soil-structure interaction analysis (after Kausel et al. 1978)

2.3.1. Semi-discrete substructure formulation

In order to distinguish the definition of foundation impedances in semi-discrete manner, the superposition principle can be used to partition the whole SSI system to its substructure systems including ground with the soil excavation and a simple structure, whose responses are coupled at their boundary as shown in Fig. 2.2. According to Wolf (1985), using finite element formulation, the dynamic equation of motion can be written in frequency-domain for the structure:

$$\begin{bmatrix} S_{ss} & S_{bs} \\ S_{bs} & S_{bb}^{s} \end{bmatrix} \begin{Bmatrix} u_s \\ u_b \end{Bmatrix} = \begin{Bmatrix} P_s \\ P_b \end{Bmatrix} \tag{2.4}$$

where S_{ss}, S_{bs} and S_{bb}^{s} are the internal, coupled and interface dynamic stiffness submatrices of the structure, respectively, u_s and u_b are the total displacement vector of the structural

and interface nodes, respectively. P_s is the external force vector applied to the nodes within the structure, and P_b is the interaction force vector acting at the soil-structure interface. For earthquake excitation within the ground, $P_s = 0$, because the non-interfacial structural nodes are not loaded. In this case, the equation of motion at the soil-structure interface subjected to the scattered seismic motion u_b^g is written as:

$$S_{bs}u_s + S_{bb}^s u_b + S_{bb}^g (u_b - u_b^g) = 0 \tag{2.5}$$

where S_{bb}^g is the dynamic stiffness submatrix of the soil at the soil-structure interface. Combining Eq. 2.5 and Eq. 2.4, the equation of motion for the complete soil-structure interaction under seismic excitation is:

$$\begin{bmatrix} S_{ss} & S_{bs} \\ S_{bs} & S_{bb}^s + S_{bb}^g \end{bmatrix} \begin{Bmatrix} u_s \\ u_b \end{Bmatrix} = \begin{Bmatrix} 0 \\ S_{bb}^g u_b^g \end{Bmatrix} \tag{2.6}$$

In the above equation, S_{bb}^g is referred to as the soil impedance function which is usually frequency-dependent and complex-valued, with the real part representing inertial and stiffness effects and the imaginary part corresponds to the damping effects. Accurate characterization of the soil impedance requires dynamic continuum load-deformation analysis of the foundation in an unbounded soil domain. As evident in Eq. 2.6, with the knowledge of foundation impedance functions, the frequency-domain formulation of a SSI problem allows for determination of the system response through a straightforward algebraic calculation. This results in an exact solution for a linear elastic SSI system. However, the corresponding time-domain formulation of Eq. 2.6 is much complicated than the frequency-domain one, which is (Wolf 1989):

$$\begin{bmatrix} M_{ss} & M_{bs} \\ M_{bs} & M_{bb} \end{bmatrix} \begin{Bmatrix} \ddot{u}_s(t) \\ \ddot{u}_b(t) \end{Bmatrix} + \begin{Bmatrix} P_s(t) \\ P_b(t) + S_{bb}^g(t) * u_b(t) \end{Bmatrix} = \begin{Bmatrix} 0 \\ S_{bb}^g(t) * u_b^g(t) \end{Bmatrix} \tag{2.7}$$

where M_{ss}, M_{bs} and M_{bb} are the internal, coupled and interface mass submatrices of the structure, respectively. P_t is the internal resisting force of the structure, and $(*)$ denotes the convolution integral operator used to calculate the interaction force at the boundary in time domain, which is given as:

$$S_{bb}^g(t) * u_b^g(t) = \int_0^t \left[S_{bb}^g(t-\tau) \right] \left\{ u_b^g(\tau) \right\} d\tau \tag{2.8}$$

The time-domain equation of motion in Eq. 2.7, which is able to account for time-varying properties of a nonlinear SSI system is solved using the conventional time-stepping numerical integration methods. A simplified approach to avoid the tedious work of computing the convolution integral and complexities of the frequency-dependent properties of the impedance functions, is modelling the stiffness of the surrounding soil with a constant-value spring in parallel with a dashpot along each DOF (degree-of-freedom) of the foundation's motion. In this method which is very common in practice, dynamic properties of the coefficients of spring and dashpot are determined by modifying their static values at a specific frequency such as natural frequency of the system or predominant frequency of the input motion (NIST 2012). However, this method cannot be a reliable tool for seismic SSI analysis where interaction between the SSI system and the seismic ground response may render significant frequency-dependent response.

For SSI analysis of structures supported on pile foundations, the subgrade impedance function at the pile head must account for properties of dynamic soil-pile interaction along the active pile length.

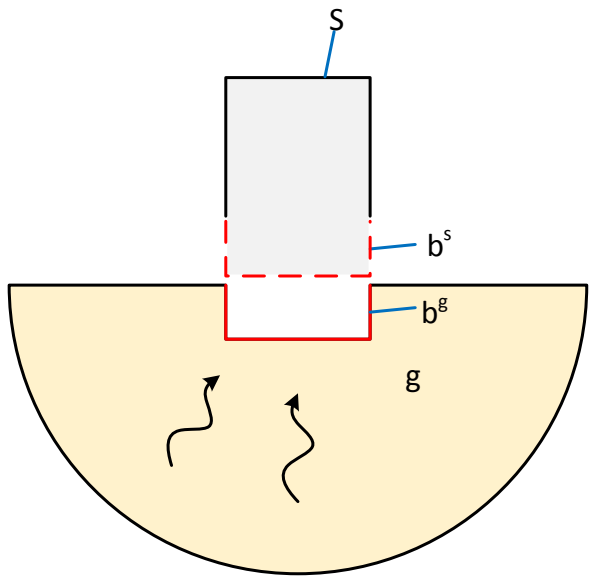

Figure 2.2. Schematic of uncoupled soil-structure system

2.4. Modelling of Soil-Pile Subgrade Impedance

2.4.1. Elastic Continuum

Elastic continuum method in conjunction with the Winkler model has been basis of several studies for modelling the dynamic soil-pile interaction. In this method, the Winkler medium around the pile shaft is represented by a bed of continuously distributed viscoelastic element including linear spring and dashpot as shown in Fig. 2.3, and differential equation of beam-on-dynamic-Winkler foundation (BDWF) is solved in frequency domain. The works of Novak (1974) and Novak and Nogami (1977) were the firsts that adopted this approach to derive closed-form impedances at the pile head. The following studies combined the BDWF approach with finite element analysis in order to determine average soil reaction coefficient in homogeneous and layered soil deposits (Kagawa and Kraft 1980 and 1981, Dobry et al. 1982) and provide equations for the pile head impedance functions in terms of soil-pile stiffness properties (Gazetas 1984, Gazetas

1991). These studies showed that the soil reaction coefficient against pile displacement is affected by pile head loading condition and dependent on the soil-pile relative stiffness as well as pile slenderness ratio. Mylonakis et al. (1999) extended derivation of the closed-form pile head impedances to inhomogeneous multi-layered soil deposit for variety of boundary condition at the pile tip. Most of these researches are based on linear elastic soil behaviour and welded soil-pile interface, which are applicable for modelling the interaction problems in stiff soils under weak motions. The alternative solution for nonlinear problems is modelling the subgrade soil reaction using the beam-on-nonlinear-Winkler foundation (BNWF) in which the soil effect is represented by a series of nonlinear spring.

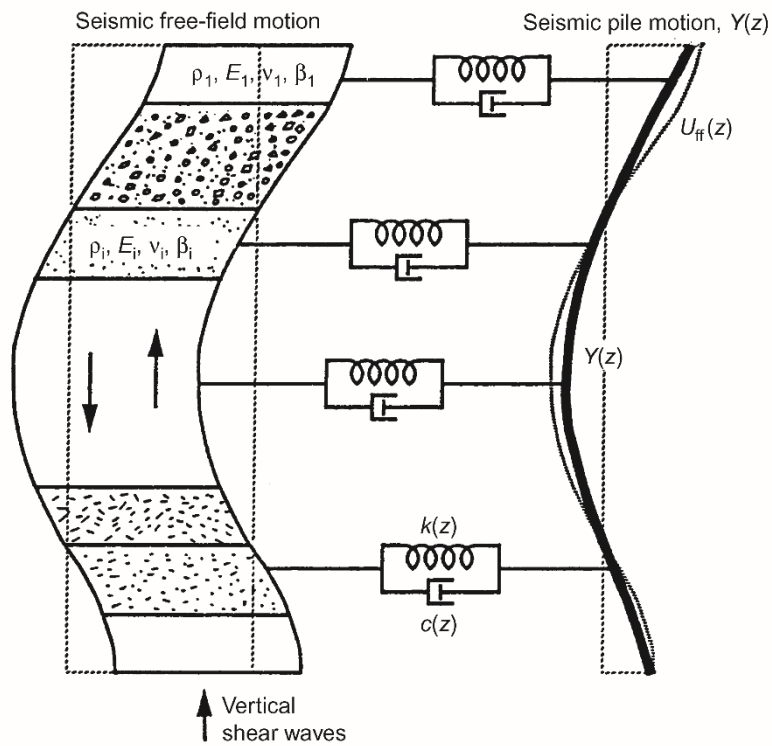

Figure 2.3. Schematic of beam on dynamic Winkler foundation in elastic medium (after Fan 1992)

2.4.2. Nonlinear soil-pile interaction

2.4.2.1. p-y method

Appropriate modelling of soil-pile interaction requires nonlinear springs to represent subgrade reaction and time domain formulation of equation of motion in order to capture time-varying interaction properties, because soil material exhibits nonlinear stress-strain behaviour from very small strain range. The p-y concept has been widely accepted method for lateral pile design in practice, initiated first by McClelland (1956) through processing the results from full scale pile loading tests. He utilized the recorded bending moment profile along the pile length to obtain pile deformation and soil pressure at a given depth. Since this initial work, several full scale experimental works on characterization of p-y concept for piles in sand and clay were undertaken by Cox et al. (1974) and Reese et al. (1975), respectively. Results from these tests combined with theoretical models for mobilization of ultimate lateral soil resistance led to proposing equations for estimation of the depth-varying p-y curves. The empirically-derived p-y method from the above studies has been adopted by the practice code of American Petroleum Institute (API). According to API (2007) provisions, the p-y curve for monotonic lateral loading of a pile in soft clay can be determined using the following equation (after Matlock 1970):

$$\frac{p}{p_u} = \begin{cases} 0.5\left(\dfrac{y}{y_c}\right)^{1/3} & \dfrac{y}{y_c} < 8 \\ 1 & \dfrac{y}{y_c} \geq 8 \end{cases} \tag{2.9}$$

where p_u is the ultimate lateral resistance, $y_c = 2.5\varepsilon_c D$, ε_c is the strain which occurs at one-half the maximum stress at unconsolidated undrained compression test (UU triaxial) of the undisturbed clay samples, and D is the pile diameter. Fig. 2.4 shows the

characteristic shape of the p-y curve for soft clay. For cyclic loading, the ultimate resistance ratio described in Eq. 2.9 is reduced by a factor of 0.72 for $y/y_c \geq 3$ to account for stiffness degradation of the soft clay under cyclic loading.

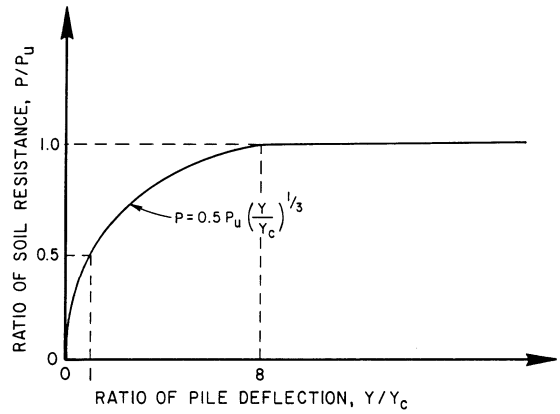

Figure 2.4. Characteristic shape of the p-y curve for soft clay under static loading (after Matlock et al. 1970)

According to API (2007), passive wedge failure and flow failure are the two failure modes of pile lateral capacity, which may occur along the length of the pile. The former dominates shallower depths, while the latter mode takes over at deeper levels with high overburden soil pressure. Therefore, p_u can be estimated using the following equations:

$$P_u = N_p S_u D \tag{2.10}$$

$$N_p = \begin{cases} 3 + \dfrac{\gamma X}{S_u} + J\dfrac{X}{D} & X < X_R \\ 9 & X \geq X_R \end{cases} \tag{2.11}$$

where N_p is ultimate lateral resistance coefficient which varies from 3 at ground surface to 9 at critical depth, S_u is undrained shear strength of clay, X is depth below ground, X_R

is the critical depth where resistance failure mode changes. J is dimensionless empirical constant ranging from 0.25 to 0.5. The intersection depth of two functions in Eq. 2.11 determines the critical depth values as follows:

$$X_R = \frac{6D}{\frac{\gamma D}{c} + J} \tag{2.12}$$

The work of Reese et al. (1975) showed that the characteristic p-y shape for piles in stiff clay exhibits highly strain-softening even under monotonic loading because of brittle nature of its stress-strain behaviour.

In addition to API (2007), several other design codes such as AASHTO (2012), and Canadian Foundation Engineering Manual (CFEM) recommend use of p-y curves for lateral pile design. Although the recommended backbone *p-y* curves are widely popular in practice, several researchers have raised concern on their reliability for different soils, piles and loading conditions. Gazioglu and O'Neill (1984) studied 30 full-scale pile load tests in cohesive soils; 21 static and 9 slow cyclic tests, and concluded that API recommended *p-y* curves are not adequate for even static lateral pile analysis, giving poor confidence in simulation of bending moments and pile displacement with depth. Murchison and O'Neill (1984) came to similar conclusion about the reliability of the *p-y* curves for cohesionless soils by performing 24 full-scale tests. The limitations of API p-y curves in representation of realistic backbone *p-y* curve for dynamic soil-pile interaction can be summarized as follows:

- *Experimental factors*: firstly, the empirical API curves have been derived from field tests in specific type of soils, and thus, extending their application to other

type of soils may produce erroneous results. Secondly, due to static or slow-cyclic loading condition of these tests, the derived p-y curves cannot appropriately represent pile lateral resistance mainly in clays under high frequency seismic motion, because the ultimate shear strength of cohesive soils increases with increasing loading frequency.

- *Analytical assumptions*: this source of limitations arises from inherent assumption of the Winkler model, with the most obvious missing mechanism which is inability to capture shear transfer between adjacent soil layers. Moreover, using the beam differential equation to obtain displacement and soil pressure from the experimental bending moment profile renders *p-y* curve at a given depth dependent on the kinematic constraints at the pile head.

2.4.2.2. Macro-element Approach

The API proposed nonlinear *p-y* springs are widely practiced for seismic analysis of soil-pile interaction though proven to be unreliable even for static problems. Presence of radiation damping and interface nonlinearities in dynamic soil-pile interaction renders these springs inadequate for realistic estimation of seismic soil-structure interaction under earthquake loadings. Matlock and Foo (1978) developed a BNWF method by incorporating discrete elements with gapping and radiation damping capabilities to the nonlinear Winkler foundation model. This method utilizes a time domain finite difference solution in which depth-varying time histories obtained from ground response analysis are input to the end nodes of the nonlinear soil support. Novak and Sheta (1980) were the first introducing the notion of dividing soil domain around the pile foundation into cylindrical near field (weakened) and far field zones to account for soil nonlinearity developed in the soil domain

adjacent to the pile. The following studies by Nogami et al. (1988, 1992) developed a complementary hybrid interaction model comprised of far field/near field soil macro-elements. The viscoelastic far field element consisted of three parallel Kelvin-Voight spring-dashpot elements, representing infinite elastic free field soil domain. The far field macro-element was then connected in series to the near field macro-element comprised of parallel nonlinear springs and elastoplastic interface element for simulation of gapping.

Badoni and Makris (1995) proposed a macro-element consisted of nonlinear spring and linear dashpot combined in parallel to simulate dynamic soil-pile interaction. The force-deformation behaviour of nonlinear spring was prescribed by the Bouc-Wen viscoplasticity model. Using similar constitutive model, Gerolymos and Gazetas (2005) developed a rigorous macro-element capable of capturing more of complex phenomena involved in the coupled soil-pile interaction. The feature of their proposed element is accounting for coupling between the radiation damping and soil-pile interface nonlinearity (gap) and hysteretic soil behaviour. They utilized finite element approach to solve differential equation of BDWF method in time domain. Elnaggar and Novak (1995) proposed a two-part macro-element for representing soil reaction in nonlinear lateral pile analysis. In this model, soil nonlinearity is modelled by a nonlinear spring with the stiffness approximated by the weakened zone idea of Novak and Sheta (1980).

Wang et al. (1998) evaluated the effect of configuration of the linear dashpot in a macro-element comprised of linear and nonlinear springs in series on modelling the nonlinear soil-pile interaction. By comparing the results of numerical analysis and experimental centrifuge test, they concluded that use of the linear dashpot in parallel with the nonlinear spring as shown in Fig. 2.5 results in significant overestimation of radiation

damping in the system. The reason is that the dashpot coefficient which is based on elastic soil properties must be updated for the effect of inelastic interaction on radiation damping.

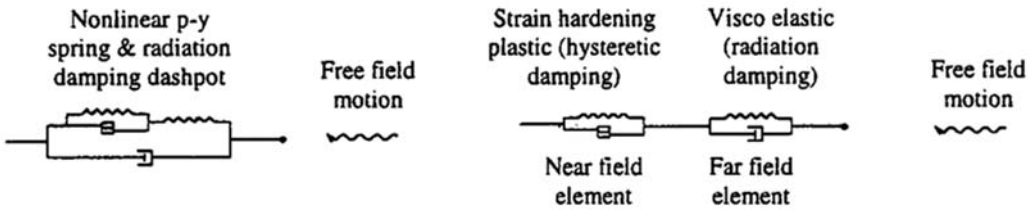

Figure 2.5. Two configurations for use of dashpot for simulation of radiation damping in a macro-element (after Wang et al. 1998)

Boulanger et al. (1999) proposed a macro-element model comprised of elastic, plastic and gap components in series for more realistic simulation of *p-y* behaviour. The elastic component consists of a linear spring in parallel with a linear dashpot to simulate the radiation damping in the far field soil. The plastic component is a nonlinear spring with an initial range of rigid behaviour (elastic range) between $-C_r P_{ult} < P < C_r P_{ult}$ where $C_r =$ ratio of P/P_{ult} when plastic yielding first occurs in the virgin loading. The recommended values of C_r are 0.35 for soft clays and 0.2 for sands. This rigid range of C_r with the total size of $2C_r P_{ult}$ remains constant and translates with plastic yielding (kinematic hardening). Finally, the gap element consists of a nonlinear drag element in parallel with a nonlinear closure element, which are used to simulate the residual drag force on the pile sides and smooth transition in the load-displacement behaviour as the gap opens or closes, respectively. Fig. 2.6 shows configuration of the proposed macro-element and the force-deformation characteristics of the corresponding subcomponents. The performance of this macro-element was then evaluated by results of centrifuge SPSI tests for a single pile (Boulanger et al. 1999) and for a group pile (Curras et al. 2001). It was also used by Hutchinson et al.

(2001) for comprehensive evaluation of seismic performance of extended RC shafts supporting highway bridges, and by Brandenberg et al. (2007) to simulate response of piles in liquefiable and laterally-spreading grounds.

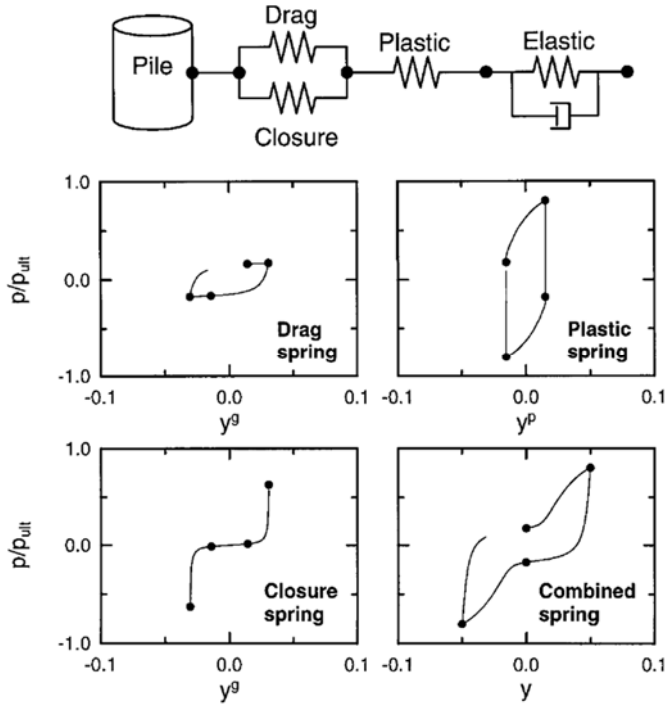

Figure 2.6. Configuration of the macro-element proposed by Boulanger et al. (1999), and force - deformation characteristic curve for each of the sub-elements

Taciroglu et al. (2006) proposed a robust macro-element for inelastic soil-pile interaction of embedded piers and large-diameter piles under cyclic loads, consisting of three sub-elements in parallel, including drag, leading-face and rear-face element as shown in Fig. 2.7. Each of these sub-elements is assembly of basic elements which capture specific aspect of soil-pile interaction. The leading-face element which is used to model the inelastic soil response along the positive pile head loading, is developed by assembling a gap element and an elastoplastic p-y element in series. The strength envelope of the element follows the p-y curves by the API guidelines for clay. The force-deformation behaviour of

the element is elastoplastic under compression while it behaves completely rigid under tension. The assembly of the rear-face element is identical to the leading-face element, but, it acts in the opposite direction to model the other side of the soil-pile interaction. Finally, the drag element is used to simulate frictional forces along the soil-pile interface. Its governing equation follows the one-dimensional classical, rate independent and elasto-perfectly plastic rules.

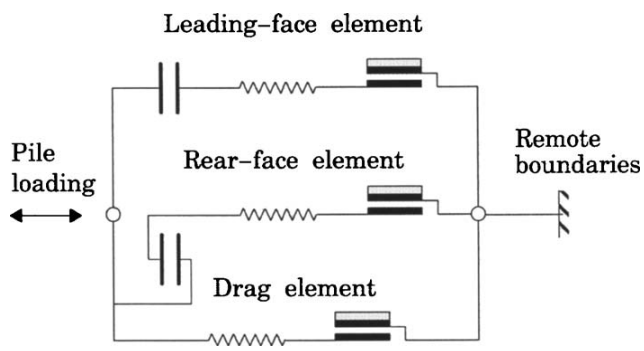

Figure 2.7. Configuration of the macro-element proposed by Taciroglu et al. (2006)

2.5. Application of Substructure Analysis

To this end, substructuring method has been used for seismic response analysis of several bridge structures supported by pile groups. For simplification, these analyses were carried out based on either linear elastic soil behaviour or equivalent linearization of nonlinear *p-y* curves. Makris et al. (1994) performed seismic response analysis for a two-span painter street bridge in northern California using analytical solution of the substructure idealization of bridge foundation in frequency domain. The foundation dynamic impedances were derived using available semi-analytical equations based on linear elastic soil-pile interaction. With a similar modelling approach, Mylonakis et al. (1997) conducted frequency and time domain substructure analyses to elucidate the crucial roles of radiation

damping and rotational component of kinematic input motion on seismic response of bridges supported by a single pile shaft and a group pile in soft soil.

Zhang and Makris (2002) conducted a systematic parametric study using a 3D stick model to identify effects of soil-pile-structure interaction on modal seismic response of the Meloland road overcrossing. The soil-pile interaction was modelled by substructuring the group pile as shown in Fig. 2.8, for which the impedances were derived in a similar fashion to the above mentioned studies.

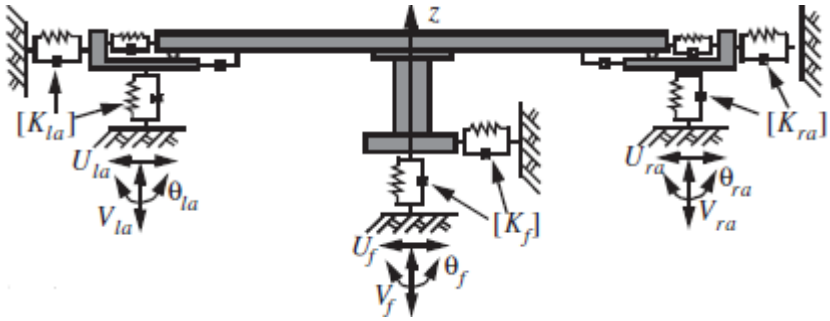

Figure 2.8. Schematic of substructuring the foundations of a bridge for seismic SSI analysis (after Zhang and Makris 2002)

Mylonakis et al. (2006) presented an analytical substructuring procedure for seismic SSI analysis of Hanshin expressway bridge during the 1995 Kobe earthquake, Japan, in order to identify the potential detrimental role of SSI on the bridge collapse. Combination of recorded and analytical evidences revealed that depending on frequency content of the ground motion, period lengthening and increased flexibility of the system due to foundation compliance may have increased significantly the seismic demand on bridge pier.

In order to incorporate inelastic soil-pile interaction in SSI analysis, a few practical studies such as those by Zafir (2002) and Lam et al. (2007) adopted equivalent linearization of the empirical p-y curves for substructure analysis of bridges. In this approach, the secant stiffness of the p-y curves along the pile length at an expected maximum ground

displacement during the earthquake is used to estimate overall foundation stiffness. Recently, Rahmani et al. (2016) showed that such a substructuring approach would provide unreliable results for seismic response of a bridge by comparing them with those from rigorous continuum analysis.

Chapter 3 : Components of finite element simulation in OpenSees

3.1. Introduction

This chapter describes the methodology and elements used for rigorous continuum modelling of soil-pile-structure interaction in the RC shaft supported bridges. With the advent of high performance computation tools, continuum modelling approach, in particular finite element method, has been increasingly utilized in both research and practice to improve analysis accuracy of complex geotechnical and structural systems. Moreover, implementation of advanced constitutive models and numerical technics to the finite element method has made it more powerful and computationally efficient approach. Generally, three different categories of components are involved in finite element simulation of a soil-structure interaction problem including: constitutive models, domain discretization tools and numerical technics. In present work, advanced constitutive models

are used to capture hysteretic behaviour of soft soil, foundation and structural components. Various elements are also implemented for spatial discretization of problem's domain, and numerical methods are adopted to perform time-domain analysis of seismic soil-pile-structure interaction.

Numerical simulations in this work are performed in the finite element program, Open system for earthquake engineering simulation (*OpenSees*) developed by McKenna and Fenves (2000). *OpenSees* is an object-oriented platform consisting of a wide variety of libraries of material's constitutive models, elements and methods for numerical solution. Such features provide extensive flexibility for researchers to investigate static and dynamic behaviour of complex structural, geotechnical or hybrid systems. Details of simulation components are explained in the sections as follows.

3.2. Materials Constitutive Models

Appropriate simulation of stress-strain behaviour of materials is the key aspect of any continuum modelling scheme. This is accomplished by means of constitutive models which are defined as theoretical and mathematical relationships between stress and strain increments in a given material. Describing such a relationship for the geological materials like soils can be quite challenging because of their complex behaviour compared to other solid materials. This complexity stems from their state-dependent and highly nonlinear nature, implying that in-situ properties (e.g. stress and density) and applied loading paths may influence stress-strain behaviour of soils. Since five decades ago, numerous works have been carried out on development of constitutive models with various degrees of sophistication to model nonlinear behaviour of soils. Among the proposed models, nested

surface (Prevost 1978) and bounding surface (Dafalias and Popov 1975, Manzari and Dafalias 1997) plasticity models have been recognized as the most successful ones in modelling the cyclic soil response under complex loading conditions. Prevost (1977, 1985) was the first who expanded application of the original nested surface plasticity concept proposed by Mroz (1967) to soil mechanics. Capability of the proposed model in simulating static and cyclic stress-strain behaviour of the cohesive and cohesionless soils has been successfully validated with the results from experimental works (Prevost 1977, Prevost 1985, Yang et al 2003, Elgamal et al. 2003). This class of soil models, known as multi-yield surface models in OpenSees, was implemented in FE program codes by Parra (1996), Yang (2003). In the following sections, a brief description is given on details of the constitutive models used for modelling stress-strain response of the clayey soil and structural materials used in this study.

3.2.1. Soil model for clayey soil

Hysteretic nonlinear stress-strain response of the soft clay in this study is simulated using the pressure-independent version of the nested surface soil models. This model, which is known as pressure-independent multi-yield surface (PIMY) material in *OpenSees* program framework, is a total stress elasto-plastic model with a purely deviatoric kinematic hardening rule, an associate flow rule and Von-Mises type yield surface. The volumetric stress-strain behaviour is linear elastic and plasticity is induced only under shear loads. Fig. 3.1a, b shows the schematics of the cylindrical yield surfaces in the principle stress space and determination of the yield surfaces in the octahedral shear plane by the hyperbolic shear stress-strain backbone curve. The cylindrical shape is because of the Von-Mises type

assumption for the yield surfaces, which assumes shear strength independent of variation of mean confining pressure. This is a fairly reasonable assumption for undrained response of cohesive soils subjected to the rapid earthquake shaking.

This J2 plasticity multi-yield surface model employs concept of a field of plastic moduli for better simulation of plastic soil deformation under cyclic loading. This field is defined as the area enclosed by collection of constant-size yield surfaces in the stress space (Gu et al. 2011). Each of these yield surfaces defines region of constant plastic shear moduli with the yield criteria function in the deviatoric stress space as follows (Prevost 1977):

$$f_m = \sqrt{\frac{3}{2}\left(S_{ij} - \alpha_{ij}^{(m)}\right):\left(S_{ij} - \alpha_{ij}^{(m)}\right)} - K^{(m)} = 0 \tag{3.1}$$

where S_{ij} is the deviatoric stress tensor, $\alpha_{ij}^{(m)}$ and $K^{(m)}$ represent the center and size of the yield surface f_m in the stress space, respectively. At a given mean confining pressure, the field size and plastic shear moduli of the yield surfaces are given by a hyperbolic backbone curve (Kondner 1963) used to describe nonlinear stress-strain behaviour of soil in the plane of octahedral shear stress as expressed below:

$$\tau_{oct} = \frac{G_{max}\gamma_{oct}}{1 + \gamma_{oct}/\gamma_r} \tag{3.2}$$

where τ_{oct} and γ_{oct} are the octahedral shear stress and strain, respectively. $G_{\max}$ and γ_r are the two parameters required for characterization of the hyperbolic stress-strain expression. $G_{\max}$ is the small-strain shear modulus, and γ_r is the reference shear strain defined as:

$$\gamma_r = \frac{\gamma_{\max,oct}\tau_{\max,oct}}{G_{\max}\gamma_{\max,oct} - \tau_{\max,oct}} \tag{3.3}$$

In the above equation, τ_{max} corresponds to the octahedral shear strength at the maximum yield octahedral shear strain. The parameters of hyperbolic curve can be determined for a given type of soil by using results of cyclic and monotonic laboratory shear tests as will be discussed in detail in Chapter 4.

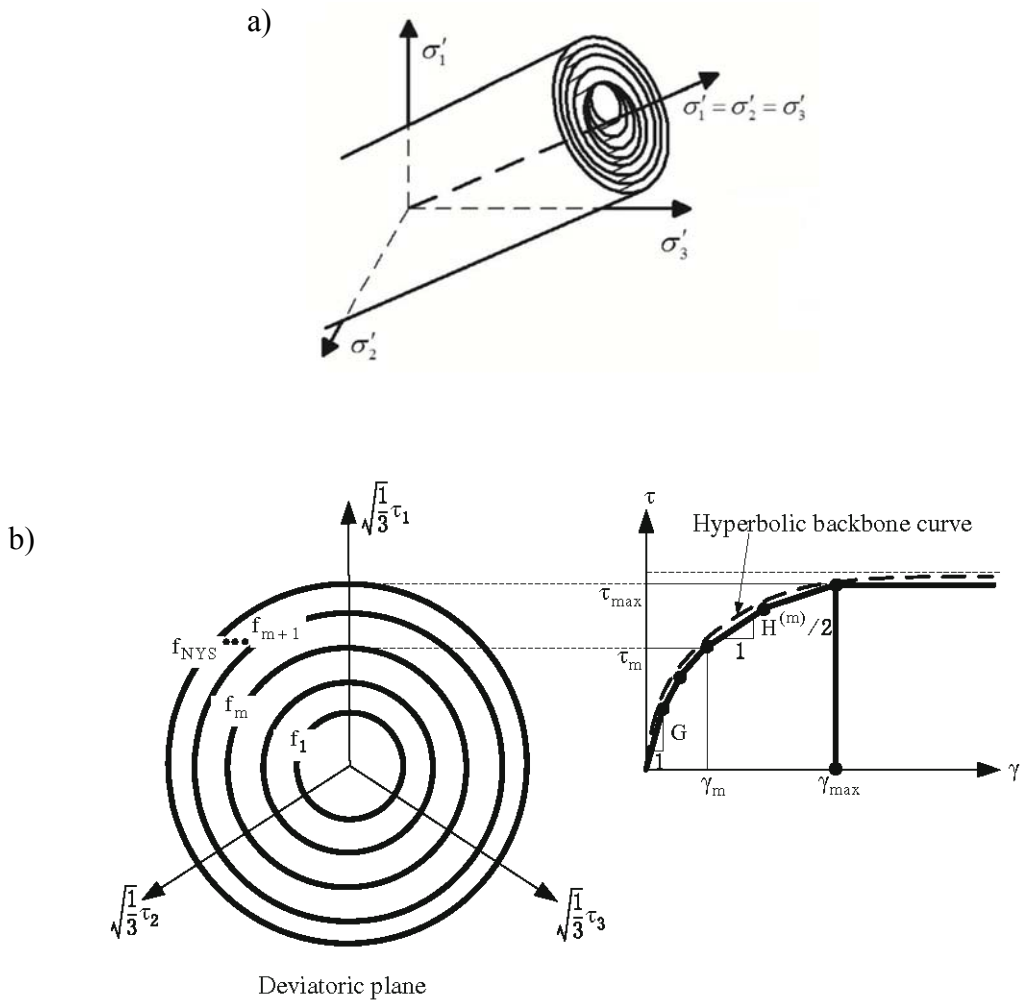

Figure 3.1. a) Cylindrical yield surfaces in the principal stress space b) domain of yield surfaces based on the hyperbolic backbone curve (after Gu et. al 2011)

3.2.2. Structural Materials

Reinforced concrete members are the main structural elements used in this study. The Kent-Scott-Park (Mander et al. 1988) model is used to model stress-strain behaviour of the unconfined (concrete cover) and confined concrete sections in the RC members. This model is a uniaxial model known as Concrete01 material in *OpenSees*, in which tensile strength is zero and unloading/reloading stiffness is degraded with increasing strain. Fig. 3.2 shows the strength envelope for hysteretic stress-strain response of the concrete, which is obtained from monotonic loading experiment. The strength envelope is described by the concrete compressive strength at 28 days (f'_{max}), strain at maximum compressive strength (ε_0), concrete crushing strength (f'_{ult}), and strain at crushing strength (ε_{ult}). The initial slope (E) of strength envelope is given by $2f'_{max}/\varepsilon_{max}$.

A simple bilinear model is used in this study for modelling the hysteretic behaviour of the reinforcement steel material. The model known as Steel01 in *OpenSees* framework is a uniaxial model with kinematic hardening rule. The stress-strain envelope of the nonlinear model is schematically shown in Fig. 3.3. Parameters used to describe this bilinear envelope are yield strength (f_y), Young modulus (E), and strain-hardening ratio (b) which is defined as the ratio between post-yield modulus and Young modulus (elastic region).

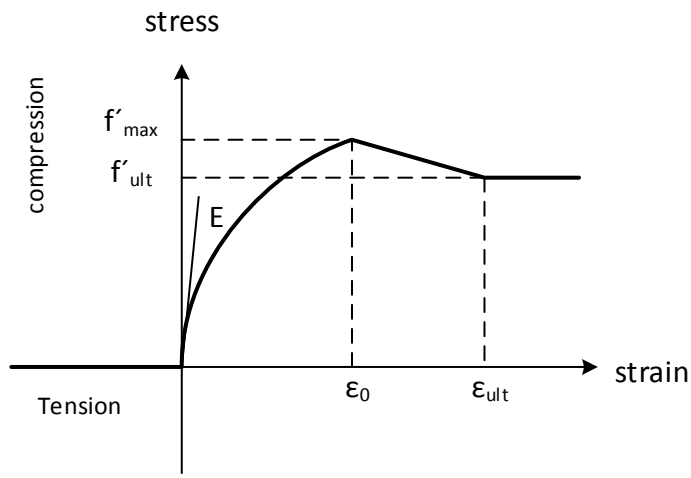

Figure 3.2. Stress-strain response of the Kent-Scott-Park concrete model

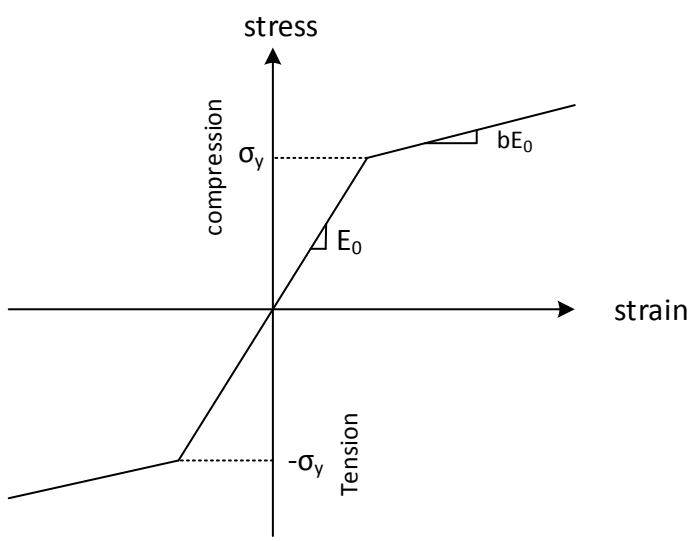

Figure 3.3. Stress-strain response of the uniaxial biaxial steel model

3.3. Simulation of Soil-Pile Interaction

Modelling soil-pile interaction, in particular soil-pile interface, as a key element of soil-structure interaction is of high importance. The pile-soil interaction governs load-transfer mechanism between vibrating objects with different dynamic properties. In the finite element scheme of this study, soil domain is discretized using the eight-node hexahedral elements known as Brick element, where each node has three degrees of freedom. The pile foundation is modelled using the displacement-based beam-column elements connected by nodes with six degrees of freedom. For simulation of soil-pile interaction, connections must be made between the two bodies to couple their response. The interaction domain is created by removing solid soil elements in the region physically occupied by the pile and placing the pile beam column elements in the center of region. A commonly used method for coupling soil-pile response is connecting the soil nodes to the pile ones at each elevation by rigid elastic beam-column elements. The connection state between the soil node and rigid elements at the soil-pile interface is only translational, while pile nodes' rotational degrees of freedom remain unconnected. Using this method for soil-pile interaction, full compatibility is enforced for all modes of deformation between soil and pile at the place of corresponding interface. Such a compatibility renders different modes of force (shear, axial and moment) to be fully transferred between the pile and the surrounding soil medium. The only advantage of this method is fairly perfect numerical stability especially under strong dynamic loadings associated with large deformations, while its major drawback is the unrealistic assumption of perfect bonding between the soil and pile, which does not account for relative displacements such as gapping or slippage that are very likely to occur between soil and pile under strong dynamic structural loads.

For more realistic simulation of soil-pile interface behaviour, interface elements (Petek 2006) known as node-to-beam contact elements in the *OpenSees* framework are used at the soil-pile interface to allow for gapping and slippage. This element is an elasto-perfectly plastic element following the Coulomb's friction law in simulating frictional behaviour at the soil-pile interface. Schematic of force-deformation relation for this contact element is shown in Fig. 3.4. Using the contact element, gap is created when the interaction force reaches zero or exceeds the tension strength at the soil-pile interface. Incorporation of the interface element into the soil-pile interaction model in clay is deemed to be essential as creation of gap has been reported to very likely occur in cohesive soils (Matlock and Foo 1978) where soi.

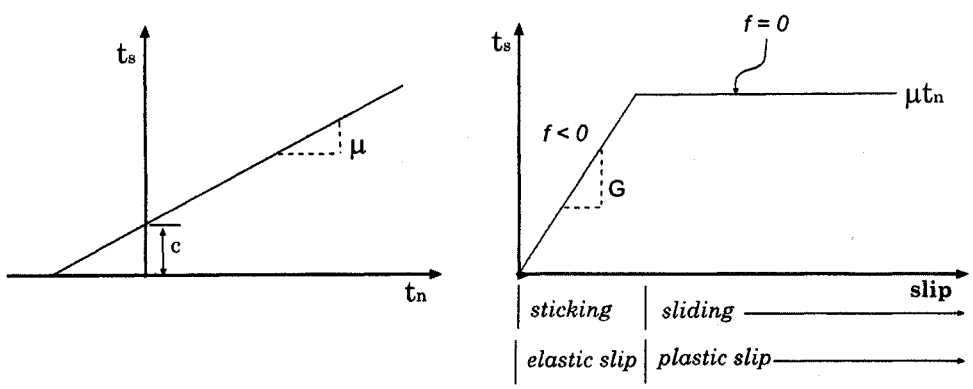

Figure 3.4. Force-deformation relation of the contact element at soil-pile interface (after Petek 2006)

3.4. Analysis Procedure of Continuum Model

Dynamic analysis of soil-pile-structure interaction is performed through three different stages. The first two steps involve static analysis of the finite element model. In the first step, the soil domain including the soil elements without presence of structural components is subjected to the soil weight to provide initial at-rest stress state. In the second step, the soil elements at the region to be occupied by the pile volume are removed, then the pile and other structural elements are incorporated to the model, and a static nonlinear analysis is performed under gravitational body forces of structural components. In the third stage, dynamic soil-structure interaction analysis is carried out by applying force-equivalent time history of the input earthquake motion at the base of the soil domain using Plain excitation pattern via single-point constraint (SP) command in *OpenSees*. Force time history is used as input excitation in accordance to the energy-absorbing boundary method discussed in detail in the following chapters.

Dynamic equilibrium equation of motion for the soil-structure system is numerically integrated using a composite time-stepping integration scheme which combines simple trapezoidal rule and three-point backward Euler method. This scheme known as TRBDF2 method (Bathe 2007) is an energy-conserving method, suitable for highly inelastic and contact problems. The system solver Multifrontal Massively Parallel Sparse direct solver (MUMPS) is used to solve the sparse system of equations developed for entire soil-structure system. Using this solver, execution time of the analysis is significantly sped up. Krylov-Newton solution algorithm is adopted to solve the nonlinear residual equation iteratively. The convergence test for solution algorithm is based on increments of energy. In fact, this is a robust criterion in comparison with displacement increments in inelastic

and contact problems associated with large deformation. The penalty method is adopted to enforce nodal constraints to the system of equations.

Chapter 4 : Calibration of Ottawa's soft clay model for seismic analysis

4.1. Introduction

In seismically active regions of eastern Canada, the dominant geological setting mainly consists of soft post-glacial sediment known as "Leda clay" or "Champlain Sea clay". This soft clay deposit, with thicknesses that exceed 100m in some locations, was formed in a marine environment resulting in a sensitive and naturally-cemented fabric in the clay. Laboratory investigations on geotechnical properties of Leda clay, particularly stress-strain response, have illuminated the contribution of this natural cementation on the distinct behaviour of this structured clay compared to other non-cemented clays. Moreover, the presence of rigid crystalline bedrock underlying this soft clay deposit elevates the seismic hazard risk by providing a significant impedance contrast. This contrast has been confirmed by geophysical studies that show the capability of such geological conditions to

significantly amplify weak seismic motions (Khaheshi Banab et al. 2012). As the Ottawa area is located within the West Quebec Seismic Zone, it is frequently subjected to earthquakes with magnitude ranges of M 2.0-4.0. This area has also experienced higher magnitude earthquakes such as the 2010 Val-des-Bois earthquake at M 5.1.

In this study, the Ottawa's soft clay is adopted as the target model soil in order to have realistic soil-pile-structure interaction analysis. Model soil layering in the analysis also follows typical stratification of clay layers existing in the Ottawa area. This chapter discusses the calibration process of Leda clay model for use in seismic analysis. The calibration procedure involves three main stages outlined as follows:

- Geotechnical parameters required for dynamic analysis are obtained from various experimental works, and interpreted collectively to describe stress-strain behaviour of Leda clay.
- Two most crucial soil parameters for seismic analysis, *shear strength* (S_u) *and small-strain shear modulus* (G_{max}) are characterized in detail. A relation between G_{max} and soil stress state is proposed based on available experimental data. The strain rate dependency of the shear strength is also described and corresponding adjustment of monotonic shear strength for seismic application is proposed.
- Finally, the calibration of Leda clay's small-strain shear modulus is verified by a site response analysis using weak ground motions recorded during the 2010 Val-des-Bois earthquake striking Ottawa area.

4.2. Properties of Leda Clay from Laboratory Tests

Leda clay is a type of marine soft clay formed during the most recent ice age (circa 10,000 years ago) in the Ottawa River lowlands, and it covers most of the Ottawa valley and southern Quebec in eastern Canada. This soil is the result of glacial abrasion of the Canadian Shield resulting in a fine rock flour which was deposited at the bottom of the prehistoric saltwater Champlain Sea that flooded the region. The average bulk density of the soil was estimated to be 1.53 Mg/m^3 with natural moisture content of about 67% (ASTM D2216). The particle size distribution of this soil, obtained from a hydrometer test (ASTM D422), shows a clay fraction of about 40%. The liquid limit and plasticity index of the soil were measured at about 51% and 23, respectively, as per ASTM D4318. The soil is classified as CH in the USCS classification system (ASTM D2487).

Depending on the intensity of the incident earthquake, soil deposits may undergo various levels of shear strain ranging from 10^{-5} to 5%; implying that an adequate dynamic characterization needs to be carried out on the soil of interest. In most of the current methods used, maximum/small-strain shear modulus (G_{max}), the strain-dependent variation of shear modulus (G/G_{max}) and damping (D%) are the crucial parameters that directly control the soil response. However, because of the complex behaviour of sensitive clays, detailed monotonic and cyclic properties of the soil should be taken into account for accurate calibration of constitutive soil models. Several laboratory tests have revealed that inter-particle cementation bonds govern the strength and deformation characteristics of Leda clay within in-situ overburden stress range. Results of one-dimensional consolidation tests performed on Leda clay samples in different studies have admittedly indicated very stiff behaviour in the pre-yield stress region with brittle response around the pre-

consolidation pressure (Mitchel 1970; Vaid et al. 1979; Quigley et al. 1983). Moreover, the strain-rate dependent feature of the stress-compressibility relationship of the sensitive clay from eastern Canada, with noticeable contribution of secondary consolidation, was investigated by Leroueil et al. (1983) and Vaid et al. (1979). Generally, it is believed that a combination of natural cementation and secondary consolidation can result in stable structure-induced overconsolidated clay without change of in-situ effective vertical consolidation stress.

Recently, monotonic and dynamic characterization of Leda clay has been carried out by Rasmussen (2012) using a series of laboratory tests. She conducted monotonic direct simple shear (DSS) tests on clay samples that are consolidated at in-situ effective consolidation pressures (σ'_{vc}) and k_0 conditions, where k_0 is the at-rest lateral earth pressure coefficient. The obtained undrained peak shear strength (S_u) from these tests is a crucial factor for site response analysis when large shear strain is mobilized in the soil column. The shear stress-strain curves from the monotonic tests indicated that the peak shear strength occurs at failure shear strain (γ_f) of 2-3%. The shear strength of the clay at any given depth is determined by using the empirical equation for normalized strength (Ladd 1991) as given by:

$$S_u/\sigma'_{vc} = \alpha(OCR)^{\beta} \tag{4.1}$$

In Eq. 4.1, $OCR = \sigma'_p/\sigma'_{vc}$ is defined as the overconsolidation ratio and σ'_p is the yield pressure in the compression curve, interpreted from the consolidation test for a structured clay. The above equation is calibrated for Leda clay by fitting a power law function to the reported data from monotonic tests as shown in Fig.4.1. The regression coefficients α and n were determined to be 0.23 and 0.9 with the goodness-of-fit measure of $R^2 = 0.97$,

respectively. The estimated value for the overconsolidation exponent is also consistent with the value given by the following equation proposed by Ladd (1991):

$$n = 0.88(1 - C_r / C_c) \pm 0.06 \tag{4.2}$$

By substituting the average compression (C_c) and recompression (C_r) indices derived from consolidation tests in Eq. 4.2, *n=0.86* was computed, which is close to the value from the regression.

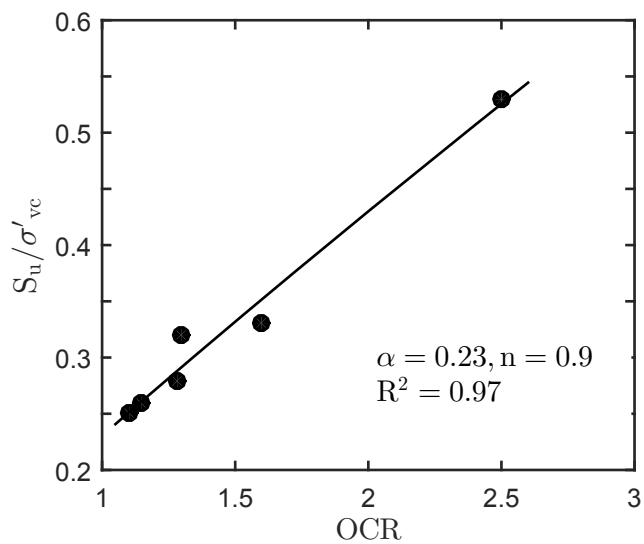

Figure 4.1. Calibration of monotonic shear strength equation for Leda clay based on the experimental data

Rasmussen (2012) also performed a number of cyclic DSS (DCSS) tests to characterize cyclic resistance and to develop soil stiffness degradation (G/G_{max}) and hysteretic damping (D) curves for Leda clay in the large shear strain range ($\gamma_c > 0.1\%$), while low-strain shear stiffness degradation ($\gamma_c < 0.05\%$) was investigated by the resonant column (RC) tests. All the RC and DCSS tests were conducted on samples from a depth of about 15m and consolidated under in-situ pressure of σ'_{vc}=106 kPa. Fig. 4.2 depicts the G/G_{max} and damping curves (D) with the level of cyclic shear strain from the described

cyclic tests. The large-strain part of modulus reduction is adopted herein for seismic analysis.

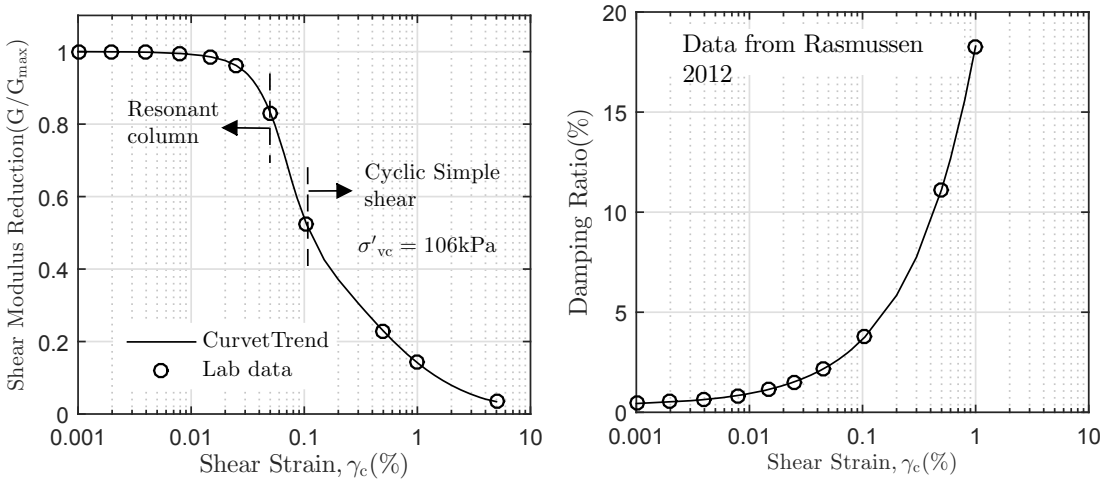

Figure 4.2. Experimental shear modulus degradation and damping ratio for Leda clay

Following the outcomes of in-situ geophysical testing by Crow et al. (2011) in intervals of massive Leda clay, the very low-strain damping ratio (D_{min}) was adjusted to 0.4 %. Moreover, they concluded that Leda clay exhibits fairly frequency-independent small-strain stiffness and damping. This type of non-destructive experiment is believed to provide the most reliable low-strain dynamic properties for the sensitive clays, since the structured fabric of the clay is retained. The small-strain shear modulus (G_{max}) is the principal factor governing pre-failure shear behaviour of structured clay. It is well established that stress-strain parameters of fine grained soils are strain-rate dependent over a wide range of shear strain. However, the clay fabric can influence the degree of dependency; such that the loading frequency has minimal effect on the G_{max} of the naturally-cemented clays with less viscous characteristics, compared to the de-structured clays with direct contacts between clay particles (Soga, 1994). This is consistent with the

findings of Crow et al. (2011) from field geophysical experiments regarding the frequency-independent trend of the low-amplitude shear wave velocity in Leda clay. The only measurement of G_{max} for Leda clay from an RC test was reported to be around 28Mpa by Rasmussen (2012). This value was measured under $\acute{\sigma_{vc}} = 106\ kPa$, and at the resonant frequency of 28 Hz. Despite the lower degree of frequency dependent behaviour of G_{max} in sensitive clays, the large difference between the measurement frequency and the average predominant frequency of the earthquake motions (~1 Hz) requires adjustment of the G_{max} value from RC test. Reviewing the dynamic small-strain behaviour of the sensitive clays, the measured G_{max} value in the RC test should be corrected for two effects in this study in order to obtain a true G_{max} value for the earthquake analysis. First, the frequency effect was considered by applying a strain-rate factor of 5% per log cycle as proposed by D'Onofrio (1999) for a structured clay from Italy. Secondly, to account for the sampling disturbance effect which can be significant in sensitive soils, a correction factor of 1.2 was applied to the laboratory G_{max} as per the chart from ROSRINE study (Stokoe et al. 1998).

4.3. Calibration of Soil Models for Seismic Analysis

The maximum shear modulus (G_{max}) and undrained shear strength are the key parameters in seismic analysis, governing small-strain and large strain response of the soil during earthquake loading. Thus, this section principally focuses on calibrating the relations between the G_{max} and the soil's stress state parameters such as effective consolidation stress as well as overconsolidation ratio in order to provide shear wave velocity profile for seismic analysis. Viggiani and Atkinson (1995) proposed a formula for G_{max}as a function of in-situ mean effective stress and yield stress ratio, expressed as below:

$$\frac{G_{\max}}{P'_a} = A\left(\frac{P'_m}{P'_a}\right)^n (OCR)^m \tag{4.3}$$

where $n \approx 1$ for clays as proposed by Yamada et al. (2008), and m=constant that depends on the clay properties, e.g., plasticity index and structure of the clay; A=a factor that depends on the structure of the clay; P'_m =mean effective stress. Eq. 4.3 can be expressed in terms of detailed soil parameters as below:

$$\frac{G_{\max}}{P'_a} = A\left(\frac{1+2K_0}{3}\right)^n \left(\frac{\sigma'_{vc}}{P'_a}\right)^n \left(\frac{\sigma'_{\max}}{\sigma'_{vc}}\right)^m \tag{4.4}$$

where, σ'_{max} = effective yield stress with the assumption of taking OCR as the yield stress ratio; σ'_{vc} = vertical effective consolidation stress, and K_0 = at-rest soil lateral pressure coefficient. The G_{max} of a Leda clay sample from a depth of about 15m was measured at $\sigma'_{vc} = 106\ kPa$ in resonant-column device. The $K_0 = 0.91$ was estimated for this overconsolidated clay ($OCR = 1.5$) by utilizing $K_0 = (1 - \sin\phi')OCR^n$ (Jaky 1944; Schmidt 1966), where $n = 0.95$ as proposed by Lefebvre (1991) from the field hydraulic fracture tests. The overconsolidation exponent ($m = 0.4$) was adopted, which is slightly higher than the value proposed by Hardin and Drnevich (1972b) for the clay with $PI = 40$. This is related to the fact that the structure-induced overconsolidation is more influential on the pre-failure behavior of the natural clays, compared to its load-induced counterpart in the destructured clays. Applying the described values of the parameters to the Eq. 4.4 along with the corrected G_{max} of 32 Mpa, $A = 288$ was computed. Since stiffness degradation of clays is typically insensitive to the variation of effective confining pressure (Kokusho et al.1982; Yamada et al. 2008), the large-strain part of the modulus-reduction (G/G_{max}) curve shown in Fig. 4.2 is applied to all clay layers throughout the model.

Nonlinear soil constitutive model (Chapter 3) requires the shear strength envelope (backbone curve) to simulate hysteretic cyclic response of the soil. The shear strength envelope of the cohesive soils has been observed to be strain-rate dependent due to the viscous nature of inter-particle contacts, asymptotic to the dynamic shear strength $(S_u)_d$ (Sheahan et al. 1996; Lefebvre and Pfendler 1996). Therefore, undrained shear strength (S_u) from monotonic tests must be increased for the strain-rate effect, as determined to be about 12% per log cycle for Champlain Sea clay. This issue matters in modelling dynamic response of clays in seismically active regions where a large deformation of soil is likely to occur. If the soil-specific modulus-reduction curve is available from cyclic laboratory tests (e.g. simple shear) conducted at high strain rates (e.g. 1 Hz), it does implicitly contain strain-rate effect and can be directly used to construct the dynamic shear strength envelope $(\tau_c = G\gamma_c)$, as depicted in Fig.4.3. The large-strain part of the G/G_{max} curve proposed by Rasmussen (2012) was derived from the strain-controlled cyclic simple shear test performed at 1 Hz frequency. Thus, the implied shear strength at $\gamma_c = 3\%$ from this modulus-reduction curve is equivalent to the shear strength recorded at a shear strain rate of $\dot{\gamma}_c = 43200\ \%/hr$. This rate is 8340 times greater than the strain-rate of $5\ \%/hr$ used in monotonic tests. Therefore, by considering a 12% increase of monotonic shear strength per log cycle of increase in strain-rate, the dynamic shear strength $(S_u)_d$ was anticipated to be approximately 53% greater than the shear strength from the monotonic tests for Leda clay. Fig. 4.3 also shows the hyperbolic representation of the G/G_{max} curve for use in practical site response analysis tools such as *DeepSoil* program, given as follows:

$$\frac{G}{G_{\max}} = \frac{1}{1+\beta\left(\frac{\gamma}{\gamma_r}\right)^{\alpha}} \tag{4.5}$$

where G =secant shear modulus (= τ/γ); G_{max}=small-strain shear modulus; γ =shear strain; γ_r= reference strain and β and α=curve-fitting coefficients. Within the framework of hyperbolic approximation, two fitting scenarios can be considered: i) the curve-fitting parameters are optimized to provide a best-fitting curve to the G/G_{max} data ($\beta = 1.53, \alpha = 1.23$), resulting in a strain-softening backbone curve yielding an implied shear strength that is much lower than the experimental value. ii) The hyperbolic model proposed by Darendeli (2001) ($\beta = 1.0, \alpha = 0.94$), with the adjusted curvature parameter (α) so that the resultant backbone curve would asymptote to the dynamic shear strength $(S_u)_d$. In both fitting scenarios, the reference shear strain $\gamma_r = 0.14$ % corresponds to the shear strain at which $G/G_{max} = 0.5$ (Darendeli, 2001). Fig. 4.3a compares fitted hyperbolas to the Leda clay's G/G_{max} from laboratory tests. Similarly, Fig. 4.3b compares the backbone curves generated from the stiffness degradation trends shown in Fig. 4.3a. As shown, the strength-adjusted hyperbola seems to be in better agreement with the laboratory-based modulus-reduction than the optimized hyperbola, particularly in the medium-to-large shear strain range.

As described in Chapter 3, the elasto-plastic constitutive model approximates the modulus reduction and the corresponding stress-strain backbone curves by a hyperbolic function in the octahedral stress plane. Three soil parameters from experimental data, including maximum shear modulus (G_{max}), cohesion at zero effective confinement (C_u) and maximum shear strain (γ_{max}) must be input to the model for definition of the hyperbolic backbone curve. The cohesion (C_u) is estimated from the equation of shear failure criteria

in the octahedral stress space. In this equation, the peak shear strength value is given by the corresponding modulus reduction ratio (G/G_{max}) at the maximum shear strain (γ_{max}). $\gamma_{max,oct}$ is also obtained by applying a coefficient of $\sqrt{2/3}$ to the γ_{max} value. Fig.4.3. illustrates generation of the shear stress-strain backbone curve from the different scenarios of approximating experimental G/G_{max} trend. It is shown that how the misrepresentation of the large-strain part would lead to significant underestimation of the undrained shear strength for seismic analysis. It should also be noted that the elasto-plastic constitutive model has two limitations for accurate simulation of the stress-strain behaviour of sensitive clays at large strains. First is model's inability to capture strain-softening behaviour of soil at large strains, which is often observed as the post-peak response in sensitive clays, and second is utilizing Masing's unloading-reloading rule for cyclic simulation, which may result in damping values higher than those from laboratory tests. Hence, this model is calibrated by several basic soil parameters to just simulate the stress-strain response of Leda clay up to the peak shear strain value.

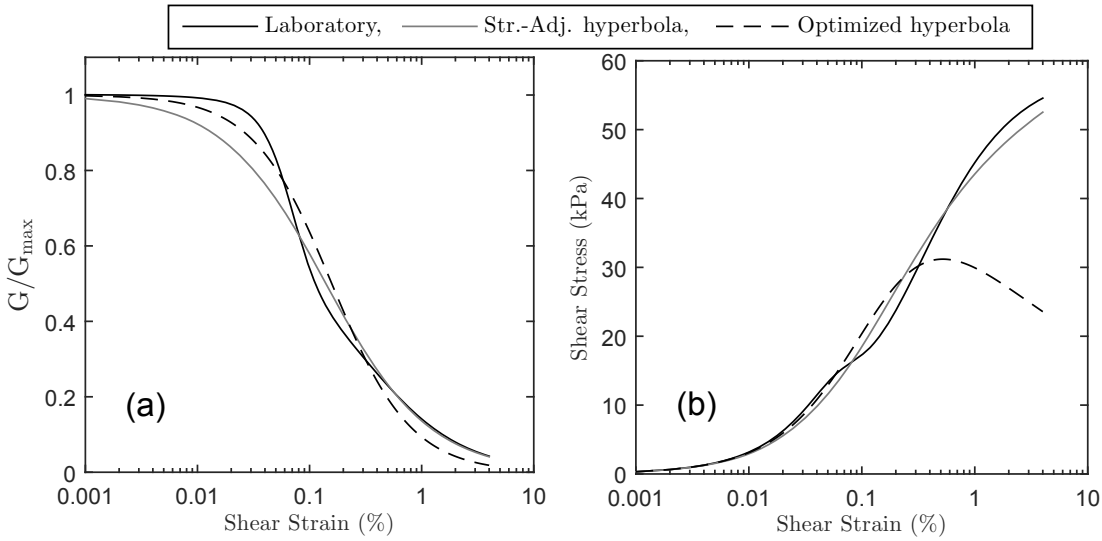

Figure 4.3. Generation of the shear strength envelope from the three different representations of the shear modulus degradation curve

4.4. Validation of Calibrated Models

This section intends to verify applicability of the calibrated equation for the small-strain shear modulus of Leda clay to the seismic analysis. Two nearby instrumented sites, ORHO and ORIO, from the suburban Ottawa area were selected as target sites for verification purposes. ORHO station, which is located toward the deepest part of the basin, includes a fairly thick layer of Leda clay, and ORIO station is a rock outcrop site located 1.6 Km away from the ORHO station (Khaheshi Banab et al. 2012). The ground motion time series recorded by these two stations during the most recent earthquake (M5.1 Val-des-Bois 2010) that occurred in the Ottawa area are shown in Fig.4.4. These data, which are available from the database of the Geological Survey Canada, were utilized for validation of the calibrated models. The geological stratification of the soil site (ORHO) comprises a top 2m layer of medium-dense silty sand underlain by 81m of post-glacial sediment (Leda clay) and 10m of glacial till.

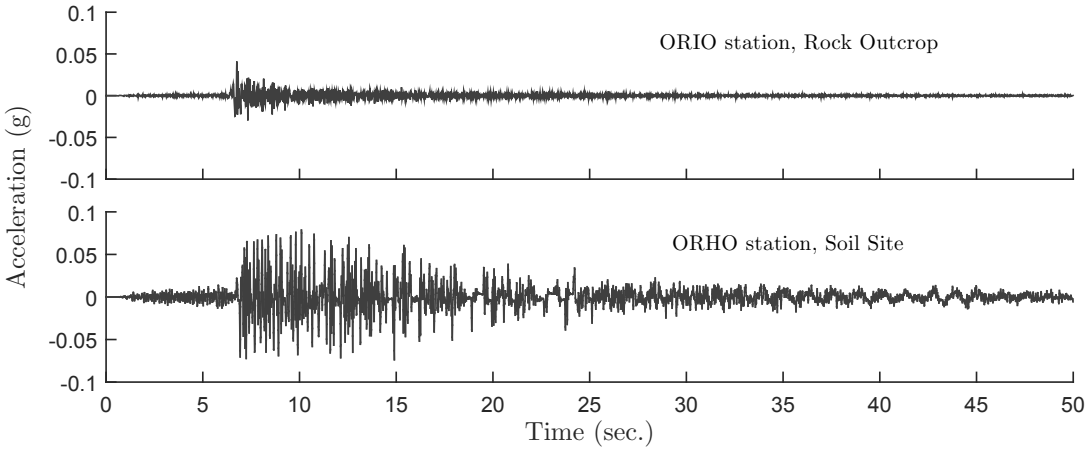

Figure 4.4. Time histories of the recorded ground motions during the 2010 Val-des-Bois earthquake

The profile of small-strain shear modulus (G_{max}) variation with depth is a principal parameter to be input to the site response models. Therefore, the calibrated Eq.4.4 was employed to identify this profile in the 81m Leda clay layer at the ORHO site, which in turn requires determination of the stress state profile (OCR, σ'_{vc}) of the clay with depth. Field measurements of the overconsolidation ratio at various depths ($\sim up\ to\ 60m$) from 31 sites in Quebec revealed that eastern-Canada sensitive clays are mainly preconsolidated (Demers and Leroueil 2002). Similar conclusions were also reported by Crawford (1961) and Quigley et al. (1983) for the shallower depths ($\sim up\ to\ 35m$) of Leda clay from the Ottawa valley. In this study, an approximate trend of overconsolidation profile for the ORHO site was developed on the basis of the reported trends from the field observations and laboratory consolidation tests by Rasmussen (2012). As shown in Fig.4.5a, the OCR profile consists of two parts; first, the top 20m segment including OCR data points extracted from the laboratory consolidation tests along with the estimated ordinates in order to achieve a trend similar to those from previous studies. Shown in Fig. 4.5a in the depth interval between 7 and 12m is a lightly overconsolidated layer trapped right beneath the top overconsolidated layer. The post-depositional erosion of top soils prior to the 100% consolidation of the trapped layer is believed to be the cause of such a trend (Quigley et al. 1983). The second part of the OCR profile is the segment from a depth of 20m to the bottom of the clay deposit, where secondary consolidation and the natural cementation are thought to be the dominant overconsolidation mechanisms. For this segment, the OCR values were assumed to increase linearly from 1.3 to 1.6 with depth according to the data reported by Demers and Leroueil (2002) for deeper layers.

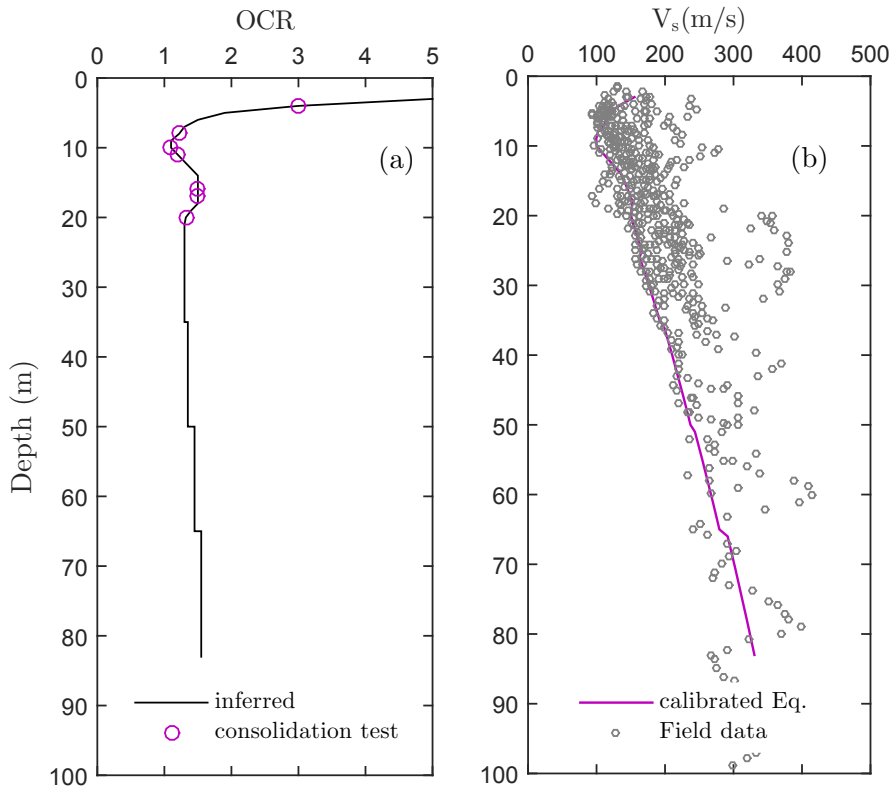

Figure 4.5. a) Variation of overconsolidation ratio of Leda clay with depth b) comparison between the shear wave velocity profile from the field experiments and the calibrated equation of this study

Table 4.1. Estimated properties of Leda clay at five representative depths

Depth (m)	γ_{avg} (kN/m^3)	σ'_{vc} (kPa)	OCR	G_{max} (kPa)	S_u (kPa)	$(S_u)_{d,emp}$ (kPa)	$(S_u)_{d,DCSS}$ (kPa)
4	15.5	37	3	24775	23	35	41
10	16	69	1.1	16323	17	26	27
20	16	131	1.3	36930	39	59	61
40	17	266	1.35	76741	80	123	126
70	17.5	301	1.55	161720	167	255	265

*G_{max}, small-strain shear modulus given by $G_{max}=288(\dot{P}_m)(OCR)^{0.4}$; S_u, undrianed shear strength at shear strain γ_c=3% given by $S_u=0.23(\sigma'_{vc})(OCR)^{0.9}$; $(S_u)_{d,emp}$, dynamic undrained shear strength given by the empirical strain rate-adjusting factor $(S_u)_{d,emp}=1.53S_u$; $(S_u)_{d,DCSS}$, dynamic undrained shear strength given by the modulus curve from DCSS test $(S_u)_{d,DCSS}=G_f.\gamma_f$

Table 4.1 presents the estimated soil properties for five representative depths within the Leda clay layer in the ORHO site that are input to the site response analysis. A close match is observed between the $(S_u)_{d,emp}$ and $(S_u)_{d,DCSS}$ values, particularly at deeper levels, indicating that applying the unique modulus reduction curve, or at least its large-strain portion, for the entire depth of the clay layer is reasonable. In this step, to ensure validity of the estimated G_{max} profile as well as its underlying assumptions, Fig. 4.5b compares schematically the shear wave velocity profile computed from the G_{max} values with a range of velocities determined by the seismological experiments from the 18 Ottawa-Montreal boreholes (Hunter et al. 2007). As shown, the estimated profile in this study is fairly in agreement with the trend from the field experiment measurements.

In the final step of verification, the input soil parameters for all layers as shown in Table 4.1 were implemented in the site response model built in *OpenSees* framework. Configuration of the pseudo-3D finite element model developed in *OpenSees* is shown in Fig. 4.6. The spatial discretization of the continuum soil column was carried out using the 3D eight-node Brick elements, allowing for multi-directional site response analysis. The procedures for constitutive modelling of clay soil as well as model development in the *OpenSees* were fully described in Chapter 3. The lateral boundary condition follows the shear-beam type condition requiring the nodes with equal elevations to be constrained to have equal displacement in three directions. The time-stepping HHT method (Hilber et al. 1977) with the parameter $\alpha = 0.7$ was used to integrate the equation of motion in the finite element model. An energy-absorbing boundary condition was used at the base to avoid the reflection of the seismic wave back into the model. This is accomplished by employing the model proposed by Joyner and Chen (1975), in which a viscous dashpot represents the

bedrock stiffness, and input motion is applied as an equivalent force developed from the velocity conversion of the earthquake record. It is worth noting that the recorded rock outcrop motion can be directly applied with the energy-absorbing boundary condition (Kwok et al. 2007). Thus, the rock outcrop motion recorded at the ORIO site (Fig. 4.4) is directly input to the model.

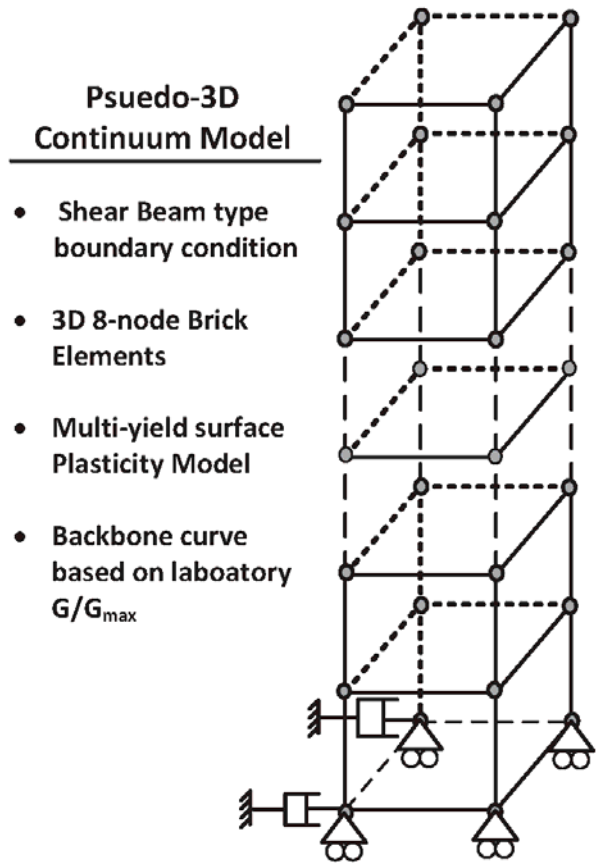

Figure 4.6. Conceptual layout of the finite element model used for nonlinear site response analysis

Figure 4.7 presents the level of agreement between the estimated 5% damped acceleration response spectra from the nonlinear *OpenSees* (NLO) analysis and the recorded motion at the ORHO site. As evident in Fig. 4.7, in general, an encouraging match exists between 1D response analysis and recorded spectra over the dominant period range. The noticeable mismatch was observed within a single period range of the fundamental site period, which was determined to be 1.25 and 1.41 seconds from the surface-to-rock Fourier spectral ratio for the recorded and estimated time series, respectively. The higher spectral values of the recorded motion in the long period range ($T > 1\ sec.$) is very likely to be caused by the basin effect in the Ottawa valley. This effect, which cannot be captured by 1D ground response analysis, results in a lengthening of the duration of the earthquake shaking and extra amplification at the fundamental site period (Kramer 1996).

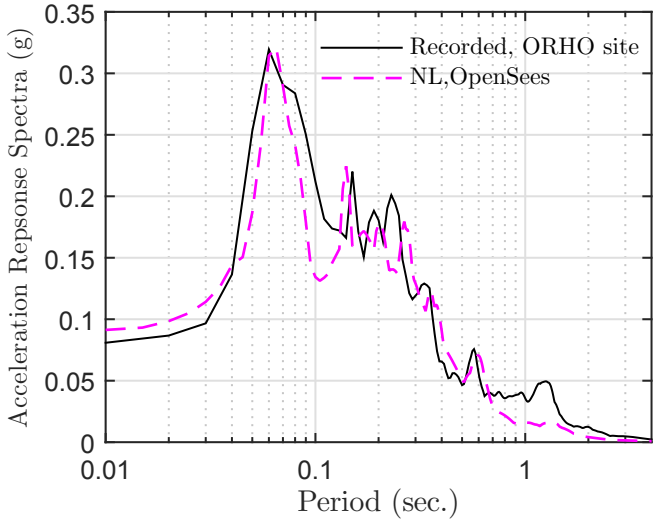

Figure 4.7. 5% damped acceleration response spectra of the recorded and estimated ground surface motion during the 2010 Val-des-Bois earthquake

Chapter 5 : Continuum modelling of inelastic soil-pile-structure interaction for bridge structure

5.1. Introduction

Previous studies have shown that seismic soil-structure interaction may have detrimental impact on structures with foundation supported in soft soils. These effects can be pronounced in massive structures such as bridges. The seismic SSI comprises dynamic interaction between the far field soil domain, near field soil-foundation system and the structure. In fact, interaction between the two latter components occurs in a coupled manner when they are subjected to seismic excitation from the far-field soil domain. The current widely used methods for SSI analysis of the pile-supported structures, including the substructure and Beam-on-Nonlinear-Winkler-Foundation (BNWF) methods mainly rely on evaluation of the impedance functions and *p-y* curves, respectively. As for the substructure method, since the early 1970s, several analytical and semi-analytical studies

have been carried out to derive the pile head impedance functions. In all these efforts, underlying assumptions are the linear elastic soil behavior and the rigid bonding at the soil-pile interface, which make the substructure method inadequate for SSI analysis of nonlinear problems. On the other hand, performance of the BNWF method in predicting SSI effects is limited by two issues which are the empirical basis for derivation of the *p-y* curves (API 2007) plus employing soil representative independent springs to support the pile.

Continuum modelling is recognized as the most powerful technique for seismic analysis of the soil-structure systems because of its capability in capturing fully coupled interaction between the SSI components including energy dissipation mechanisms, kinematic soil-pile and inertial soil-structure interactions. With advances in high performance computational tools and methods in the recent decades, 3D continuum modelling has been used for simulation of small scale or large scale soil-structure systems. However, these models have been rarely used for fundamental identification of nonlinear soil-pile-structure interaction in RC shaft supported bridges.

In this chapter, development of a 3D finite element model for analyzing the seismic SPSI in RC shaft supported bridges is described, and the respective SPSI-induced impacts on the bridge system in soft soil is discussed. The developed model was validated by comparing the finite element simulations with seismic SPSI centrifuge test results. The main objectives of developing the 3D finite element model of the SPSI can be summarized as follows:

- The first objective is to investigate the potential impacts of inelastic seismic SPSI on seismic response of RC shaft supported bridges designed according to the current design guidelines, through a rigorous fully coupled analysis. The goal is to

investigate the combined effects of the superstructure loads (inertial interaction) and the soil displacement (kinematic interaction) on performance of the structure-pile system.

- The second goal is to generate baseline data for the next part of this study in which the impedance functions are estimated for use in the computationally efficient substructure method. Results of the fully coupled SSI analysis provided by the finite element model are implemented to a back-calculation analytical solution to derive the impedance functions under coupled nonlinear condition.

5.2. Analysis of Nonlinear Soil-Pile-Structure Interaction for the Bridge Structure

5.2.1. Conceptual Bridge Model and Design

Reinforced concrete (RC) drilled shaft is commonly used as an economical bridge foundation in problematic geological settings such as liquefiable loose sand or soft clay deposits because of its substantial lateral capacity. This large diameter pile shaft namely the cast-in-drilled-hole pile is constructed as the extension of the pier column in the single or multi-column bent highway bridges. According to the Caltrans seismic bridge design guidelines (2013), structural members of the RC bridges shall be designed ductile in order to take advantage of the energy dissipation under strong earthquake loadings. RC shafts are categorized as type I and II, pertaining to the desirable level of inelastic action in the structural column-pile shaft system. In type I shafts, the inelastic action and plastic hinge formation are permitted below the ground and along the pile shaft, while type II shafts are designed to confine the plastic hinge to the above-ground pier column and avoid structural yielding of the pile shaft (Fig. 5.1).

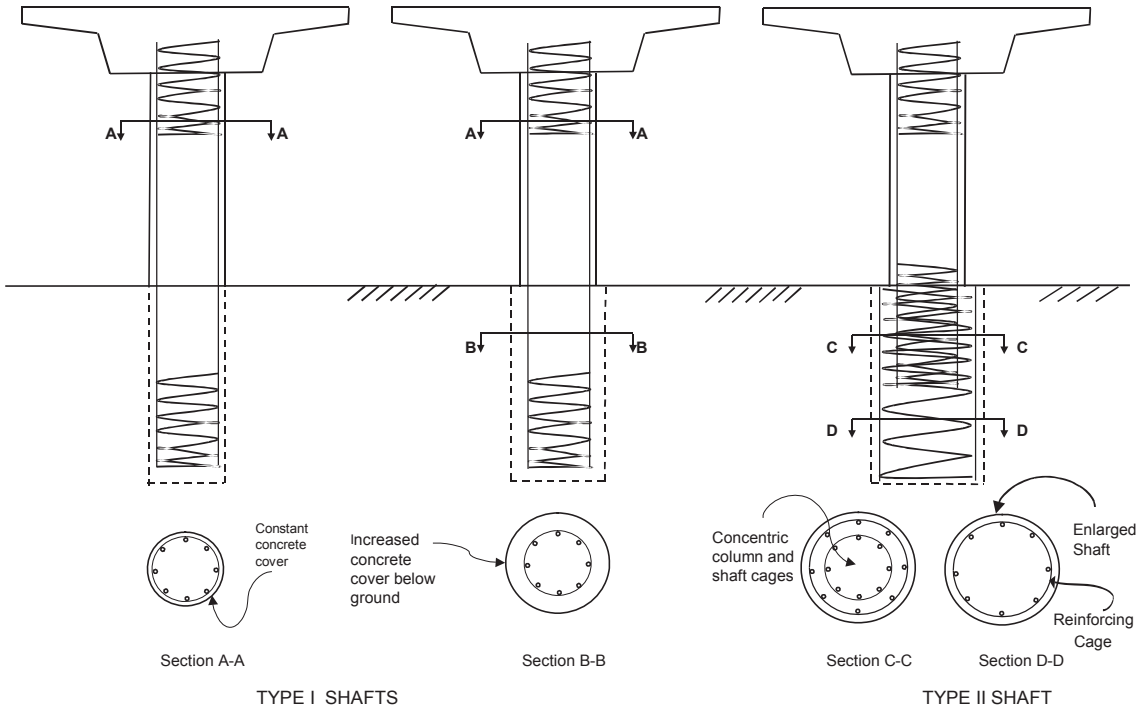

Figure 5.1. Types of reinforced concrete extended pile shafts for bridges (Caltrans 2013)

Seismic response of the bridges supported by the extended RC shafts is significantly affected by the seismic soil-pile-structure interaction phenomenon. Current state of practice design guidelines are based on complete isolation between the dynamic structural analysis and the foundation design, ignoring soil-structure interaction effect (AASHTO 2012). However, equivalent-static analysis (ESA) so-called push-over method may be used to account for contribution of the increased base flexibility (SSI effect) to the lateral behavior of the bridge (Caltrans 2013). This would require estimation of the superstructure inertial demands. In this method, the superstructure acceleration at the first-mode natural period is determined from the 5% damped design response spectra or the response spectra of the site-specific ground response analysis, then, it is multiplied by the appropriate tributary mass of the superstructure to obtain the inertial forces. This method is associated with two

disadvantages; (1) it does not consider the increased natural period of the system due to soil flexibility in the spectral analysis, and (2) the ESA method inherits the deficiencies of the BNWF approach as the common analysis method, described in the previous sections.

In this study, the conceptual bridge model for SPSI analysis is the response of a representative segment from a typical highway bridge in the transverse direction as shown in Fig. 5.2. This assumption was based on the fact that the bridge response in the transverse direction can be critical due to lower level of the lateral restraint compared to the longitudinal direction. The model bridge consists of a concrete box girder deck supported by a single large-diameter pier column. The structural loads are carried by a large-diameter type II RC pile shaft. The tributary mass of the segment is modelled as the lumped mass at top of the column shaft. The conceptual model is designed in accordance with the current AASHTO (2012) LRFD and Caltrans (2013) bridge design guidelines. The detailed seismic design procedure for the representative lumped mass system and the pile shaft is discussed in the following sections.

The site geology at the bridge model follows the soil stratification profile as exists in the Ottawa area and fully discussed in Chapter 4. Since monopile shafts are commonly used as the end-bearing pile sitting on a stiff stratum, shallow soft clay deposits are intended in this study. Two soil profiles with depths of 17m (site 1) and 30m (site 2) are considered in the analysis in order to analyze effect of the frequency content of the site's vibration on the SPSI mechanism. According to the shear wave velocity profiles shown in Fig.5.3, geology of both the sites consists of three relatively distinct soil layers including a top thin layer of over consolidated clay with average V_s of 130 m/s, underlain by a layer of soft normally consolidated layer with average V_s of 100 m/s and the bottom layer with shear

velocity linearly increasing with depth. The input soil parameters at representative depths for the constitutive model are summarized in Table 5.1.

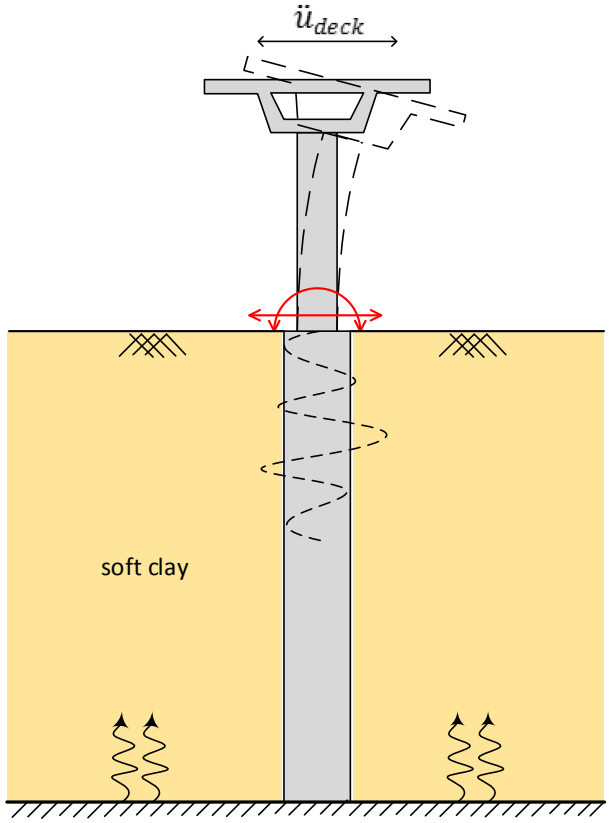

Figure 5.2. Conceptual schematic of the soil-pile-structure interaction for a single column highway bridge

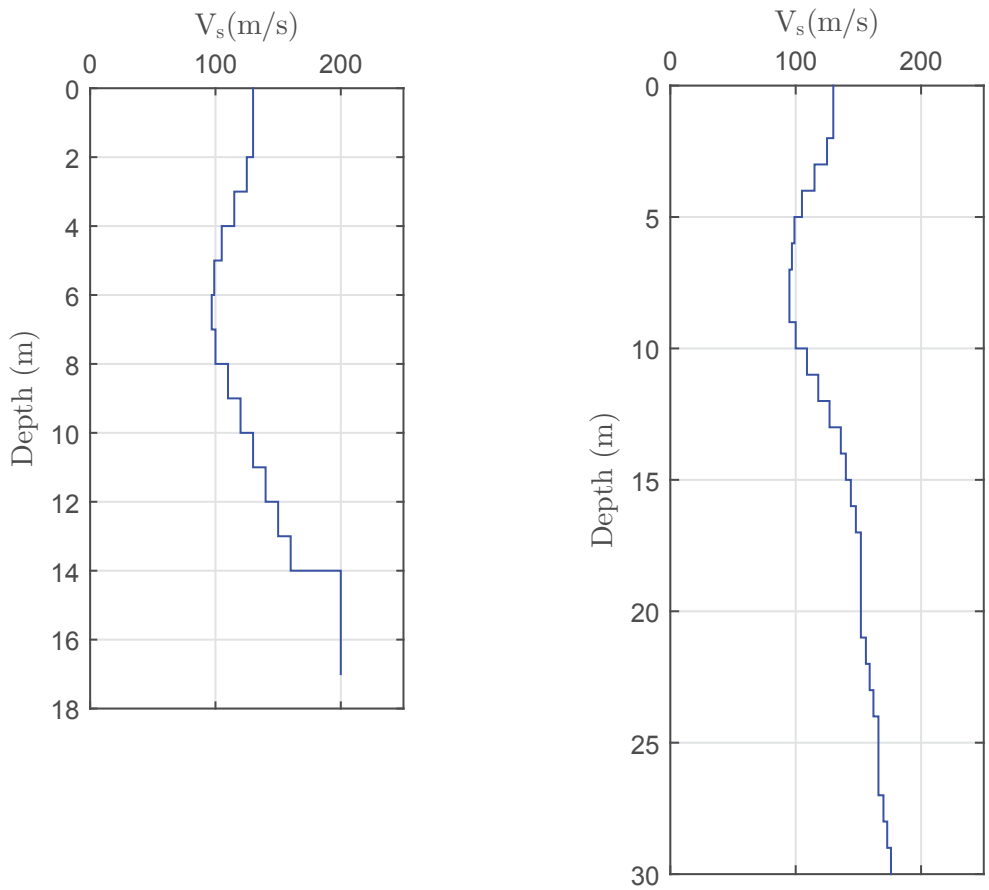

Figure 5.3. Shear wave velocity profile for the soil sites used in this study

Table 5.1. Input soil parameters for the constitutive model

Depth (m)	V_s (m/s)	S_u (kPa)	ρ (Mg/m^3)	G_{max} (Mpa)	B_{max} (Mpa)	ν	$\Upsilon_{max,oct}$
2	130	45	1.6	27	126	0.4	0.033
10	100	27	1.6	16	74.7	0.4	0.033
20	152	61	1.6	37	172.7	0.4	0.033

* V_s, shear wave velocity; G_{max}, small-strain shear modulus; B_{max}, small-strain Bulk modulus; S_u, undrained shear sterngth ν, poisson ratio; $\Upsilon_{max,oct}$, Octahedral shear strain

Boundary condition of the pile tip for the 30m soil profile is modelled as a hinge connection because the pile is assumed to behave as a long flexible pile due to its high slenderness ratio (L/d). For the 17m soil profile, practically, the pile tip must be socketed into the stiff stratum in order to avoid rigid type behavior of the short pile associated with lower lateral capacity and excessive pile head rotation. Therefore, a fully fixed boundary condition is assumed for the pile tip in the 17m soil profile.

The structural components in the lumped mass system, which influence soil-structure interaction, are the column-to-deck connection type and the kinematic restraint at the deck. In practice, the top of the pier column is connected to the deck either monolithically in all degrees of freedom or by the bearing element. According to the Caltrans (2013) guidelines, the bearings isolate the bridge deck from transmission of seismic moments from the pier column while it allows for the displacement transmission, and can be modelled as a hinge connection. The kinematic restraint, specifically the rotational one, is crucial for realistic simulation of the seismic displacement demand in the lumped mass model (Anastasopoulos et al. 2015). The rotational spring is used herein to approximately capture the effect of the rotational restraint. If deck is rigidly connected to the abutment, the rotational stiffness would be equal to the torsional stiffness of the deck (k_{rd}) given as below:

$$k_{rd} = \frac{GJ_{eff}}{L} \tag{5.1}$$

where G=shear modulus of the deck, J_{eff}=torsional moment of inertia for the cracked deck and L=distance to the abutment. Since in reality, the deck is connected to the abutment though the bearing elements, the overall rotational stiffness is equal to that of the equivalent system of two springs in series, and less than that of the case with deck rigidly connected to the abutment. Therefore, the stiffness of the rotational spring used herein is calculated

by Eq.5.1 in which $J_{eff} = 0.2J_g$ (Caltrans 2013), and then divided by a factor of 2 to include contribution of the rotational compliance of the bearing support at the abutment.

5.2.2. Design of Representative Bridge Column

The structural design process involves determination of the design loads, dimensions of the pier-column and area of the reinforcing steel rebar. The RC pier column is designed to sustain the static dead loads and the seismic demands by the earthquake ground motions. According to the AASHTO (2012) guidelines and assumed geometry of the bridge, the total dead load of the deck is calculated 13 Mg/m, resulting in the total lumped mass of 400 Mg. Seismic design of the RC column follows the conventional design method assuming full fixity of the pier-column's base subjected to the free field ground motion. The RC column is designed to withstand the most devastating strong seismic motions recorded during the past major earthquakes. Thus, a suite of twelve real-world ground motions, which covers a broad range of loading frequency content and amplitude, is employed as the seismic excitation, whose characteristics are listed in Table 5.3. The design ground acceleration is adopted as the maximum of the spectral values in the 5% damped acceleration response spectra of the ground surface motions which are obtained from the site response analysis. Designing the RC column as a ductile member, the maximum displacement ductility demand (μ_D) is taken 3 in accordance with the Caltrans (2013) guidelines, yielding to the design spectral acceleration of $S_a = 0.61g$. Given this design acceleration, the cross section of the RC column is designed circular with 1.60m in diameter and reinforcing steel rebar area of 0.025m^2. Fig. 5.4 illustrates the fiber section layout and the cyclic moment-curvature response of the designed cross section of the pier

column. The moment-curvature analysis is performed using the OpenSees program, resulting in the yield moment capacity of 9.8 MN.m under the factored axial load of 4500 KN. According to the AASHTO (2012) LRFD design approach, the dead load must be multiplied by a factor of 1.2 for the extreme loading scenarios. The unconfined compressive strength (f_c') of 35 MPa is used to define compressive strength of the concrete sections. The compressive strength of the confined concrete core is determined as 40.5 MPa based on the work by Mander et al. (1988). The longitudinal reinforcing rebars are modelled with the elasticity modulus (E) of 200GPa, yield strength of 475 MPa and strain hardening ratio of 1%.

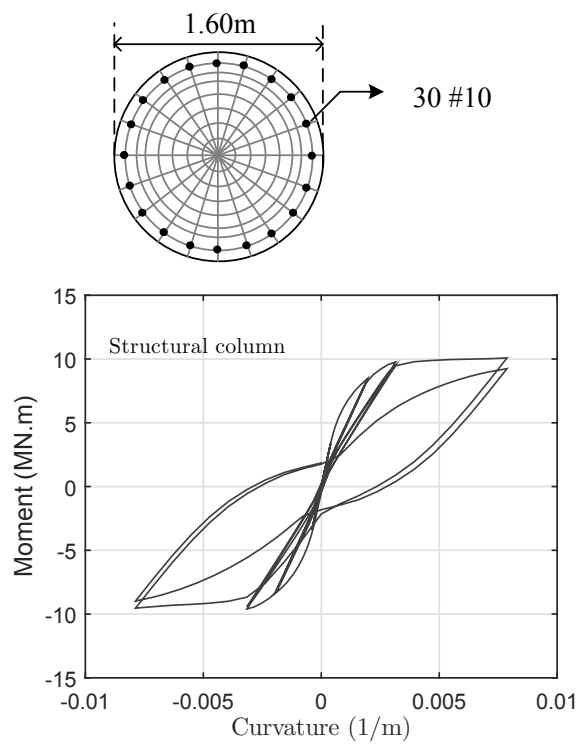

Figure 5.4. Schematic of the designed cross section of the RC shaft and its moment-curvature response

5.2.3. Design of Pile Shaft

Design of the foundation for lateral loading typically controls the shaft diameter. In this study, type II pile shaft is considered to support the bridge superstructure for the two following criteria; (1) pile shaft remains elastic through the strongest earthquake scenario, and (2) pile shaft provides sufficient lateral capacity in the target soft clay with low shear strength. Pile shaft is designed following the AASHTO (2012) guidelines for the LRFD design method. In this limit state approach, the force and resistance components are related by the appropriate factors.

The maximum design values of the seismic inertial demands transmitted from the bridge superstructure to the top of the foundation shaft can be estimated by the ultimate moment capacity of the pier-column, considering that flexural yielding of the pier column is permitted under design earthquake scenarios. It means that upon formation of the plastic hinge at the bottom of the pier column, it would be unable to transfer seismic moments in excess of the plastic hinge capacity and the respective shear forces. Thus, the shear and moment capacity of the pier column are considered as the force demands for the foundation design. On the other hand, according to the Caltrans (2013) guidelines, the pile shaft diameter must be at least 24 inches larger than that of the bridge pier column. Thus, the pile shaft diameter is tentatively determined to be 2.3m, and then this value is verified to ensure that sufficient lateral pile capacity is provided. Assuming the steel rebar area ratio ($\rho = A_s/A_g$) of 0.015 and the given rebar area extended from the pier-column below ground, the RC cross section of the pile shaft is designed. Fig.5.5 shows the fiber discretization of the shaft cross section and the corresponding moment-curvature response.

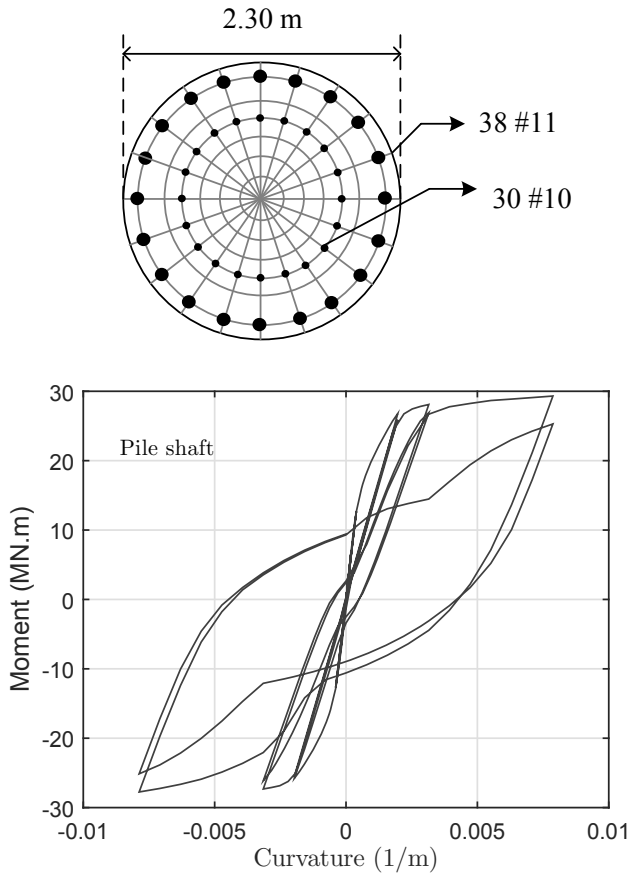

Figure 5.5. Schematic of the designed cross section of the pile shaft and its moment-curvature response

A number of displacement-controlled push-over analyses are carried out using rigorous 3D finite element model to determine the lateral pile capacity. The reason for using finite element method is that it is capable of accounting for nonlinear coupling between the translational and rotational degrees of freedom in mobilizing the ultimate lateral pile capacity. Due to this coupling effect, a pile foundation shows different lateral bearing capacities under different combinations of the lateral and moment forces. Therefore, it is essential to characterize the lateral bearing capacity of the pile under the loading condition as transmitted from the bridge superstructure to the pile head. In the SSI-

excluding design approach (fixed-base structure), base shear-moment relationship is governed by the structural constraints including the connection type (bearing or monolithic) and the deck's rotational stiffness. For the pinned column-deck case, the column acts as a cantilever beam with the maximum moment at the pile head while for the monolithic case, depending on stiffness of the rotational spring, length of the cantilever arm ranges from zero to the column height. Therefore, lateral bearing capacity of the pile shaft is characterized by performing push-over analysis for three cases involving pure horizontal force with no moment and horizontal force-moment combinations corresponding to the cantilever loading condition (hinged column-to-deck connection) for the column height of 6m and 10m. In these analyses, lateral displacement increments are applied monotonically while the pile shaft is subjected to the axial load equal to weight of the superstructure, and the resultant displacement are recorded.

Moreover, monotonic push-over analysis is performed on the fixed-base lumped mass system in order to determine the ultimate moment and shear demands applied to the pile head. The P-Δ effect is considered in the analysis to account for the base moment induced by offset axial loads.

Fig.5.6a shows the inelastic lateral force-displacement response of the pile shaft, recorded at the pile head from the push-over analyses, and compares it between the three structural heights that produce moment at the pile head. In fact, this plot reveals significant influence of the inelastic coupling between the rotational and translational degrees of freedom on reduction of the lateral bearing capacity of the pile, resulting in lower lateral pile capacity as the level of the applied moment increases. To verify the design adequacy against lateral load, Fig.5.6 a and b compares the ultimate base shear computed as the

plastic moment capacity (M_{pc}) of the structural column, divided by the column's height with the factored resistance which is 67% of the capacity from the push-over analysis according to the LRFD design method. It is shown that the base shear demands for both 6m and 10m column heights are well below the design criteria.

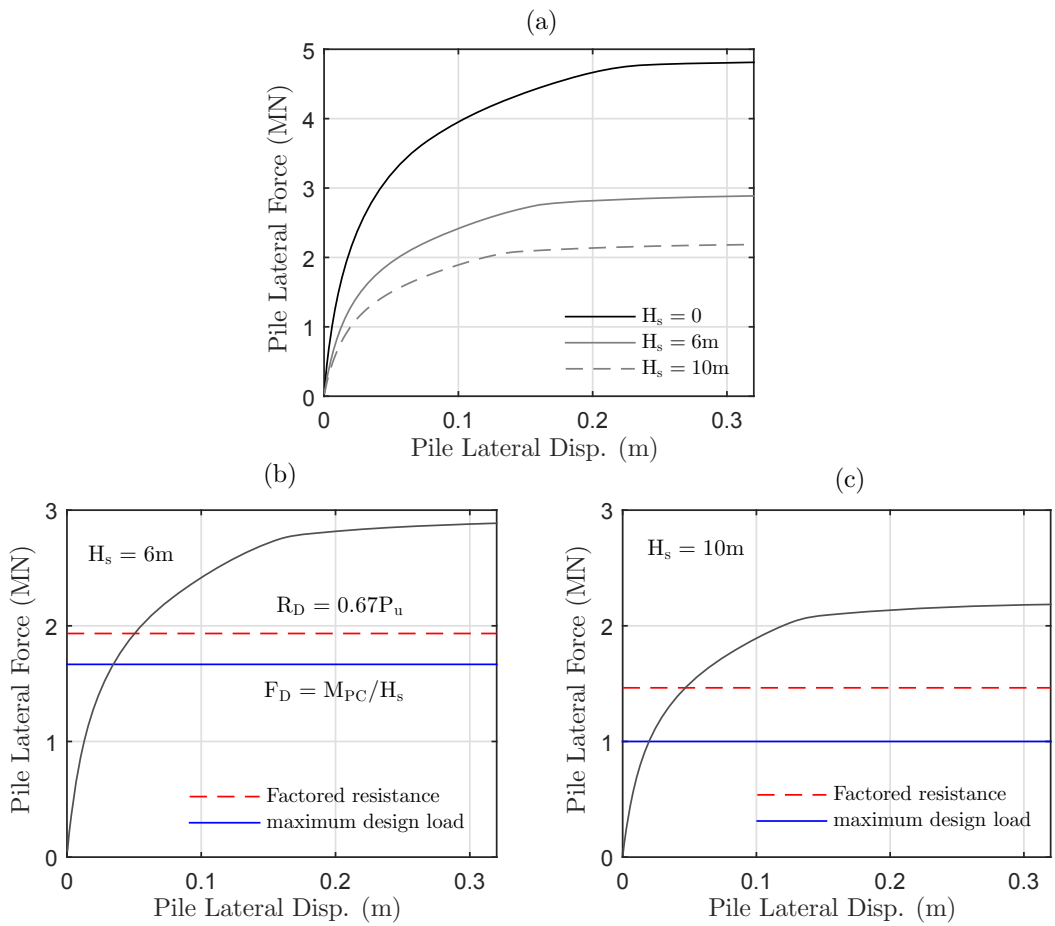

Figure 5.6. Inelastic lateral force-displacement response of the pile shaft a) three structural height, b,c) verifying design adequacy based on the AASHTO LRFD

5.2.4. Development of Finite Element Model and Simulation Details

Three dimensional (3D), nonlinear fully coupled finite element analyses of the soil-pile-structure interaction for a bridge structure supported by the large diameter RC extended pile shaft in soft clay are performed in the OpenSees platform. Spatial discretization of the soil domain is carried out in the cylindrical coordination as shown in Fig.5.7. Such a mesh generation has two advantages; *first*, it results in lower number of the elements, leading to considerable reduction in computational cost. *Second*, it increases number of the elements adjacent to the pile interface, which in turn would enhance accuracy of capturing soil-pile interaction. Moreover, increased number of the soil-pile interface elements (contact element) significantly improves stability of the numerical solution. The cylindrical soil domain has a radius of 35m, with the lateral boundaries placed far away enough (fifteen times the pile diameter) from the pile interface in order to appropriately simulate radiation damping of the seismic waves emanating from the structural system and avoid their reflection back to the model.

3D 8-node Brick elements are used to model the soil domain, with the PIMY constitutive model assigned to each element to simulate inelastic soil response. Each node of the element has three translational degrees of freedom. The nodes with equal elevations at the lateral circumference of the cylindrical soil domain are tied together using the equalDOF command in the OpenSees to undergo the same displacements in all three directions. Due to the model symmetry, only half of the model in the direction perpendicular to the seismic input excitation is analyzed. The maximum element size in the direction of wave propagation was determined as one-tenth of the minimum wavelength of the system (10 nodes per wavelength) to ensure high-frequency resolution of the soil

response. Accordingly, the upper boundary value for the maximum grid spacing was given by $\Delta Z_{max} \leq V_s/10f_{max}$ where f_{max} is the maximum frequency (5Hz) in the system and V_s is the average shear wave velocity of the soil due to cyclic deformation. Accordingly, the element sizes of 0.5m and 1m are used in discretization of the vertical direction. In total, the halved soil domain is comprised of 16072 nodes and 14400 elements, resulting in 48216 degrees-of freedom (DOFs).

An energy-absorbing boundary condition was used at the base to limit the large unrealistic reflection of the seismic wave back into the model due to rigid base assumption. This is accomplished by employing the approach proposed by Joyner and Chen (1975), in which a viscous dashpot represents the bedrock stiffness, and input motion is applied as an equivalent force developed from the velocity conversion of the earthquake record. It is worth noting that the recorded rock outcrop motion can be directly applied with the energy-absorbing boundary condition (Kwok et al. 2007).

Three-dimensional fiber section nonlinear displacement-based beam-column elements are adopted to model the bridge pier-column and the enlarged pile shaft. Each node of the beam-column element has six degrees of freedom. A "*P*-Δ" geometric transformation command is used to capture the moment effect induced by the offset superstructure mass and nodal forces along the pier-column and the pile shaft. Three-dimensional beam-to-node contact elements (Petek 2006) are adopted to model the gap and slippage at the soil-pile interface as shown in Fig.5.8

Given the strength properties of the designed structural column, Table 5.2 presents description of the bridge superstructure model used in the parametric study. The given first

mode frequency of the superstructure is obtained from the eigenvalue analysis in OpenSees.

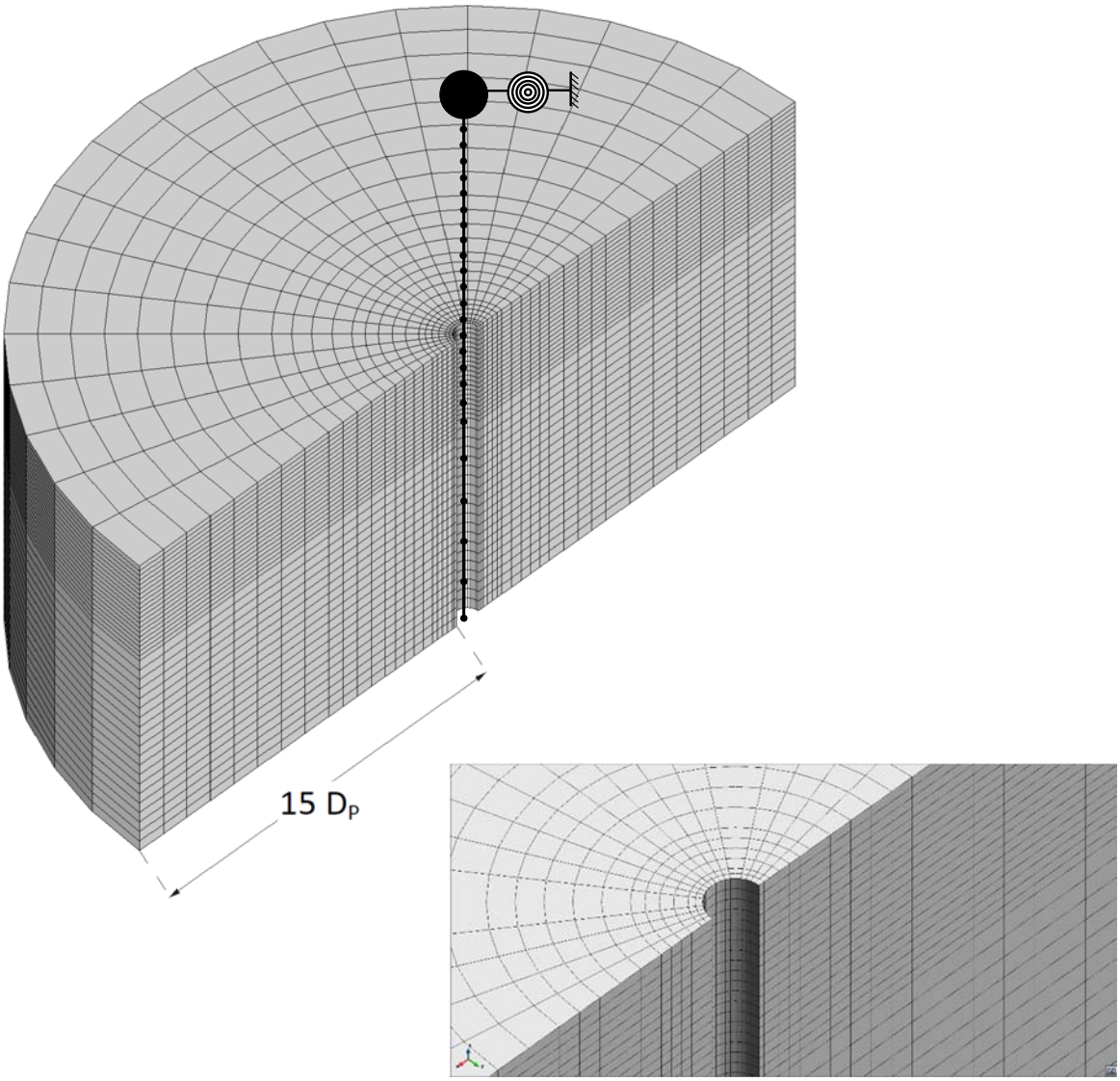

Figure 5.7. Schematic layout of the 3D cylindrical finite element model of soil-pile-structure interaction in OpenSees

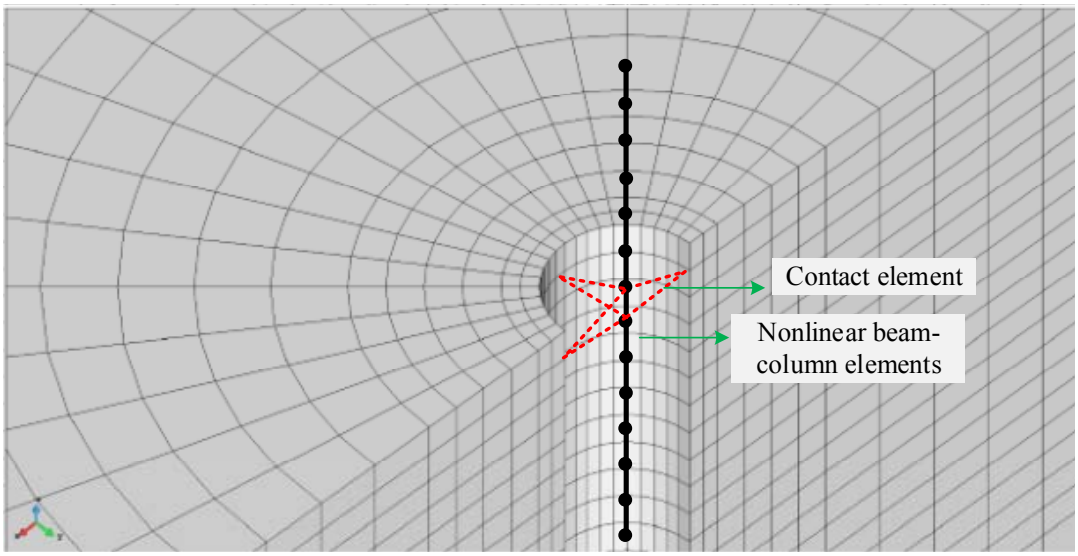

Figure 5.8. Configuration of contact elements at soil-pile interface

Table 5.2. Description of the structural parameters

structure height (m)	deck-column joint	first mode frequency (Hz)	EI $_{elastic}$ (MPa)	k_{rd} (MN.m)
6	free	2.83	8500	—
	constrained	3.1	8500	640
10	free	1.3	8500	—
	constrained	1.55	8500	640

* EI: flexural stiffness of the structural column; K_{rd}: stiffness of the rotational spring

5.2.5. Input Earthquake Motions

In performance-based design of structures, one approach for damage assessment is to perform incremental dynamic nonlinear analysis using a suite of appropriate ground motions being likely to cause damage or collapse. Previous studies have reported on the influence of the near-fault ground motions containing strong velocity pulses on the inelastic

response of structures (Alavi and Krawlinker 2000). One cause of these short-duration large pulses is the forward-directivity effect in the near fault region (Baker 2007). This type of earthquake motions is of significant interest in earthquake analyses because the large seismic demands they impose on the structure is not predicted by the typical response spectra used in design (Bertero et al. 1978, Alavi and Krawlinker 2000). The immense imposed demand can be justified by the fact that input energy to the system is directly proportional to the velocity amplitude in the input earthquake motion. It has also been shown that detrimental effect of SPSI on bridge structures can be significantly elevated when subjected to the near-fault ground motions (Hutchinson et al. 2001). Therefore, the soil-pile-structure system is subjected to two distinct sets of the earthquake shakings, involving eight near-fault and four far-fault crustal motions. Each set of motions includes variety of the frequency content and amplitudes ranging between 0.05-0.8g in order to induce different levels of inelastic interaction in the system. All of the motions were selected from the Pacific Earthquake Engineering Research Center (PEER) ground motion data base (PEER-NGA). Selection criteria for the near-fault motions follow the quantitative identifying procedure proposed by Baker (2007). Majority of the selected motions are the rock outcrop earthquake records so that they can be directly applied to the base of the model without need for the deconvolution process. However, three of the near fault motions are the records from the stiff soil site (V_{s30}~$300\ m/s$). Thus, these records are deconvolved over the 30m soil profile with uniform V_s equal to the reported $V_{s,30}$ at the recording site. Table 5.3 lists the selected earthquake records with their seismological characteristics.

Table 5.3. Earthquake records used in this study

Event No.	Earthquake	PEER-NGA No.	R_{jb} (Km)	V_{s30} (m/s)	T_P (sec.)	T_m (sec.)	PGA (g)	PGV (cm/s)
1	2010 Val-des-Bois, QC	—	—	2800	—	0.11	0.04	0.83
2	2010 Val-des-Bois, UHS	—	—	2800	—	0.3	0.22	9.6
3	Loma Prieta (1989)	765	8.8	1426	—	0.29	0.41	31
4	kobe (1995)	1111	7.1	609	—	0.49	0.51	37
			Near-Fault motions					
5	Kocaeli (1999)	1161	7.6	792	5.9	0.68	0.26	45
6	L'Aquila (2009)	4483	0	717	2	0.65	0.36	36
7	Loma Prieta (1989)*	802	7.1	380	4.6	0.55	0.33	46
8	Morgan Hill (1984)	451	3.6	561	1.1	0.42	0.7	53
9	Tabas (1978)	143	1.8	767	6.19	0.47	0.85	121
10	Kobe (1995)*	1120	1.46	256	1.6	1.1	0.62	121
11	Northridge (1994)*	1063	0	282	1.25	0.92	0.83	112
12	Chi-Chi (1999)	1529	1.5	714	9.6	1.4	0.3	91

T_p: period of the velocity pulse

T_m: mean period of the motion following Rathje et al. (2008)

* the motion is deconvoluted over the 30m soil profile with V_s=$V_{s,30}$

5.3. Validation of Continuum Model

Results of two soil-structure interaction centrifuge experiments are utilized herein to validate reliability of the continuum model for nonlinear SSI problems. A centrifuge test conducted by Rayhani and Elnaggar (2007) for evaluation of nonlinear SSI effects in shallow foundation is simulated using the 3D finite element method. Fig.5.9 shows the schematic layout of the centrifuge model. In this experiment, the test model was spun in a centrifuge at a radial acceleration of 80 g. A rigid hollow aluminum box with dimensions of 5.5m in length, 2.5m in width and 6m in height in prototype scale was placed on top of a synthesized soft clay material called Glyben. This box was embedded 2 m deep in the soil, representing a shallow foundation. A rigid walled soil container with dimensions of 0.73m length, 0.3m width and 0.57m height was used to contain the soil-structure model, simulating a uniform 30 m deep soil layer in the prototype scale. Table 5.5 summarizes input parameters of the Glyben for the PIMY constitutive soil model used in the numerical simulation.

Representative simulation results including 5% damped response spectra and time histories of the computed and recorded accelerations at various locations in the model are presented in Fig. 5.6. These locations include the free field (ACC1), underneath the structure (ACC2), the foundation (ACC3) at depths of 3.5 m, 4m and 1m respectively and the top of the structure (ACC4). Satisfactory agreement was observed between recorded and computed accelerations over both the time and frequency ranges at all locations except for ACC1. As observed in the acceleration response spectra (ARS) corresponding to ACC1, some spectral ordinates corresponding to a narrow frequency range of about 2–5 Hz were not reproduced by the numerical model accurately. Almost the same discrepancy was observed for the

other accelerometers (ACC5 and ACC7) located at deeper levels of free field. Considering that ACC1 represents free field motion, such a discrepancy can be mainly due to numerical limitations in modeling the rigid boundary condition where some frequencies are amplified. In general, comparison of experimental and numerical results demonstrates the capability of the elasto-plastic soil constitutive model in simulating a nonlinear dynamic SSI problem.

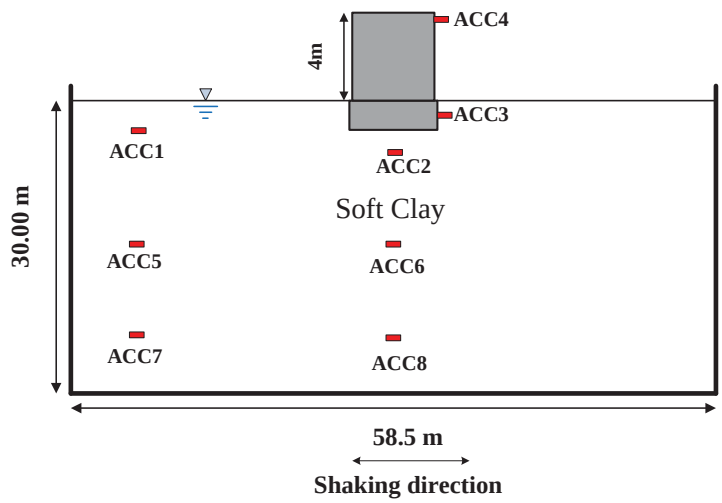

Figure 5.9. SSI centrifuge model (Rayhani and Elnaggar 2007)

Table 5.4. Input soft clay parameter

Model Soil Parameters	Parameter Index	Value
Bulk mass density (kg/m^3)	ρ	1575
Shear modulus (kPa)	G_{max}	9600
Bulk modulus (kPa)	B	65380
Undrained shear strength (kPa)	S_u	50
Undrained friction angle	φ_u	0
Poisson ratio	ν	0.43
Reference confining pressure (kPa)	P_r	100
Peak shear strain	Υ_{max}	0.1

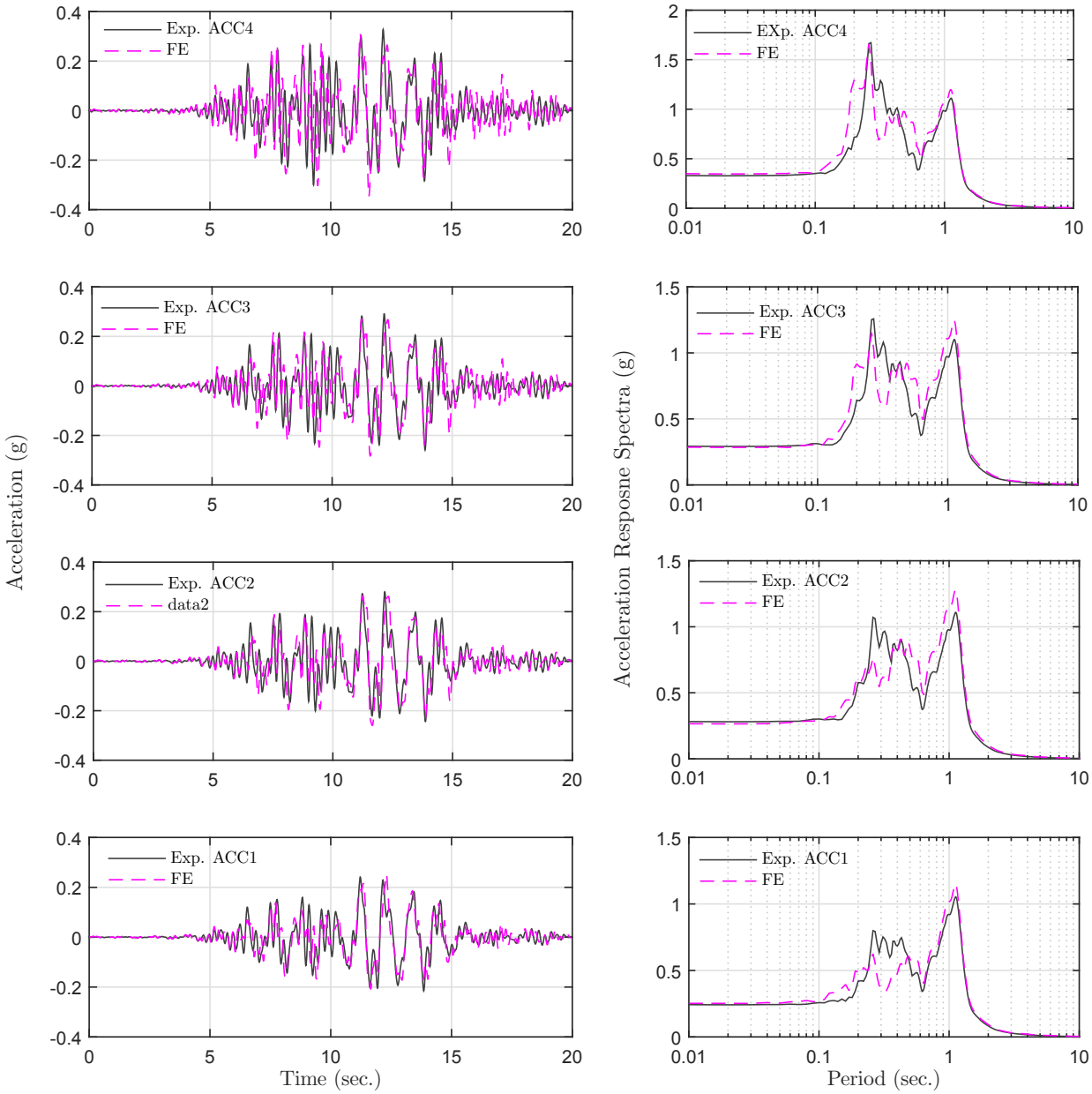

Figure 5.10. Comparison between the results of experimental and simulated SSI model

The centrifuge test (CSP5-B) conducted by Wilson (1998) is also simulated by the continuum finite element model in order to verify its capability specifically in capturing the nonlinear dynamic soil-pile-structure interaction in soft clay. Details of the centrifuge model are shown schematically in Fig.5.11. As shown, the model consists of two soil layers including 6.1 m of very soft reconstituted San Francisco Bay mud as the top layer underlain by 11.4m layer of dense Nevada sand layer. The soil domain has dimensions of 51.6m long, 20.5m wide and 21m deep in the prototype scale. The lumped mass-bar system used in the model represents a prototype steel pipe pile with the length of 16.5m, supporting a mass of 49.1 Mg. The finite element model of the centrifuge test is developed with a similar procedure explained in Section 5.2.2. The PIMY constitutive model is used to model the soft clay behavior, and its effective stress version, PDMY (pressure-dependent multi-yield surface) model, is employed to model the stress-strain behavior of the sandy soil. The input parameters for the clay layer are adopted from the Torvane test measurements for the undrained shear strength (C_u) which is adjusted for the high strain rate effect of the centrifuge test, and the approximate equation of $G_{max}=250C_u$. The initial value of this ratio is based on the correlation proposed by Dickenson (1994) for undisturbed Bay mud. This ratio is adjusted for the disturbance effect and to better capture the natural system frequencies observed in the experimental results. The parameters for the dense Sandy layer are adopted from the values reported by IIankatharan (2008) for Nevada sand with 80% relative density. Fig.5.12 compares the 5% damped ARS of the measured and computed motions at the free field ground surface and the superstructure in the centrifuge test. As shown, very satisfactory match is observed between the two spectral responses in both

locations, confirming capability of the continuum model used in this study in capturing nonlinear SPSI.

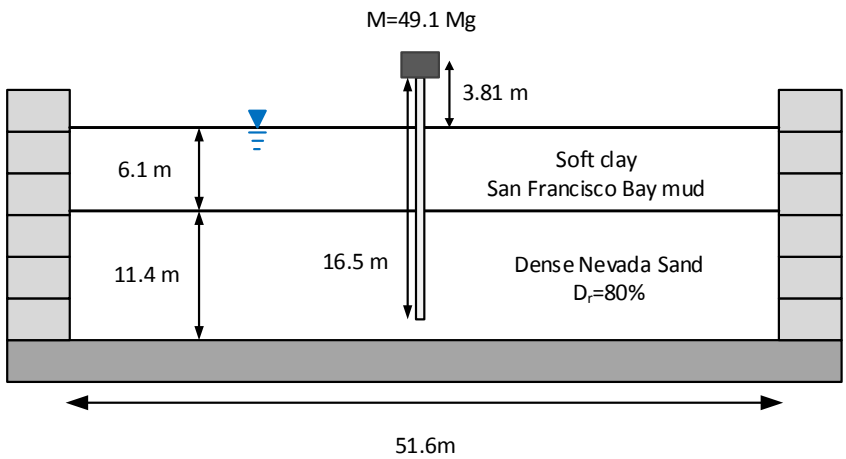

Figure 5.11. SPSI centrifuge model (Wilson 1998)

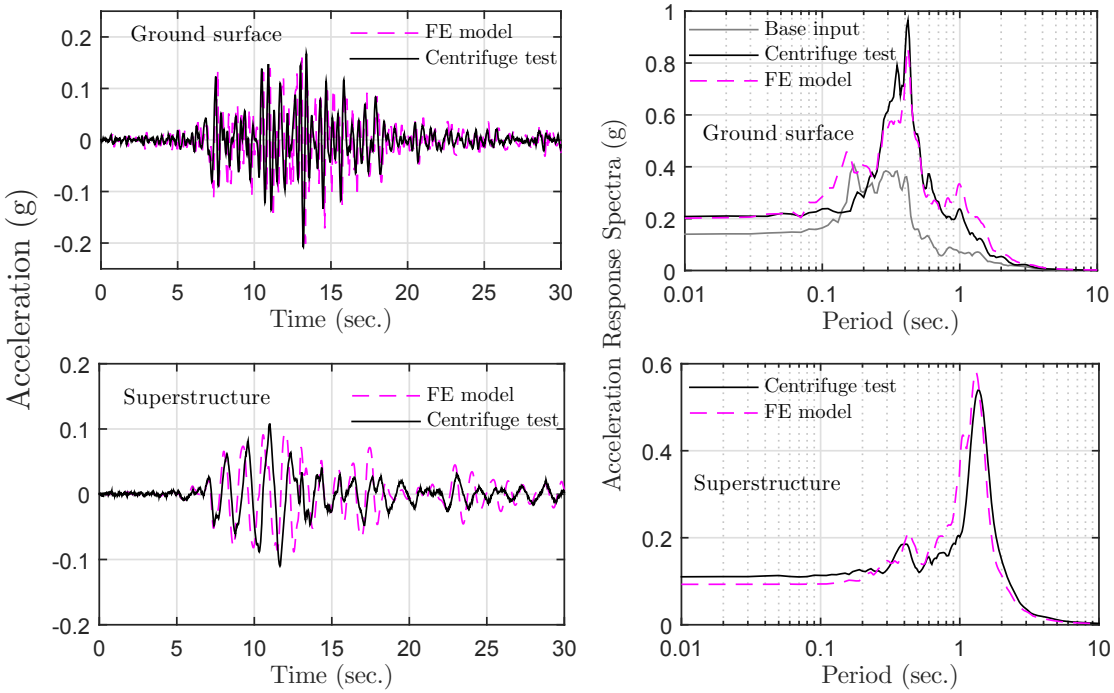

Figure 5.12. Comparison between the results of experimental and simulated SPSI models

5.4. Simulation Results

In this section, results of a comprehensive parametric analysis evaluating influence of the nonlinear SPSI on seismic response of a RC shaft-supported bridge are presented and discussed. Site soil effect, lateral pile performance, structural components and input shaking levels are the subjects of the parametric analyses, as described in the section 5.2.1. For characterization of the SPSI effect and its underlying causes, results are presented and discussed in two categories including moment and subgrade reaction developed along the pile shaft and pier-column displacement demand.

5.4.1. Free Field Soil Response

In any SSI analysis, it is very important to identify vibrational characteristics of the free field soil response as the source of input excitation to the soil-structure system. Site response analysis is performed for all the input motions listed in Table 5.3, with the same modelling procedure as described in Chapter 4. The 5% damped response spectra of the free field ground motions are used to identify the natural frequency, the spectral amplification factors and the frequency content of the inelastic site response. The spectral amplification factors are estimated using the ARS ratio of the computed ground surface and input base motions given as follows:

$$AF(T) = \frac{ARS(T)_s}{ARS(T)_b} \tag{5.2}$$

Fig.5.13 shows estimated spectral amplification factors for the 17m (site 1) and 30m (site 2) soil profiles subjected to the earthquake events of No.3 (NGA 765) and No.11 (NGA

1120), being representative of the far-fault (FF) and near-fault (NF) motions, respectively. For both the soil profiles, the input spectra are shown to be severely damped under the near-fault ground motion over the entire period range while the amplification factors of up to 3 is observed for the far-fault motion with the input PGA of 0.4g. This is because of the large relatively long- period velocity pulse in the near-fault motion, which renders soil softening and consequently shifts the natural site period to longer periods. The range of natural site periods resulted from all the earthquake events is determined by computing the peak amplification spectra and its corresponding period. The obtained periods range between 0.8 sec.-3 sec. for the 30m site and 0.5 sec.-3 sec. for the 17m site.

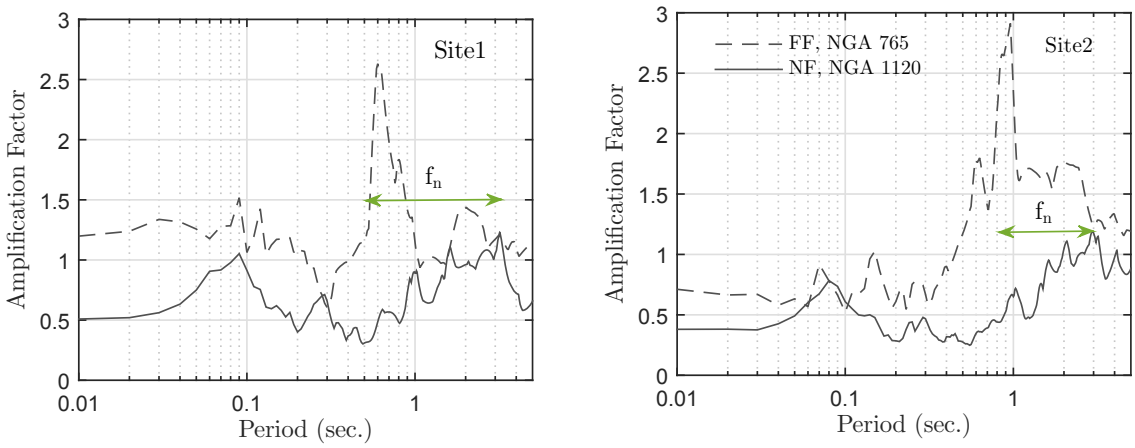

Figure 5.13. Spectral amplification factors for the two soil sites subjected to representative far-fault and near-fault motions

The profiles of the induced maximum shear strain along the soil profile and the peak displacement response of the soil are illustrated in Fig.5.14 and Fig. 5.15, respectively, for the two FF and three NF representative motions in order to discriminate effects of the NF motions from the FF ones. In fact, these profiles correspond to the strain and displacement

responses at the instance of the peak displacement ($u_{g,max}$) which occurs at the ground surface. The distinct effect of the FF motion is shown to be shear failure at the boundary between the soft layer and the underlying stiffer one. Such an enormous in-depth shear strain would result in the large displacement of the soil mass up to 70 cm in the upper layers while the maximum ground response under strong FF motions would hardly exceed 10 cm. The magnitude of the soil movement can be comparable with that of lateral spreading in the liquefiable ground, which has been shown to be very destructive to pile foundations. Thus, this huge displacement response of the shallow layer is expected to significantly impact the lateral performance of the pile-structure systems.

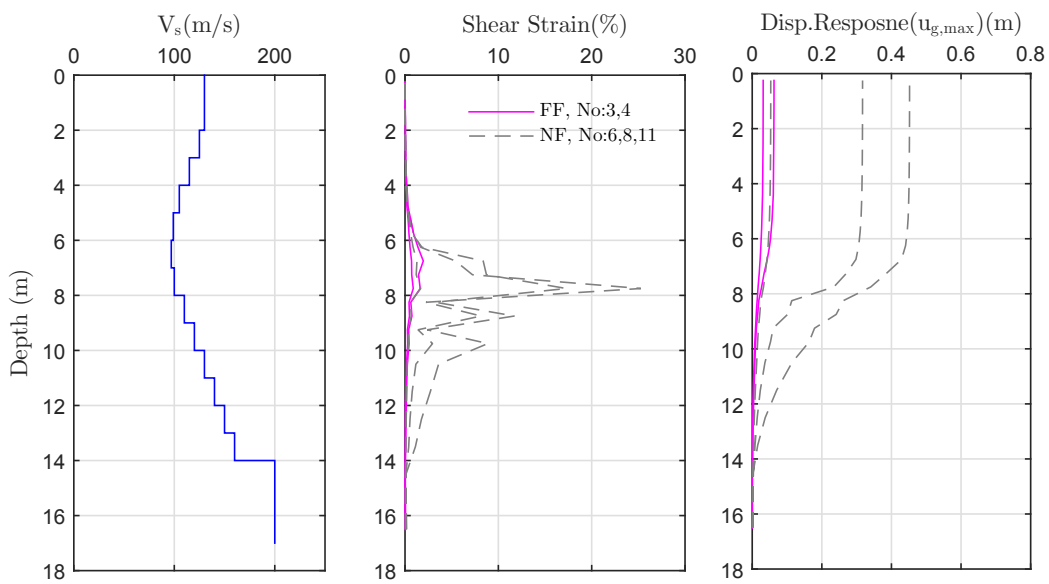

Figure 5.14. Shear strain and displacement response profiles induced under far-fault and near-fault motions for the 17m soil profile

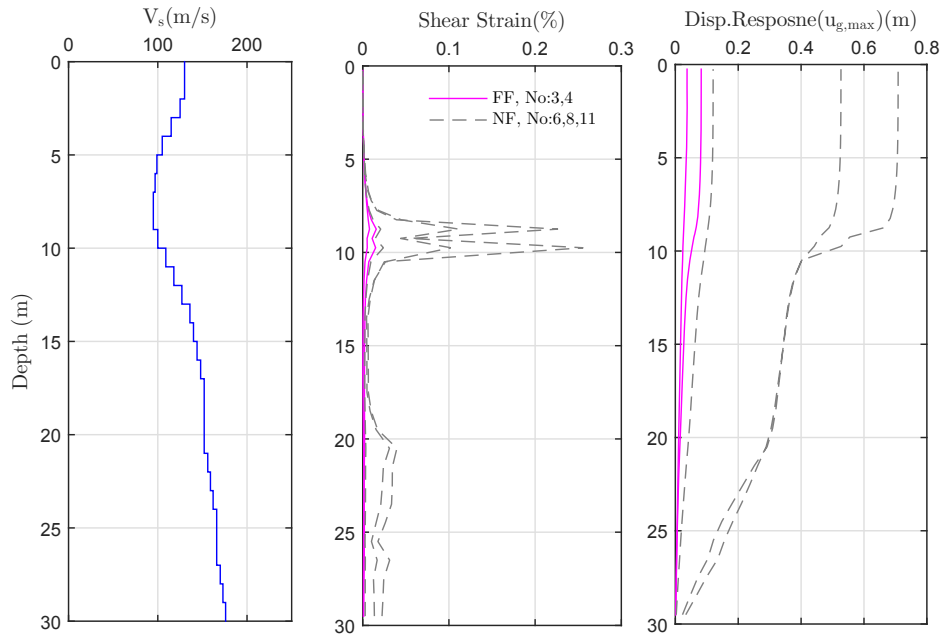

Figure 5.15. Shear strain and displacement response profiles induced under far-fault and near-fault motions for the 17m soil profile

5.4.2. Fundamental Period of the System

Period lengthening of the structure has been well recognized as the primary consequence of the soil-structure interaction due to soil flexibility. It is essential to identify the flexible-base period of the soil-structure system (f_{SSI}) in order to predict potential resonance between the free field ground motion and the vibration of the soil-structure system. The frequency-domain non-parametric system identification (Pandit 1991, Ljung et al 1987) is used in this study to determine f_{SSI} for the different cases in the parametric study. This method evaluates the complex-valued transfer function between the input and output time histories of a system, which represents frequency response of the system subjected to a unit impulse excitation. For the case of a soil-structure system in this study, the input and output motions are responses of the free field ground and the bridge deck. Although the frequency-

domain transfer function may not be appropriate for evaluating the damping ratio of a nonlinear SSI problem due to its lumped parameter nature, it can be used for identification of the natural period of the nonlinear system, which corresponds to peak spectral amplitude of the transfer function. The cross and auto power spectral density functions smoothed in time domain are used to compute the transfer function as:

$$H_u(\omega) = \frac{S_{fs}(\omega)}{S_{ff}(\omega)} \tag{5.3}$$

where $H_u(\omega)$ is the frequency-domain transfer function, S_{fg} is the cross power spectral density function for the acceleration time series of the free field and deck motions, and S_{ff} is the auto power spectra for the free field ground motion.

5.4.3. Seismic Response of the System

For the seismic design purposes, inelastic lateral response of the bridge structure and the force demands (shear and moment) along the pile shaft are considered as the crucial parameters. The importance of the inelastic response has been highlighted following the experiences from the 1995 Hanshin earthquake, which indicate that large inelastic residual rotation at the ground surface might render the bridge structure nonoperational (MacRae and Kawashima 1997). From the investigation of the structural damages, subsequent to the 1995 Hanshin earthquake, the Japan Road Association (JRA 1996) guidelines for highway bridges specified the allowable residual drift ratio of 1% for seismic design of bridges supported by reinforced concrete columns. The drift ratio is defined as the slope of the vertical above ground pier column, which is calculated herein as the relative displacement response of the superstructure mass divided by the height of the above ground pier column.

The inelastic rotation of the structure stems from the inelastic action of the soil-pile system due to compliant flexible soil and the reinforced concrete section of the column. Under soil-pile-structure interaction, the magnitude of the former rotation is rendered by the coupling between the inertial forces from the superstructure (inertial interaction) and the displacement demands from the far field soil on the pile shaft (kinematic interaction). In other words, it depends on the ground motion characteristics (natural site period and amplitude), the stiffness and period of the structure, and the inelastic foundation impedances (stiffness and damping).

5.4.3.1. Structural drift

Fig.5.16 shows the drift ratio ordinates from the continuum modelling of the fully coupled nonlinear SPSI for Site 2 with 30m hinged-tip pile and Site 1 with 17m fixed-tip (socketed) pile. In this plots, correlation between the residual drift ratio at the end of the shaking event and the maximum transient one is illustrated for four structural cases with different vibrational properties, subjected to all the earthquake events presented in Table 5.3. The versatility in the structural vibrational properties is given by the above ground heights, 6m and 10m, and the deck-level kinematic constraints, free head and the rotational spring.

While majority of the cases in Fig. 5.16 are shown to experience the γ_{res} value of equal or less than the allowable 1%, there are few pile cases with the limit exceeding γ_{res} values, which are subjected to extreme near-fault ground motions. Two prominent differences can be distinguished between the drift responses of the two pile cases in Fig.5.16, which clarify the mechanisms underlying the drift response. First, a distinct narrow-banded correlation trend is observed for the fixed-tip pile case, whereas in the hinged-tip pile, the breadth of

the trend widens with increasing the transient drift from a very small transient drift values (~1%). This is attributed to higher rotational stiffness of the fixed-tip short pile due to contribution of the flexural stiffness of the pile. This contribution is highlighted under strong shakings in which higher degree of the inelastic soil-pile interaction occurs, resulting in further softening of the surrounding soil. On the contrary, since the foundation stiffness highly depends on the interaction stiffness between soil and pile in the hinged-tip long pile, lateral pile stiffness progressively degrades with increasing the level of shear strain and the imposed lateral displacement. With this vision in mind, the fixed-tip pile foundation undergoes less impact from the vibrating superstructure due to lower structure-to-foundation stiffness ratio, in particular, the rotational stiffness.

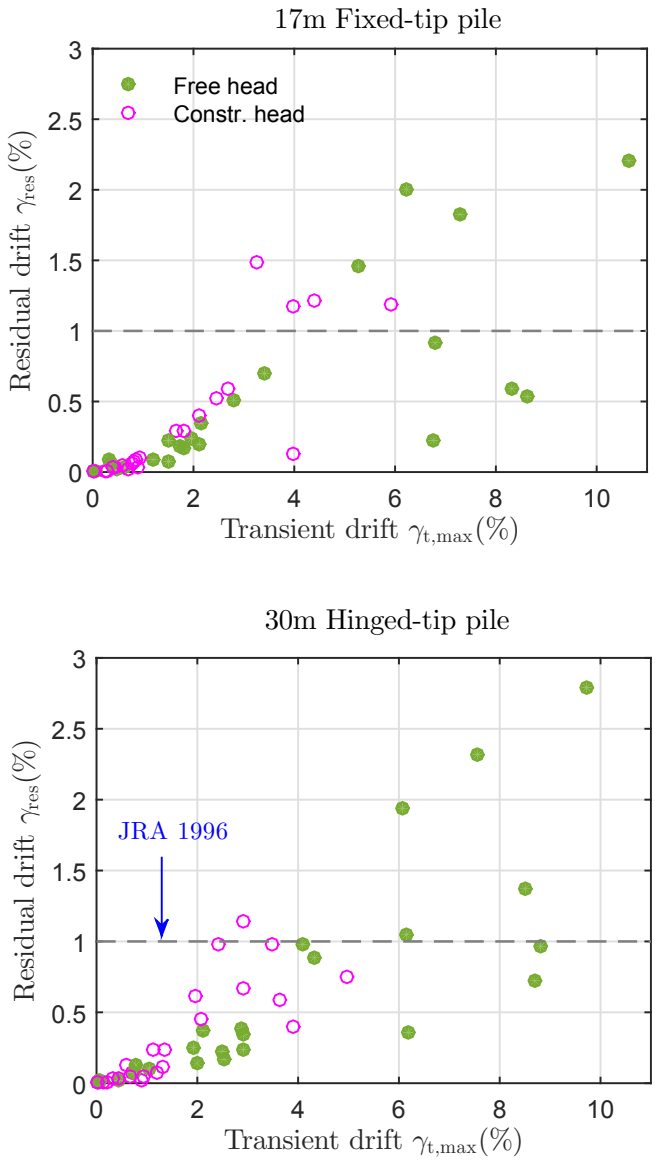

Figure 5.16. Correlation between the residual and the maximum transient drift ratios from continuum model

Second, and of special interest, the threshold transient drift ratio for the residual drift is shifted from 3% in the fixed-tip to 6% in the hinged-tip pile. Moreover, γ_{res} value in four of the rotationally-constrained structures on the fixed-tip pile exceeds the allowable 1%. These behaviours can be justified by spectral analysis of the free-field and the soil-structure motions. Fig.5.17 shows the 5% damped acceleration response spectra (ARS) of the free-field motion at the ground surface and the motion at the deck level for the structural cases subjected to event No.11 (1994 Northridge). The residual drift ratio for these cases exceeds the 1% limit. In the 30m soil profile, the free-head 10m column undergoes γ_{res} value of 2.3 %. This is because of coincidence of the natural site period of 2.9 sec. with the fundamental period of the SPSI system (f_{SSI}), resulting in such a large residual drift. In the 17m profile, the induced γ_{res} value of 1.5% in the 6m constrained-head column can be attributed to higher spectral amplitude of the ground motion at the fundamental period of the system (f_{SSI}=1.05 sec.). Comparatively, the identical structural case in the 30m profile shows γ_{res} value of 1.0% when subjected to the spectral free field acceleration equivalent to half of that in the 17m profile.

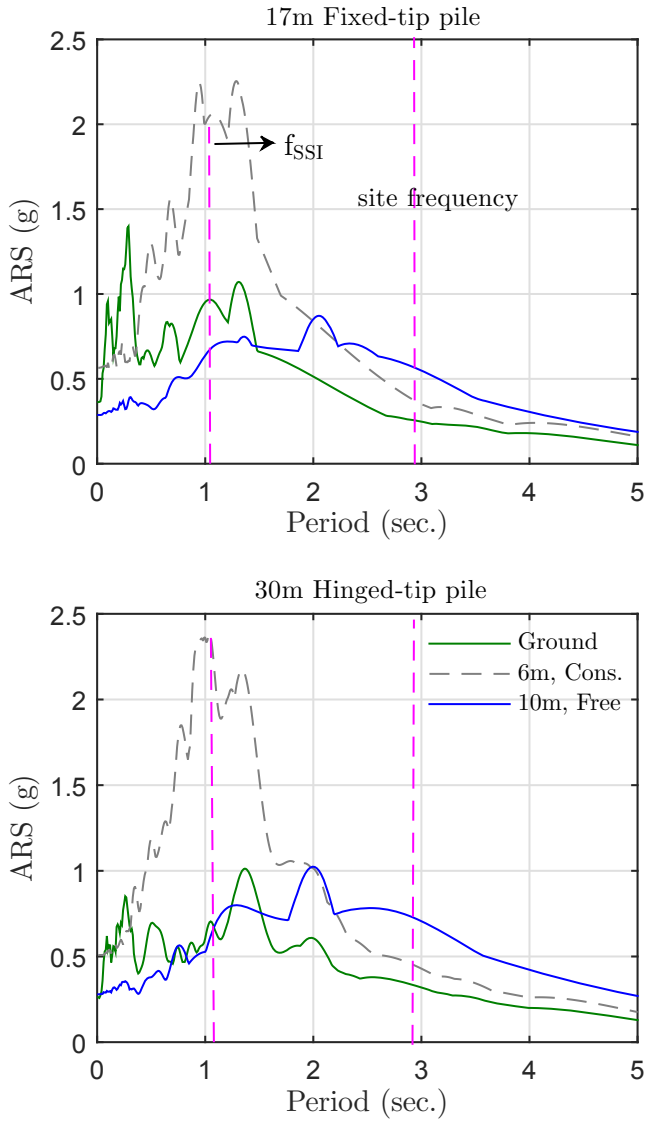

Figure 5.17. 5% damped acceleration response spectra of the free field and the superstructure motions for the 17m and 30m pile cases and two representative structural cases

5.4.3.2. Soil Curvature

Fig.5.18 shows correlation between the maximum soil curvature representing kinematic loading from soil domain and the induced maximum transient drift for the rotationally-free and constrained structural columns in two different sites and pile configurations. In fact, this plot describes how the soil curvature as an independent demand parameter contributes to overall rotation of the pier column, which is the outcome of the foundation rotation (θ_p) and the structure's response (u_b) under SSI influence and defined as:

$$\delta = u_b + H\theta_p \qquad (5.5)$$

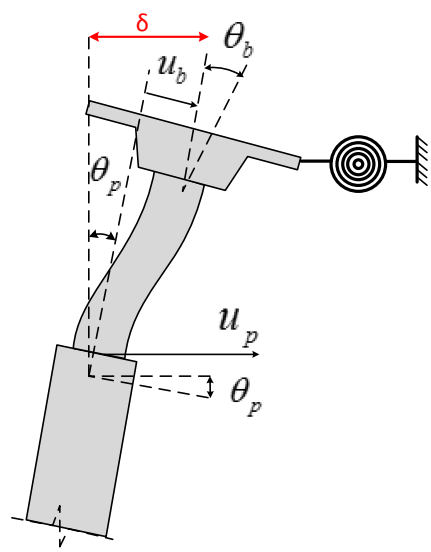

The soil curvature parameter ($1/R_s$) is used to approximately quantify deformation in the soil, which imposes curvature on the pile as the shear waves propagate vertically through the soil column. According to Margason (1975), the soil curvature over a vertical distance in the soil column is defined as:

$$(1/R_s) = \frac{2\Delta u_{ff}}{\Delta z^2} \qquad (5.6)$$

where Δu_{ff} denotes the relative lateral displacement between two elevations in the soil domain with vertical distance Δz. For the two pile cases of this study, the maximum soil curvature is computed over the active pile length at the instance of maximum displacement response of the free field soil column, at which maximum bending moment is induced along the pile shaft. Although the active pile length depends on soil-pile relative stiffness, inelastic subgrade modulus and slenderness ratio of the pile, the active length is approximately assumed 10Dp which is an average value in this case, considering increase of active pile length due to soil-pile inelastic interaction.

As expected, the maximum drift ratio in Fig.5.18 is shown to increase with increasing the soil curvature transferred to the pile shaft, resulting in rotation of the superstructure column. A best-fit exponential trend from the regression analysis is fitted to the data. Deviation of data from the trend is caused by the structure's response as given by Eq. (5.5), which depends on the spectral amplitude of the free field motion around the fundamental frequency of the system. Relatively linear relation is observed between the soil curvature and induced drift ratio in the fixed-tip pile, implying that the foundation rotation prevails the structural drift, while in the hinged-tip long pile, drift values for extreme FF motions are insensitive to soil curvature. In the latter case, it appears that consistency between the natural frequency of the SPSI system and the dominant frequency content of the free field ground motion causes larger drift vales, as comparison between the ordinates of 6m and 10m free head columns shows.

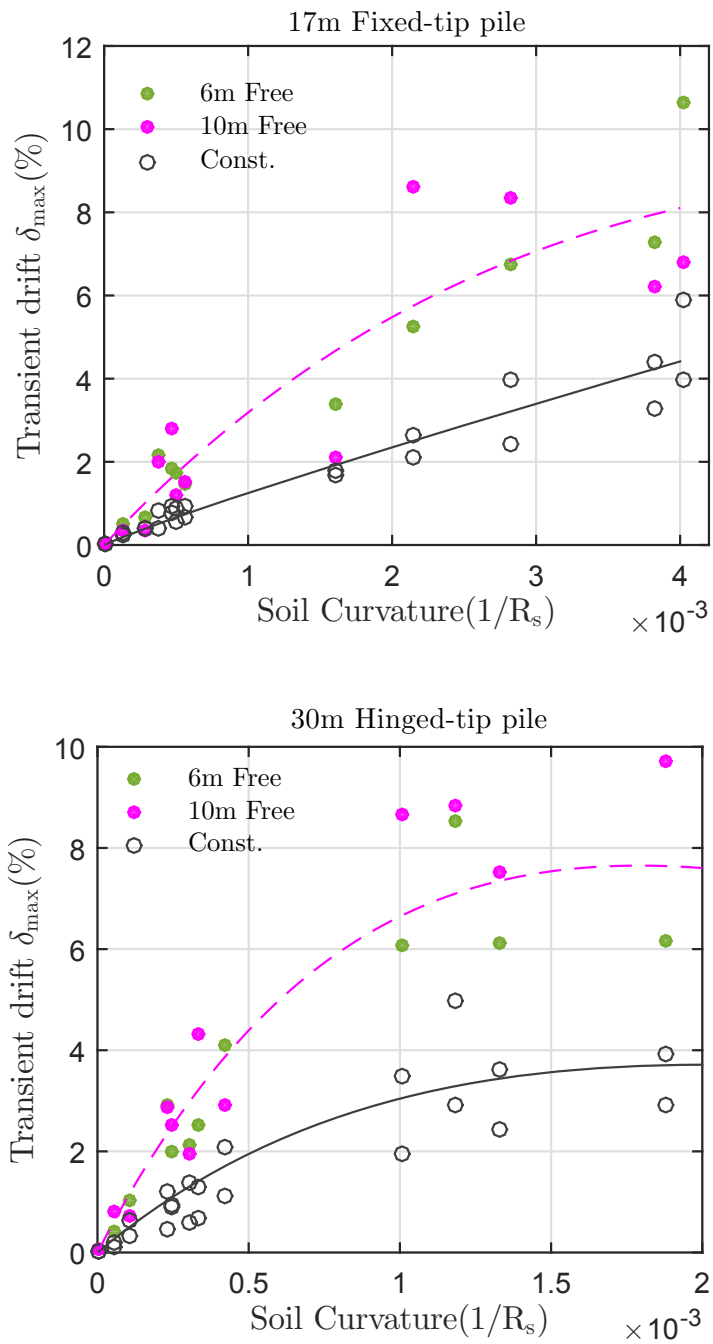

Figure 5.18. Correlation between the free field soil curvature and the maximum transient drift ratio

5.4.3.2. Bending moment profile

The induced bending moment profile along the pile shaft under kinematic and inertial interactions is the key parameter to ensure structural integrity of the foundation under seismic loading. Fig.5.19 shows the bending moment profile for all the structural cases supported by the 30m hinged-tip pile shaft, and subjected to destructive near-fault input motions. In order to evaluate yielding of the RC sections, this plot also includes the plastic moment ordinates for the structural column (M_{pc}) and the pile shaft (M_{pp}), obtained from the cyclic moment-curvature analysis. Fig.5.19 is intended to illustrate the difference between moment profiles of moderate (event No.6) and severe (event No.11, 12) NF input motions. As shown in Fig.5.19, the structural column undergoes yielding under all three shaking events as intended in the design phase. The plastic hinge develops at the deck level for constrained-head column cases, while it is developed at the ground surface for the free-head ones. Moreover, the bending moment profiles for event No.6 are controlled by the magnitude of inertial forces due to low level of the imposed displacement while in the other two high intensity events, the kinematic interaction prevails over the inertial forces, resulting in larger moment values and deeper elevation of the maximum bending moment. The maximum moment occurs at a depth of 12m below the ground surface, beneath the depth of shear failure induced by the shear wave propagation in the soil domain, as shown in Fig.5.15

The moment profiles for the 17m fixed-tip pile representing a rock-socketed short pile are shown in Fig.5.20. Formation of the plastic hinges with a length of 2-5m is observed in the two strong events (No.11, 12). This indicates that enormous amount of the lateral loads are transmitted to the pile's structure due to the base fixity and the cantilever

type lateral pile behaviour. Further, stiffness degradation around the pile shaft due to nonlinear soil-pile interaction and widening of the gap opening under strong shaking events aggravates the level of transferred loads. Of special interest, no agreement between the timing of the maximum moment in the structural column and that of the pile shaft is observed for the 10m free head pile in events No.6 and 11 and 6m free head pile in event No.8. This is caused by out of phase vibrations of the soil column and the soil-structure system, where small level of inertial forces are transmitted to the pile shaft because of lower spectral acceleration in the free field response.

Fig.5.20 compares the level of maximum bending moment induced in the two pile shaft cases during eleven earthquake events. For all the events, the maximum moment for the 30m hinged-tip shaft doesn't reach the corresponding plastic value, whereas in the 17m socketed shaft, plastic hinge is developed under NF motions with a maximum ground displacement response larger than 20 cm.

In conclusion, based on the observed bending moment profiles along the socketed and hinged tip pile shafts, designing the short piles just for lateral bearing capacity would not be adequate from seismic design prospective, in particular kinematic soil-pile interaction. One possible solution can be increasing diameter of the socketed pile shaft to increase its moment capacity.

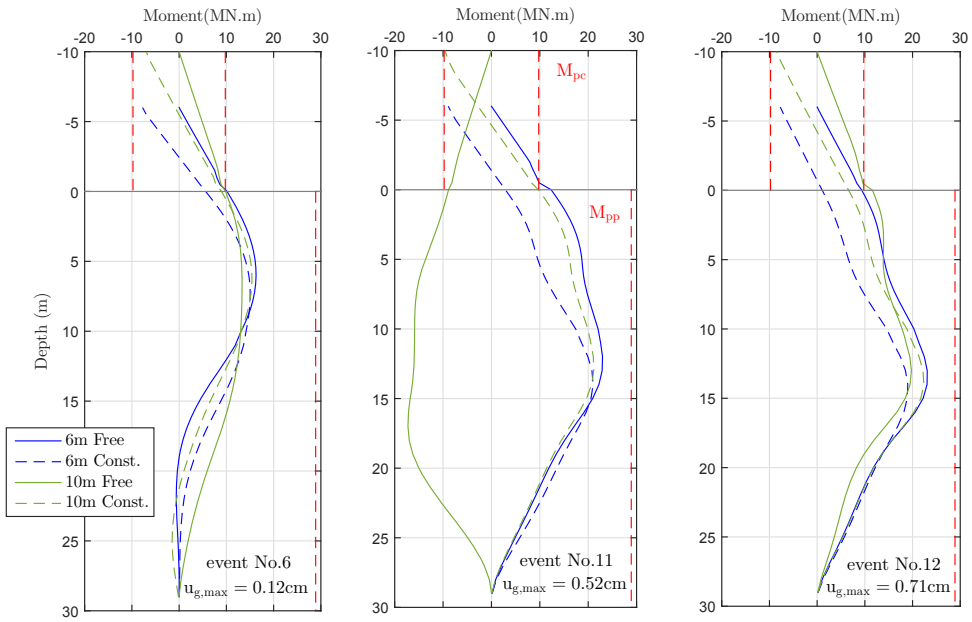

Figure 5.19. Bending moment distribution for four structural cases under moderate (event No.6) and two strong near-fault motions (event No.11, 12).

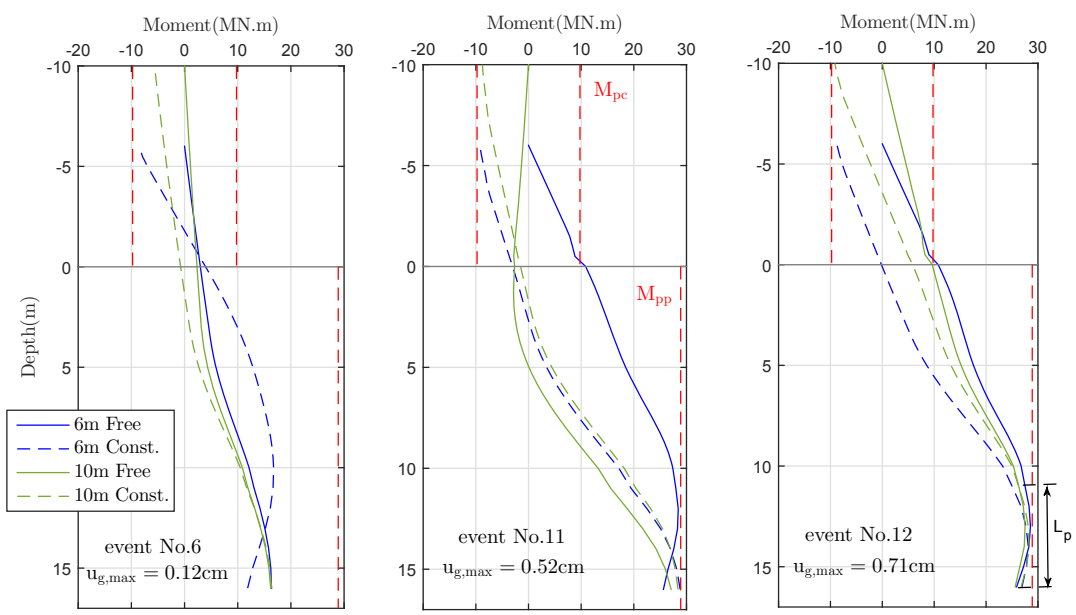

Figure 5.20. Bending moment distribution for four structural cases under moderate (event No.6) and two strong near-fault motions (event No.11, 12).

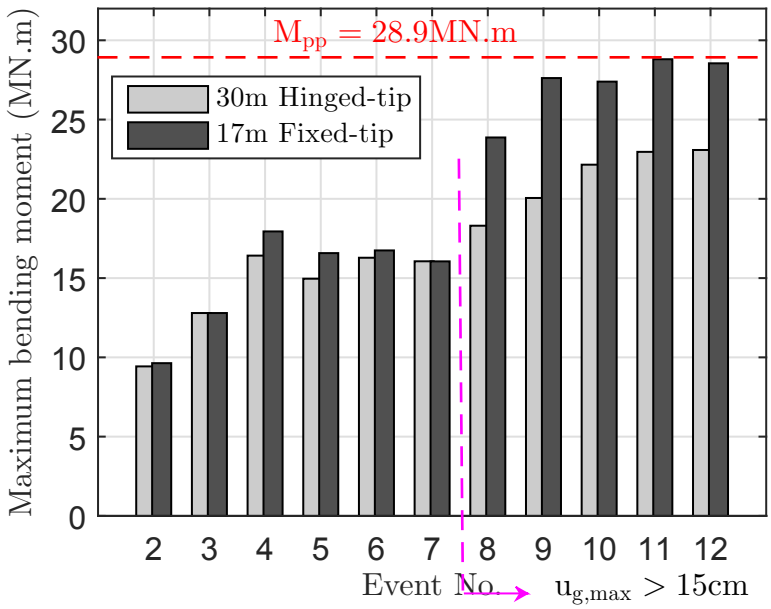

Figure 5.21. Bending moment distribution along the pile and structural column shaft for four structural cases under moderate (event No.6) and two strong near-fault motions (event No.11, 12).

Chapter 6 : A hybrid method for derivation of equivalent-linear pile head impedance functions

6.1. Introduction

The substructure, or lumped spring method is widely used for soil-structure interaction analysis of various structures. Pile head impedance functions are the key ingredients of this method, representing modulus of soil-foundation interaction force under inertial loads transferred from the structure. To this end, all proposed moduli are constrained to linear elastic soil behaviour and rigid bonding between the soil and foundation, whereas in reality and particularly in pile foundations, impedance functions can exhibit quite inelastic behaviour due to soil inelasticity and geometrical nonlinearity such as gap and slippage between the pile and soil. Both frequency and time-domain solutions of the substructure analysis can be utilized to estimate the system response for soil-structure interaction effect. Each of these solutions has its own advantages and drawbacks, such that, the substructure

analysis is performed conveniently and time-efficiently in the frequency-domain while in the time-domain counterpart, the equation of motions are solved through step-wise numerical integration approaches. The frequency domain solution uses frequency-dependent transfer function to solve the equation of motion at a desired frequency. Computation of the transfer function requires the impedance functions to be inserted to the system. Despite simplicity, the frequency-domain solution is valid for soil-structure system with linear behaviour of the components. On the contrary, the time domain solution is capable of capturing time-varying system characteristic due to soil-structure inelasticity, but realistic characterization of the nonlinear impedance function in the substructure method is quite challenging, especially for deep foundations with high degree of coupling between the swaying and rocking stiffness. This means that nonlinear load-deformation relationship representing foundation stiffness should be identified under coupled shear and moment forces from superstructure, whose actual spectral magnitude itself depends on the dynamic foundation stiffness and damping (impedance function). The second obstacle in characterization of inelastic impedance function concerns the kinematic interaction in deep foundations, that can be very significant in strong ground shaking because of large shear strains induced at deeper soil medium around the foundation and degrades the modulus of subgrade reaction. To this end, formulation of impedance functions for elastodynamic soil-pile interaction with the assumption of soil-pile interface continuity has been well addressed by previous studies through analytical (Novak 1974, kaynia 1982, Mylonakis 2005), semi-analytical (Gazetas 1984, Kagawa and Kraft 1980). This chapter presents development of a hybrid approach to derive variation of the impedance function resulted from inelastic action of the soil-structure system in the RC pile shaft supporting bridge

superstructure. The proposed method combines the superiority and accuracy of the time-domain direct method in solving inelastic soil-structure interaction with computational convenience of the frequency-domain method and the practical Winkler-based impedance function formulation for piles. The following sections describe various aspects and solution algorithm of the proposed approach.

6.2. Solution Scheme

A hybrid numerical-analytical method is developed in this study to estimate the modulus of subgrade reaction and the corresponding pile head impedance function ordinates under coupled nonlinear soil-pile-structure interaction (SPSI). The term "coupled" denotes two types of coupling mechanism existing in the SPSI. One refers to compatibility condition between the spectral inertial forces transmitted to the soil-foundation system and the corresponding mobilized foundation stiffness that alters the overall vibration period of the structure. The other one concerns coupling between the interface nonlinearity, radiation and hysteretic damping at the soil-pile interface. The solution algorithm is a back-calculating method in which the Winkler-based closed-form pile head impedance functions are calibrated with results of the continuum models. In other words, an equivalent homogenous bed of viscoelastic Winkler elements (parallel spring and dashpot) is assumed along the pile shaft to represent the stress-induced inhomogeneous soil-pile interaction, caused by the system nonlinearity as well as shear transfer between adjacent soil layers. The proposed hybrid approach involves three different components; each of which handles a specific aspect of the solution totally different from the other two components. Fig. 6.1 illustrates the components of the solution algorithm that utilizes advantages of both the

time-domain direct and frequency-domain substructure solutions of the soil-structure interaction system. As shown, the scheme core relies on algebraic solution of the frequency-domain substructure formulation. In summary, the depicted solution elements and their contribution are described as follows:

- Three-dimensional time-domain continuum modelling of soil-pile-structure interaction system, a powerful means of simulating fairly realistic nonlinear SPSI phenomenon. Using the continuum finite element technique, two crucial aspects of SPSI problem, including the fully coupled nonlinear soil-pile-structure interaction and soil-pile subgrade reaction along the pile length are rigorously captured. With this analysis, displacement and force parameters are provided at any location within the model.
- The substructure method is used as a simplified approach for analysis of the inertial interaction, which allows mathematical solution of the dynamic equation of motion using discrete system properties including mass and stiffness. Moreover, the frequency-domain transform of the substructure formulation facilitates closed-form solution of the system response at a given frequency.
- The third element of the hybrid solution involves analytical derivation of appropriate pile head impedance functions that are inserted to the substructure formulation. The term appropriate refers to the functional form that makes algebraic coupled solution feasible for the system of equation of motions.

The three-step procedure of the substructure analysis, as described in Chapter 2, requires decomposition of the kinematic and inertial interactions, which results in exact solution for

linear interaction only. However, this assumption can be approximately valid for the nonlinear soil-pile interaction in this study for the following reasons:

- Shear strains induced by the inertial interaction are significant near the ground surface and are attenuated rapidly with depth whereas the kinematic interaction controls shear strains at relatively deeper elevations (Gazetas 1984).
- More importantly, using the equivalent-linear frequency-dependent impedance function (viscoelastic) in the frequency-domain solution of the substructure method allows for decomposition of the inertial and kinematic interactions, while the response of structure and foundation applied to the back-calculation of the substructure formulation are obtained from the time-domain continuum model with fully coupled kinematic and inertial interactions.

6.3. Substructure Formulation

6.3.1. Forced head vibration

For a pile shaft shown in Fig. 6.1a, the inelastic pile response under a prescribed force at the pile head is described by the equation of motion as follows:

$$M\Delta\ddot{U}(t) + C\Delta\dot{U}(t) + K\Delta U(t) = \Delta F_{ext}(t) \tag{6.1}$$

where M, C and K denote the mass, damping and stiffness matrix of the system, and U(t) denotes the displacement vector of the system. For a solution in the frequency domain, the above equation can be rewritten as:

$$(-M\omega^2 + C\omega + K)\hat{U}(\omega) = \hat{F}_{ext}(\omega) \tag{6.2}$$

in which $S(\omega) = -M\omega^2 + C\omega + K$ is known as the complex-valued dynamic stiffness or impedance matrix of the system. For analysis of a soil-pile interaction system using the substructure modelling approach, dynamic properties of the near-field soil medium and its interaction with the pile must be determined at the pile head, known as the pile head impedance functions (Fig. 6.1b). Replacing the system impedance with the equivalent pile head impedance in Eq. 6.2, the pile head response can be determined by solving:

$$\begin{bmatrix} S_{uu}(\omega) & S_{u\theta}(\omega) \\ S_{u\theta}(\omega) & S_{\theta\theta}(\omega) \end{bmatrix} \begin{bmatrix} \hat{u}(\omega) \\ \hat{\theta}(\omega) \end{bmatrix} = \begin{bmatrix} \hat{F}(\omega) \\ \hat{M}(\omega) \end{bmatrix} \tag{6.3}$$

where $S_{uu}(\omega), S_{u\theta}(\omega)$ and $S_{\theta\theta}(\omega)$ represent the pile head impedances in the horizontal, cross-coupling and rocking vibration modes.

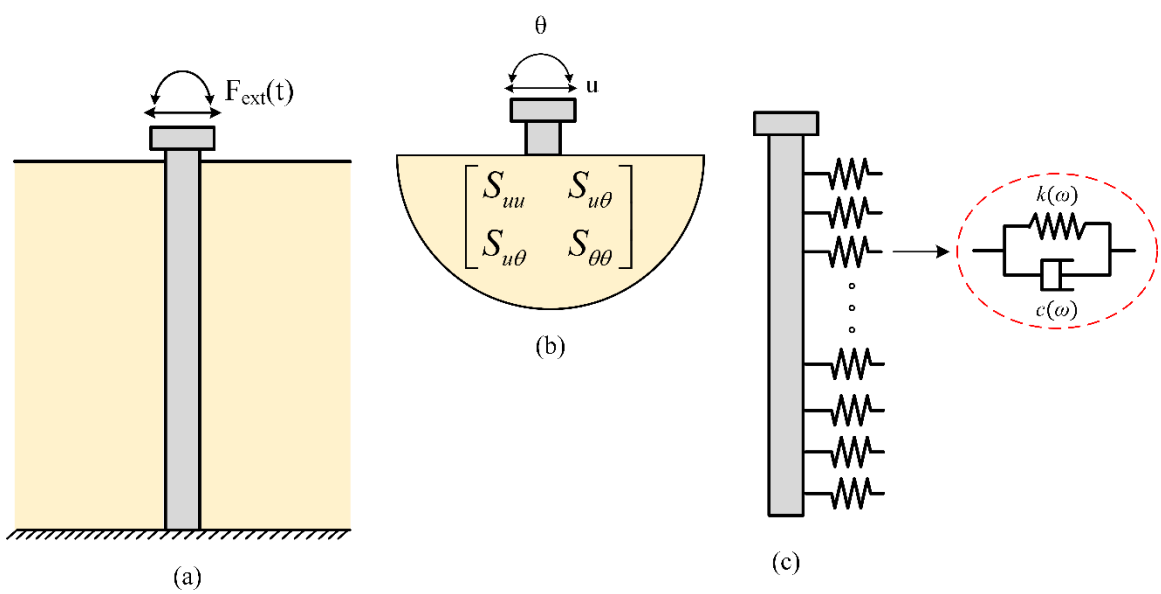

Figure 6.1. Schematic presentation of a) external loads on end-bearing pile head, b) replacing the soil-pile dynamic properties with the impedance matrix, and c) modelling the soil-pile interaction with Winkler viscoelastic medium

6.3.2. Seismic loading

For the substructure analysis of a soil-pile-structure interaction system subjected to propagation of the seismic waves, the three-step procedure of substructure modelling approach should be followed (Kausel et. al 1978). In addition to characterization of the foundation impedances and analysis of the system under structural loads, this involves determination of appropriate foundation input motions, known as kinematic interaction analysis. From this analysis, the horizontal (u_{gk}) and rocking (ϕ_{gk}) components of foundation input motions are determined, which are different from the free field soil vibration due to wave scattering and foundation incompliance at the soil-pile interface.

Fig. 6.2 schematically shows the layout of the substructure model for a single-column bridge system supported by a large-diameter extended RC shaft. As shown, the frequency-dependent parallel springs and dashpots (viscoelastic) are used to represent the dynamic stiffness and damping of the soil-pile interaction system in the horizontal (k_{uu}, c_{uu}), rocking $(k_{\theta\theta}, c_{\theta\theta})$ and cross-coupling $(k_{u\theta}, c_{u\theta})$ modes of vibration. The viscoelastic element is mathematically expressed as:

$$K_{ij} = k_{ij} + i\omega c_{ij} \tag{6.4}$$

where k_{ij} and c_{ij} denote spring and dashpot coefficients, respectively. Since the foundation seismic energy is dissipated through the radiation (c_{rad}) and soil hysteretic damping (c_s) mechanisms, the dashpot coefficient consists of damping values from these two sources:

$$c_{ij} = c_{rad} + c_s \tag{6.5}$$

which can also be expressed in the classic definition form:

$$\zeta_{ij} = \frac{\omega c_{ij}}{2k_{ij}} \tag{6.6}$$

The substructure method is the solution core in the proposed hybrid approach. The goal is to compute equivalent-linear impedance functions by which the substructure analysis of the soil-pile-structure interaction would match the spectral responses given by the rigorous inelastic continuum analysis. This is achieved by conducting a back-analysis of inertial interaction in the substructure model using force and displacement spectral values from the continuum model. This would require identification of the equations of motion governing the substructure system.

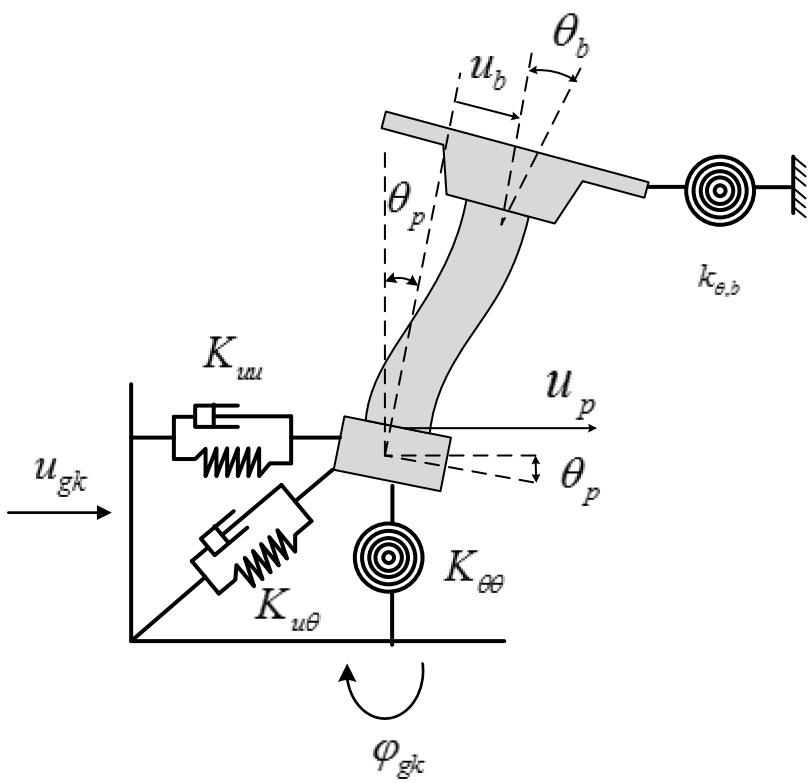

Figure 6.2. Schematic presentation for substructure modelling of the bridge superstructure under earthquake loading

6.3.2.1. Equations of motion

The equations of motion for a lumped system of the soil-pile-structure interaction (Fig. 6.2) subjected to the foundation input motions (FIM) can be written in time domain:

$$m_b(\ddot{u}_b + \ddot{u}_p + H\ddot{\theta}_p) + c_s\dot{u}_b + k_s u_b = -m_b(\ddot{u}_{gk} + H\ddot{\theta}_{gk}) \tag{6.6}$$

$$m_{p,uu}\ddot{u}_p + m_{p,u\theta}\ddot{\theta}_p + c_{uu}\dot{u}_p + c_{u\theta}\dot{\theta}_p + k_{uu}u_p + k_{u\theta}\theta_p - c_s\dot{u}_b - k_s u_b = -m_{p,uu}\ddot{u}_{gk} - m_{p,u\theta}\ddot{\theta}_{gk} \tag{6.7}$$

$$m_b H(\ddot{u}_b + \ddot{u}_p + H\ddot{\theta}_p) + I_b(\ddot{\theta}_p + \ddot{\theta}_b) + m_{p,\theta\theta}\ddot{\theta}_p + m_{p,u\theta}\ddot{u}_p + c_{\theta u}\dot{u}_p + c_{\theta\theta}\dot{\theta}_p + k_{\theta u}u_p + k_{\theta\theta}\theta_p$$
$$-c_{\theta,b}\dot{\theta}_b - k_{\theta,b}\theta_b = -(m_{p,\theta\theta} + I_b)\ddot{\theta}_{gk} - m_b H(\ddot{u}_{gk} + H\ddot{\theta}_{gk}) - m_{p,u\theta}\ddot{u}_{gk} \tag{6.8}$$

where Eq. 6.6 represents the translational force equilibrium of the bridge superstructure, Eq. 6.7 represents the translational force equilibrium of the foundation and Eq. 6.8 represents the moment equilibrium of the soil-foundation-structure system. In Eqs. 6.7 and 6.8, m_b, k_s, c_s, u_b, I_b and θ_b denote the mass, stiffness, dashpot coefficient, relative displacement, mass moment of inertia and relative rotation of the superstructure, respectively, and m_p, $u_p$and $\theta_p$denote the mass, relative displacement and rotation of the foundation, respectively. Rearranging Eq. 6.7 and 6.8 and substituting the stiffness and damping forces $(k_s u_b + c_s\dot{u}_b)$ in Eq. 6.7 with the equivalent terms from Eq. 6.6 yield to a system of dynamic force-deformation equations for the foundation:

$$\begin{cases} m_{p,uu}\ddot{u}_p + m_{p,u\theta}\ddot{\theta}_p + +c_{uu}\dot{u}_p + c_{u\theta}\dot{\theta}_p + k_{uu}u_p + k_{u\theta}\theta_p = V_p & (6.9) \\ m_{p,\theta\theta}\ddot{\theta}_p + m_{p,u\theta}\ddot{u}_p + c_{\theta u}\dot{u}_p + c_{\theta\theta}\dot{\theta}_p + k_{\theta u}u_p + k_{\theta\theta}\theta_p = M_p & (6.10) \end{cases}$$

Ignoring the inertial loads due to foundation mass, the inertial shear and moment forces transmitted to the top of the foundation from the superstructure are defined as:

$$V_p = -m_b(\ddot{u}_{gk} + H\ddot{\theta}_{gk}) - m_b(\ddot{u}_b + \ddot{u}_p + H\ddot{\theta}_p) \tag{6.11}$$

$$M_p = -I_b\ddot{\theta}_{gk} - m_b H(\ddot{u}_{gk} + H\ddot{\theta}_{gk}) - m_b H(\ddot{u}_b + \ddot{u}_p + H\ddot{\theta}_p) - I_b(\ddot{\theta}_p + \ddot{\theta}_b) + c_{\theta,b}\dot{\theta}_b + k_{\theta,b}\theta_b \tag{6.12}$$

Eqs. 6.9 and 6.10 are transformed to the frequency domain in order to solve it conveniently through algebraic operation and also capture the frequency-dependent nature of the foundation impedance. In this case, a complex-valued algebraic system of equations must be solved for a given frequency (ω). The consequent frequency-domain transform of Eq. 6.9 and 6.10 takes a matrix form as:

$$\left\{\begin{bmatrix} k_{uu} & k_{u\theta} \\ k_{u\theta} & k_{\theta\theta} \end{bmatrix} + i\omega \begin{bmatrix} c_{uu} & c_{u\theta} \\ c_{u\theta} & c_{\theta\theta} \end{bmatrix} - \omega^2 \begin{bmatrix} m_{p,uu} & m_{p,u\theta} \\ m_{p,u\theta} & m_{p,\theta\theta} \end{bmatrix}\right\} \begin{Bmatrix} \hat{u}_p \\ \hat{\theta}_p \end{Bmatrix} = \begin{Bmatrix} \hat{V}_p \\ \hat{M}_p \end{Bmatrix} \tag{6.13}$$

where "^ " denotes the Fourier transform of the variables, given by:

$$\hat{V}_p = \int_{-\infty}^{+\infty} V_p(t) e^{-i\omega t} dt. \tag{6.14}$$

The complex-valued matrix on the left side of Eq. 6.13 including inertial, stiffness and damping action of the foundation represents the foundation impedance matrix. Such a matrix in the case of a pile foundation can be replaced by the pile head impedance functions which yield to:

$$\begin{bmatrix} S_{uu}(\omega) & S_{u\theta}(\omega) \\ S_{u\theta}(\omega) & S_{\theta\theta}(\omega) \end{bmatrix} \begin{Bmatrix} \hat{u}_p \\ \hat{\theta}_p \end{Bmatrix} = \begin{Bmatrix} \hat{V}_p \\ \hat{M}_p \end{Bmatrix} \tag{6.15}$$

Details of derivation of the impedance functions and approximation of their appropriate functional form for use in algebraic solution of Eq. 6.15 are discussed in the following section.

6.4. Derivation of pile head impedance functions

6.4.1. Closed-form elastic solution

Elastic solution of lateral soil-pile interaction under pile head moments and forces can be used to derive the pile head stiffness for small-strain (elastic) and equivalent-linear representation of nonlinear interaction problems. The simplified beam-on-Winkler foundation concept is commonly used to model dynamic properties of the soil-pile interaction. The Winkler method refers to response of a beam supported by a bed of independent springs with elastic stiffness modulus known as "modulus of subgrade reaction". In Winkler method, soil pressure (subgrade reaction) exerted on the pile at a given depth is proportional to relative soil-pile displacement through the modulus of subgrade reaction. For a vertical pile foundation assumed as an Euler-Bernoulli beam, embedded in a homogeneous viscoelastic Winkler medium (Fig. 6.1c) and subjected to vertically propagating shear waves as well as the pile head excitation, the governing equilibrium differential equation is as follows:

$$E_p I_p \frac{\partial^4 u}{\partial z^4} + m_p \frac{\partial^2 u}{\partial t^2} + c\left(\frac{\partial u}{\partial t} - \frac{\partial u_{ff}}{\partial t}\right) + k\left(u - u_{ff}\right) = 0 \tag{6.16}$$

where $E_p I_p$is flexural stiffness, m_p is pile mass per length, and $u = u(z,t)$ is horizontal displacement of the pile. $k = k(z,\omega)$and$c = c(z,\omega)$denote frequency-dependent modulus of subgrade reaction and dashpot coefficients. $u_{ff} = u_{ff}(z,t)$ denotes the amplitude of the

free field motion at depth z, which in the viscoelastic soil medium is given by (Kramer 1996):

$$u_{ff} = u_g \cos(\omega z / v_s^*) e^{i\omega t} \tag{6.17}$$

where u_g denotes the displacement amplitude of the free field motion at ground surface, and v_s^* represents the complex shear wave velocity of the viscoelastic soil medium. The partial differential equation of Eq. 6.16 can be converted to an ordinary differential equation by assuming a harmonic pile and free field soil motions as follows:

$$u(z,t) = u(z) e^{i\omega t} \tag{6.18}$$

Substituting Eqs. 6.18 and 6.17 into 6.16 yields to a simple ordinary differential equation:

$$\frac{\partial^4 u(z)}{\partial z^4} + \frac{(k + i\omega c - m\omega^2)}{E_p I_p} u(z) = \frac{(k + i\omega c) u_g \cos(qz)}{E_p I_p} \tag{6.19}$$

where $K = k + i\omega c$ is the complex-valued impedance function of the Winkler medium, and $q = \omega / v_s^*$ denotes the wavenumber of the free field soil medium. Solving the above equation for general and particular solutions yields to:

$$u(z) = e^{\lambda z}(A_1 \cos(\lambda z) + A_2 \sin(\lambda z)) + e^{-\lambda z}(A_3 \cos(\lambda z) + A_4 \sin(\lambda z)) + \frac{K u_{ff}}{E_p I_p (q^4 + 4\lambda^4)} \tag{6.20}$$

where A_1 to A_4 are solution constants and a characteristic parameter λ is defined as below:

$$\lambda = \sqrt[4]{\frac{k + i\omega c - m\omega^2}{4 E_p I_p}} \tag{6.21}$$

which is known as Winkler wavenumber that controls propagation of the pile head excitation along the pile length, and its inverse from $(1/\lambda)$ which has a displacement unit called characteristic wavelength. The elastic soil-pile interaction stiffness (k) is related to

the soil modulus of elasticity (E_s) through a dimensionless parameter known as Winkler coefficient (δ):

$$k = \delta . E_s \tag{6.22}$$

Early works by Blaney et al. (1976) and Roesset (1980) proposed constant value of 1.2 for δ regardless of pile head condition and stiffness parameters, while later studies have shown that the relative soil-pile stiffness (E_p/E_s), homogeneity of the soil medium and pile head boundary condition (free or fixed) influence value of δ (Gazetas and Dobry 1984, Syngros 2004).

Eq. 6.20 clearly shows that the frequency-domain solution of the soil-pile interaction allows for decomposition of the inertial and kinematic interaction effects. Thus, superposing the pile head displacements from the kinematic and inertial interactions is valid in the equivalent-linear representation of inelastic soil-pile interaction in the frequency-domain. As a result, the pile head impedance functions are derived directly for the pile head loadings (no ground motion). The static pile head loading condition ($\omega = 0$) is considered in order to derive a functional form of the pile head impedances. Thus, for a 2D substructure SSI analysis of a pile foundation with the impedance matrix depicted in Eq. 6.15 and including two independent stiffness terms ($k_{uu}, k_{\theta\theta}$), two different boundary values of unit displacement and rotation are applied at the pile head in order to derive the impedance function matrix. The derivation procedure is described in detail in Appendix B. The resulting pile head impedance matrices for a free head pile with hinged-tip is:

$$S_p = \begin{bmatrix} 4E_pI_p\lambda^3 \dfrac{\cos(2\lambda L)+\cosh(2\lambda L)}{-\sin(2\lambda L)+\sinh(2\lambda L)} & 2E_pI_p\lambda^2 \dfrac{-\sin(2\lambda L)-\sinh(2\lambda L)}{\sin(2\lambda L)-\sinh(2\lambda L)} \\ 2E_pI_p\lambda^2 \dfrac{-\sin(2\lambda L)-\sinh(2\lambda L)}{\sin(2\lambda L)-\sinh(2\lambda L)} & 2E_pI_p\lambda \dfrac{\cos(2\lambda L)-\cosh(2\lambda L)}{\sin(2\lambda L)-\sinh(2\lambda L)} \end{bmatrix} \quad (6.23)$$

and for a fixed-tip pile condition:

$$S_p = \begin{bmatrix} 4E_pI_p\lambda^3 \dfrac{\sin(2\lambda L)+\sinh(2\lambda L)}{-2+\cos(2\lambda L)+\cosh(2\lambda L)} & 2E_pI_p\lambda^2 \dfrac{-\cos(2\lambda L)+\cosh(2\lambda L)}{-2+\cos(2\lambda L)+\cosh(2\lambda L)} \\ 2E_pI_p\lambda^2 \dfrac{-\cos(2\lambda L)+\cosh(2\lambda L)}{-2+\cos(2\lambda L)+\cosh(2\lambda L)} & 2E_pI_p\lambda \dfrac{-\sin(2\lambda L)+\sinh(2\lambda L)}{-2+\cos(2\lambda L)+\cosh(2\lambda L)} \end{bmatrix} \quad (6.24)$$

These impedance matrices were first introduced by Mylonkis (1995) for three types of pile tip boundary condition including stress-free floating pile in addition to those mentioned herein. The derivations in Appendix A show that the above functional forms are identical for the fixed head and free head piles. This implies that the functional form of pile head impedances is controlled by the boundary conditions at the pile tip. The fractional part of the matrix elements in Eqs. 6.23 and 6.24 converges to 1 as the dimensionless characteristic parameter (λL) increases. It means that for a relatively long pile or a pile embedded in stiff soil, pile impedances may be independent of pile length and yield to the following simplified matrix (Pender 1993):

$$S_p = \begin{bmatrix} 4E_pI_p\lambda^3 & 2E_pI_p\lambda^2 \\ 2E_pI_p\lambda^2 & 2E_pI_p\lambda \end{bmatrix} \quad (6.25)$$

The application of these impedance formulas in Eqs. 6.23 and 6.24 is limited to homogenous linear elastic soil continuum, and the closed-form formulas for multi-layer soil domain (inhomogeneous) which is the case in reality and takes a complicated and

impractical form (Mylonakis 1995). Moreover, inelastic soil-pile interaction during strong ground shaking and interface nonlinearity such as soil-pile gapping under large inertial loads may result in dramatic reduction of the lateral pile stiffness and completely inhomogeneous distribution of the wavenumber. Despite the above mentioned limitations, the presented impedance functions can be useful if an appropriate average Winkler wavenumber $(\bar{\lambda})$ is estimated, which is intended in this study. It should be noted that the "average" term herein refers to the equivalent-homogenous wavenumber estimated for a pile in an inhomogeneous soil medium with inelastic soil-pile interaction, and is different from arithmetic mean wavenumber (μ) computed over the active pile length.

6.4.2. Polynomial approximation of impedance functions

The pile head impedance function is the key element to compute the average wavenumber $\bar{\lambda}$ through the back-calculation solution of the substructure formulation if they are expressed in an appropriate form for algebraic computation. As shown in Fig. 6.2, using simplified impedance functions in Eq. 6.24 is valid only for the values of $\lambda L > 2.5$ for fixed-tip piles and $\lambda L > 1.5$ for hinged-tip piles. This validity range of λL corresponds to long flexible piles in relatively stiff soils, in particular for the fixed-tip boundary condition, while there might be different combinations of soil-pile relative stiffness and pile physical characteristics (length, boundary conditions) that require using the general hyperbolic form of the impedance functions (i.e. Eqs. 6.23, 6.24). One practical example can be a short large diameter RC shaft with the tip socketed into a firm layer or bedrock. Further, the average wavenumber $\bar{\lambda}$ can be reduced by the soil-pile interface nonlinearity (gap) and soil inelasticity during strong earthquake shaking. This implies that due to inelastic soil-pile-

structure interaction, the active pile length and the consequent lateral pile performance would be different from the presumptive ones based on elastic parameters. Hence, it seems essential to approximate an appropriate functional form of the impedance functions to cover the entire range of λL values.

In this study, the hyperbolic impedance functions are approximated by polynomial terms using infinite power series. In mathematics, Taylor series is used to represent a function $f(x)$ as an infinite sum of the polynomial terms with coefficients given by values of the function derivatives at a single point:

$$f(x) = \sum_{0}^{\infty} \frac{f^{(n)}(a)}{n!}(x-a)^n \tag{6.26}$$

where $f^{(n)}(a)$ is the *n*th derivative of the function at point *a*, and $n!$ denotes the factorial of *n*. Maclaurin series which is the Taylor series centered at zero ($a = 0$) is used herein to represent hyperbolic functions. Followings are the Maclaurin expansion of the functions involved in the impedance functions, which are valid for all the real and complex values of x:

$$\begin{aligned}
\sin x &= \sum_{n=0}^{\infty} \frac{(-1)^n}{(2n+1)!} x^{2n+1} \\
\cos x &= \sum_{n=0}^{\infty} \frac{(-1)^n}{(2n)!} x^{2n} \\
\sinh x &= \sum_{n=0}^{\infty} \frac{x^{2n+1}}{(2n+1)!} \\
\cosh x &= \sum_{n=0}^{\infty} \frac{x^{2n}}{(2n)!}
\end{aligned} \tag{6.27}$$

The fractional hyperbolic components of the horizontal, rocking and cross-coupling impedance functions presented in Eqs. 6.23 and 6.24 are approximated by two sequences

of Maclaurin expansion. In both steps, the functions are replaced by the finite degrees (n) of the Maclaurin polynomial, sufficient to minimize the approximation error and low enough to give the function a simple form that is appealing for practice. Trying different degrees, it was concluded that the sixth degree Maclaurin polynomial for each of the hyperbolic functions would optimize the approximation, and it is needless to include higher degree terms. This is attributed to the fact that as the expansion degree increases the factorial term in the denominator grows at faster rate compared to the power term in the numerator, leading the fraction to zero. In this study, the pile head impedance matrix for both hinged and fixed-tip piles is approximated. Since the approximation procedure for different modes (i.e., horizontal, rocking, etc.) is similar, details of approximation procedure for swaying mode of fixed-tip pile is described herein as a sample calculation. Derivation starts with expanding each hyperbolic function with its corresponding Maclaurin series of Eq. (6.26):

$$
\begin{aligned}
S_{uu} &= 4E_pI_p\lambda^3 \frac{\sin(2\lambda L)+\sinh(2\lambda L)}{-2+\cos(2\lambda L)+\cosh(2\lambda L)} \\
&= 4E_pI_p\lambda^3 \frac{4\lambda L+\dfrac{2(2\lambda L)^5}{5!}+\dfrac{2(2\lambda L)^9}{9!}+\dfrac{2(2\lambda L)^{13}}{13!}}{\dfrac{2(2\lambda L)^4}{4!}+\dfrac{2(2\lambda L)^8}{8!}+\dfrac{2(2\lambda L)^{12}}{12!}}
\end{aligned}
\tag{6.28}
$$

Factoring out $4\lambda L$ and 2 in the numerator and denominator, respectively, the impedance is written as:

$$
S_{uu} \approx 8E_pI_p\lambda^4 \frac{1+\dfrac{(2\lambda L)^4}{5!}+\dfrac{(2\lambda L)^8}{9!}+\dfrac{(2\lambda L)^{12}}{13!}}{\dfrac{(2\lambda L)^4}{4!}+\dfrac{(2\lambda L)^8}{8!}+\dfrac{(2\lambda L)^{12}}{12!}}
\tag{6.29}
$$

Factoring out $(2\lambda L)^4/4!$ in the denominator and the entire numerator expression turns the impedance to the product of two major functions as follows:

$$S_{uu} \approx 8E_p I_p \lambda^4 L \frac{1+\frac{(2\lambda L)^4}{5!}+\frac{(2\lambda L)^8}{9!}+\frac{(2\lambda L)^{12}}{13!}}{\frac{(2\lambda L)^4}{4!}} \overbrace{\left(\frac{1}{\underbrace{1+\frac{4!(2\lambda L)^4}{8!}+\frac{4!(2\lambda L)^8}{12!}}_{B(\lambda)}}\right)}^{A(\lambda)} \tag{6.30}$$

where $A(\lambda)$ can be approximated using the following Maclaurin series if $|B(\lambda)|<1$:

$$\frac{1}{1-x}=\sum_{n=0}^{\infty} x^n \quad \text{for} \quad |x|<1 \tag{6.31}$$

In Eq. 6.30, while $\lambda L \le 3$, $|B(\lambda)|<1$, hence, $A(\lambda)$ is approximated by means of the second degree Maclaurin expansion:

$$A(\lambda) \approx \frac{1}{1+\frac{4!(2\lambda L)^4}{8!}+\frac{4!(2\lambda L)^8}{12!}} = 1-\frac{4!(2\lambda L)^4}{8!}-\frac{4!(2\lambda L)^8}{12!}+\frac{(4!)^2\,(2\lambda L)^8}{(8!)^2} \tag{6.32}$$

where polynomial order is limited to eight in order to retain simplicity of the formula. Substituting Eq. 6.32 into Eq. 6.30 followed by the simplification of the formula yields to:

$$S_{uu} \approx \overline{S}_{uu} = \frac{12E_p I_p}{L^3}\left(1+\frac{(2\lambda L)^4}{5!}+\frac{(2\lambda L)^8}{9!}\right)\left(1-\frac{4!(2\lambda L)^4}{8!}-\frac{4!(2\lambda L)^8}{12!}+\frac{(4!)^2\,(2\lambda L)^8}{(8!)^2}\right) \tag{6.33}$$

Further simplification and rearrangement of Eq. 6.33 yields to the final form of the approximated impedance function for the horizontal mode:

$$S_{uu} \approx \overline{S}_{uu} = \frac{12E_p I_p}{L^3}\left(1+1.24E^{-1}(\lambda L)^4-4.9E^{-4}(\lambda L)^8\right) \tag{6.34}$$

The described approximation procedure is repeated for the rotational and cross-coupling impedances of the fixed-tip pile and impedance matrix of the hinged-tip pile as well. The resulting approximated impedance matrix for the fixed-tip pile is stated as:

$$\overline{S}_p = \begin{bmatrix} \frac{12E_pI_p}{L^3}\overline{\beta}_{uu} & \frac{6E_pI_p}{L^2}\overline{\beta}_{u\theta} \\ \frac{6E_pI_p}{L^2}\overline{\beta}_{u\theta} & \frac{4E_pI_p}{L}\overline{\beta}_{\theta\theta} \end{bmatrix} \tag{6.35}$$

where,

$$\begin{aligned} \overline{\beta}_{uu} &= (1+1.24\mathrm{E}^{-1}(\lambda L)^4 - 4.9\mathrm{E}^{-4}(\lambda L)^8) \\ \overline{\beta}_{u\theta} &= (1+3.5\mathrm{E}^{-2}(\lambda L)^4 - 2.1\mathrm{E}^{-4}(\lambda L)^8) \\ \overline{\beta}_{\theta\theta} &= (1+9.5\mathrm{E}^{-3}(\lambda L)^4 - 8.9\mathrm{E}^{-5}(\lambda L)^8) \end{aligned} \tag{6.36}$$

and for the hinged-tip pile, the impedance matrix is stated as:

$$\overline{S}_p = \begin{bmatrix} \frac{3E_pI_p}{L^3}\overline{\beta}_{uu} & \frac{3E_pI_p}{L^2}\overline{\beta}_{u\theta} \\ \frac{3E_pI_p}{L^2}\overline{\beta}_{u\theta} & \frac{3E_pI_p}{L}\overline{\beta}_{\theta\theta} \end{bmatrix} \tag{6.37}$$

where,

$$\begin{aligned} \overline{\beta}_{uu} &= (1+6.48\mathrm{E}^{-1}(\lambda L)^4 - 6.0\mathrm{E}^{-3}(\lambda L)^8) \\ \overline{\beta}_{u\theta} &= (1+1.14\mathrm{E}^{-1}(\lambda L)^4 - 1.51\mathrm{E}^{-3}(\lambda L)^8) \\ \overline{\beta}_{\theta\theta} &= (1+2.54\mathrm{E}^{-2}(\lambda L)^4 - 3.8\mathrm{E}^{-4}(\lambda L)^8) \end{aligned} \tag{6.38}$$

6.4.3. Approximation error

Fig. 6.3 compares the approximated polynomial static pile stiffness $(\omega = 0)$ with the exact hyperbolic ones for the fixed and hinged-tip piles under the swaying, rocking and cross-coupling modes. The stiffness components are illustrated as a function of the pile mechanical slenderness λL and normalized by the asymptotic stiffness values. For all stiffness modes, a fairly perfect match is observed schematically between the approximated and the exact functions for both types of the pile tip conditions. However, quantification of approximation error is needed to verify reliability of the approximated impedance functions and identify their slenderness range of validity. The approximation error is determined using the following expression:

$$e(\%) = \frac{\overline{S}_{ij}(\lambda L) - S_{ij}(\lambda L)}{S_{ij}(\lambda L)} \tag{6.39}$$

where e denotes the approximation error in percent, $\overline{S}_{ij}$ and S_{ij} correspond to the approximated and exact impedance values along the mode i and j, respectively. Fig. 6a-c illustrates variation of the absolute value of the approximation error with increasing λL for all three modes. Considering five percent as the upper limit of the acceptable approximation error margin, the error curves cross the limit line at λL values slightly larger than that corresponding to the active pile length, beyond which the pile head stiffness asymptotes to the ultimate stiffness independent of the pile length. Thus, it is concluded that the presented polynomial impedance functions can accurately approximate the pile head impedances within the λL range with the upper bound value corresponding to the

active pile length. This upper bound value is about $\lambda L = 2.5$ for the fixed-tip pile and $\lambda L = 2.1$ for the hinged-tip pile.

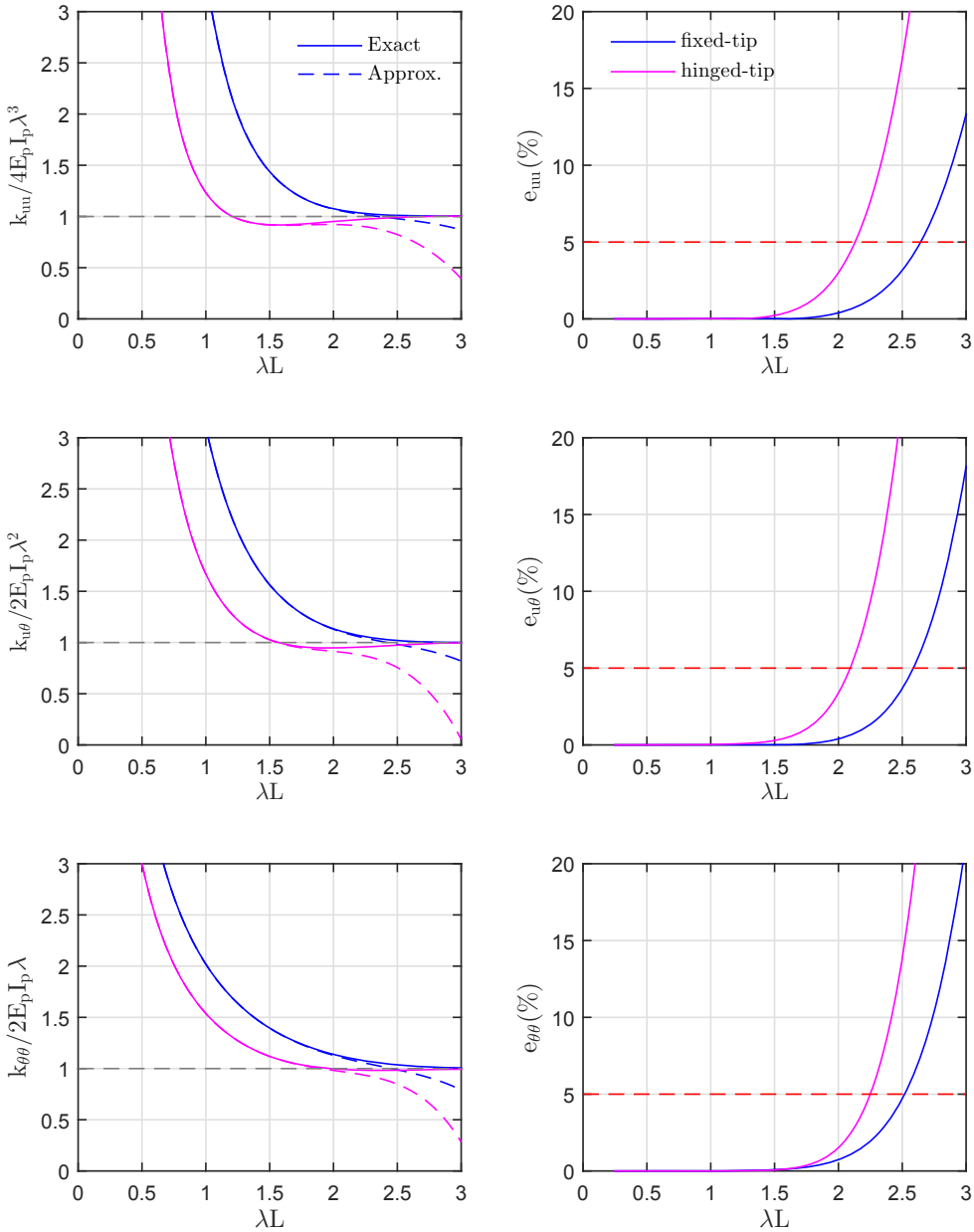

Figure 6.3. Comparison between the approximated and exact variations of the pile head impedance functions and variations of the approximation error with λL values

6.5. Computation of the Equivalent-linear Average Impedance Function from Continuum Analysis

This section presents a procedure for computing the equivalent-linear average impedance function from results of the 3D inelastic continuum analysis of dynamic soil-pile-structure interaction for the extended RC pile shaft of the bridge. The idea is to first derive the equivalent-linear average wavenumber ($\bar{\lambda}$) from algebraic solution of the complex-valued force-deformation matrix in Eqs. 6.3 and 6.15, and compute subsequently the corresponding pile head impedance functions for the three vibration modes. It should be noted that in reality, the Winkler coefficient (δ) value is not constant along the pile length even for the piles in homogeneous linear elastic soil medium (Syngros 2004). This can be attributed to the coupling between adjacent soil layers that allows for the shear transfer to deeper soil layers. Varying δ values with depth is in contrast with the common assumption of a bed of uncoupled independent springs supporting the pile. Thus, approximating the realistic pile head impedances with inhomogeneous distribution of δ values by the closed-form impedances as a function of equivalent homogeneous wavenumber ($\bar{\lambda}$) is associated with some error that will be examined later in Chapter 7 of this thesis. The derivation procedure begins with recalling Eq. 6.15 here as:

$$\begin{bmatrix} S_{uu}(\omega) & S_{u\theta}(\omega) \\ S_{u\theta}(\omega) & S_{\theta\theta}(\omega) \end{bmatrix} \begin{Bmatrix} \hat{u}_p \\ \hat{\theta}_p \end{Bmatrix} = \begin{Bmatrix} \hat{V}_p \\ \hat{M}_p \end{Bmatrix}$$

where $\hat{V}_p$ and $\hat{M}_p$ denote the Fourier transform of the base shear and moment recorded at the base of the pier column (pile head) in the finite element models, respectively. $\hat{u}_p = \hat{u}_{pt} - \hat{u}_{gk}$ and $\hat{\theta}_p = \hat{\theta}_{pt} - \hat{\phi}_{gk}$ denote the Fourier transform of relative horizontal and

rotational pile head displacements, respectively. The relative displacements are determined as difference between the recorded spectral displacement values $(\hat{\theta}_{pt})$ in the FE analysis of the entire soil-pile-structure system and those from the kinematic only analysis. It should be noted that FE-based $\hat{V}_p$ and $\hat{M}_p$ values neglect the horizontal and rotational inertia of the foundation motion due to the input kinematic accelerations, compared to their parametric definition in the substructure notation (Eqs. 6.7 and 6.8). Neglecting these values does not significantly affect the derivation results as these forces are negligible compared to huge structural inertial forces. Depending on the pile tip boundary condition and the λL value, the elements of the impedance matrix are substituted by the corresponding polynomial functions as presented in Section 6.4.2. The algebraic derivation procedure is described in the following for the case of a fixed-tip relatively short pile for which the approximating polynomial function should be used. This is related to the assumption that in such a case, upon pile-soil gap creation and degradation of soil stiffness under strong inertial structural loads, the $\bar{\lambda}L$ value is very likely to fall below $\lambda L = 2.5$, while in the case of a hinged-tip long pile or short fixed-tip pile under weak earthquake motion with larger $\bar{\lambda}L$ values, the asymptotic impedances (i.e. $S_{uu} = 4EI\lambda^3$) can be used.

Assuming $\bar{\lambda}L < 2.5$ for a fixed-tip pile, the polynomial impedance matrix of Eq. 6.35 is used in Eq. 6.15 to derive $\bar{\lambda}$ as follows:

$$\begin{bmatrix} \frac{12E_pI_p}{L^3}\overline{\beta}_{uu} & -\frac{6E_pI_p}{L^2}\overline{\beta}_{u\theta} \\ -\frac{6E_pI_p}{L^2}\overline{\beta}_{u\theta} & \frac{4E_pI_p}{L}\overline{\beta}_{\theta\theta} \end{bmatrix} \begin{Bmatrix} \hat{u}_p - \hat{u}_{gk} \\ \hat{\theta}_p - \hat{\phi}_{gk} \end{Bmatrix} = \begin{Bmatrix} \hat{V}_p \\ \hat{M}_p \end{Bmatrix} \tag{6.40}$$

where $\bar{\lambda}$ is the only unknown variable to be determined by solving the above system of complex equations. From Eq. 6.38, it is evident that $\bar{\lambda}$ as the only variable can be

determined by solving each of the two equations in Eq. 6.40. But, the obtained value from one equation (i.e., force equilibrium) does not satisfy the other one (i.e., moment equilibrium), thus, these two equations must be solved simultaneously in order to achieve an optimum $\bar{\lambda}$ value which can satisfy both equations with an acceptable error margin. Therefore, performing some basic algebra, Eq. 6.40 is reduced to a polynomial complex equation:

$$(\bar{\lambda}L)^8 + A(\omega)(\bar{\lambda}L)^4 + B(\omega) = 0 \tag{6.41}$$

which can simply turns to a quadratic equation by means of a variable change of $t = (\bar{\lambda}L)^4$ as:

$$t^2 + A(\omega)t + B(\omega) = 0 \tag{6.42}$$

Using the characteristic equation of the quadratic polynomial, the four complex roots of the above equation can be determined as follows:

$$\begin{aligned} t_{1,2} &= \frac{-A(\omega) \pm \sqrt{|\Delta|}e^{i\vartheta/2}}{2} \\ t_{3,4} &= \frac{-A(\omega) \pm \sqrt{|\Delta|}e^{i(\vartheta+2\pi)/2}}{2} \end{aligned} \tag{6.43}$$

where the characteristic equation (Δ) and the corresponding phase angle (ϑ) are define as:

$$\begin{aligned} \Delta &= A(\omega)^2 - 4B(\omega) \\ \vartheta &= \text{Arctan}\left(\frac{\text{Im}(\Delta)}{\text{Re}(\Delta)}\right) \end{aligned} \tag{6.44}$$

Separating the real and imaginary parts and considering that $e^{i\vartheta/2} = -e^{i(\vartheta+2\pi)/2}$, the four roots of Eq. 40 are reduced to the following two roots:

$$\mathrm{Re}(t_{1,2}) = \frac{-\mathrm{Re}(A(\omega)) \pm \sqrt{|\Delta|}\cos(\vartheta/2)}{2}$$
$$\mathrm{Im}(t_{1,2}) = \frac{-\mathrm{Im}(A(\omega)) \pm \sqrt{|\Delta|}\sin(\vartheta/2)}{2} \tag{6.45}$$

Computing $t = (\lambda L)^4$ and given that $\lambda^4 = (k - m\omega^2 + i\omega c)/4E_pI_p$ in Eq. 6.21, the equivalent-linear average subgrade impedance function is determined over the given frequency range. Subsequently, the corresponding pile head impedances are computed directly by inserting the obtained "t" value in Eqs. 6.34 and 6.35.

For the case of a long flexible pile, the $\bar{\lambda}L$ value is mostly larger than 2.5 and, hence, the asymptotic impedance function values in Eq. 6.24 are used to back-calculate $\bar{\lambda}$ value from Eq. 6.15 as follows:

$$\begin{bmatrix} 4E_pI_p\bar{\lambda}^3 & -2E_pI_p\bar{\lambda}^2 \\ -2E_pI_p\bar{\lambda}^2 & 2E_pI_p\bar{\lambda} \end{bmatrix} \begin{Bmatrix} \hat{u}_p - \hat{u}_{gk} \\ \hat{\theta}_p - \hat{\phi}_{gk} \end{Bmatrix} = \begin{Bmatrix} \hat{V}_p \\ \hat{M}_p \end{Bmatrix} \tag{6.46}$$

Algebraic simplification and rearrangement of the above system of two equations yield to the following third order polynomial equation:

$$\bar{\lambda}^3 + A(\omega)\bar{\lambda} + B(\omega) = 0 \tag{6.47}$$

where

$$A(\omega) = -\frac{(\hat{\theta}_p - \hat{\phi}_{gk})^2}{2(\hat{u}_p - \hat{u}_{gk})^2} \tag{6.48}$$

$$B(\omega) = \frac{\hat{M}_p(\hat{\theta}_p - \hat{\phi}_{gk}) - \hat{V}_p(\hat{u}_p - \hat{u}_{gk})}{4(E_pI_p)(\hat{u}_p - \hat{u}_{gk})^2} \tag{6.49}$$

The obtained complex-valued equivalent-linear wavenumber is described with the following parameters:

$$\bar{\lambda} = \bar{\lambda}_1 + i\bar{\lambda}_2 \tag{6.50}$$

$$\phi_\lambda = \text{Arctan}(\bar{\lambda}_2 / \bar{\lambda}_1) \tag{6.51}$$

$$\left|\bar{\lambda}\right| = \sqrt{\bar{\lambda}_1^{\,2} + \bar{\lambda}_2^{\,2}} \tag{6.52}$$

where ϕ_λ and $|\bar{\lambda}|$ denote the phase angle and modulus of the wavenumber, respectively. Using these parameters, the swaying, rocking and cross-coupling impedance functions are computed as follows:

$$S_{uu} = 4E_p I_p \left|\bar{\lambda}\right|^3 (\cos 3\phi_\lambda + i \sin 3\phi_\lambda) \tag{6.53}$$

$$S_{u\theta} = 2E_p I_p \left|\bar{\lambda}\right|^2 (\cos 2\phi_\lambda + i \sin 2\phi_\lambda) \tag{6.54}$$

$$S_{\theta\theta} = 2E_p I_p \left|\bar{\lambda}\right| (\cos \phi_\lambda + i \sin \phi_\lambda) \tag{6.55}$$

where real and imaginary parts represent the pile head dynamic stiffness and damping coefficient (ωc_{ij}), respectively.

Chapter 7 : Computation of pile head impedance functions under different loading modes

7.1. Introduction

This chapter presents application of the proposed hybrid method described in Chapter 6 in computing the pile head impedance functions for two different loading modes. In fact, the scope of this chapter is two folds; first is verification of the proposed back-calculating method for derivation of the equivalent-linear average modulus of subgrade reaction by comparing it with the modulus values proposed by previous studies. Derivation of the modulus and its corresponding impedance functions are then extended to inelastic soil-pile interaction regime in heterogeneous soil deposit under static and dynamic loading conditions. In this step, the pile loading pattern is limited to controlled excitations at the pile head, representing the inertial forces transmitted from the superstructure. The second objective is to characterize variation of the impedance functions for soil-pile-structure systems in inhomogeneous soil deposits under earthquake loading scenarios, in which the pile is subjected to seismic lateral soil displacement (kinematic interaction) in addition to

the inertial loads exerted to pile head. Further, the inelastic modulus of subgrade reaction is expected to degrade as the shear waves propagate through the soil deposit.

7.2. Computation of Impedance Functions: Pile Head Loading

Analysis of the soil-pile interaction for various infrastructure systems such as bridges and wind turbines is primarily carried out for the cyclic inertial loads transmitted from the superstructure. The spectra of these forces contain broad range of amplitudes and frequency contents, which must be considered in evaluation of the impedance functions for accurate quantification of inelastic soil-structure interaction. Because, due to highly inelastic soil behaviour, even a low level of displacement amplitude on the pile head can cause deflection in the pile's adjacent soil and, hence, alter the interaction stiffness. Moreover, the frequency content of the imposed force affects the interaction impedances through their frequency-dependent nature, in particular that of damping part. The process of computing the impedance functions under inelastic performance of the soil-pile system is explained in the following sections.

7.2.1. Description of FE analysis

A set of 3D finite element analysis of the soil-pile interaction for a large diameter RC shaft was carried out to extract the impedance functions under controlled monotonic and cyclic loads applied to the pile head. The analyses involve a single pile shaft with a diameter of D_p=2.3 m embedded in a homogenous soil continuum, with two different lengths of 15m and 30m to represent short rock socketed and long hinged-tip piles, respectively. The stress-strain behaviour of the soil is modelled using linear elastic and elastoplastic soil

models. Two types of soil-pile interface are considered: simplified rigid bonding and elasto-perfectly plastic contact elements, described previously in Chapter 3. The linear elastic soil model and the rigid soil-pile interface bonding are used for the purpose of validating performance of the back-calculating method proposed in this study. Because, these modelling conditions are the assumptions underlying previous studies which suggest equations for the modulus of subgrade reaction. The soil's elastoplastic constitutive model along with the soil-pile contact elements are used to identify variations of the impedance functions under fully inelastic performance of the soil-pile system. The pile model is assumed linear elastic with the flexural stiffness of E_pI_p=343000 MN.m^2 in all of the analyses in order to limit the system inelasticity effects on soil behaviour. Table 7.1 presents elastic properties of the soil and pile used in pile head loading analysis.

Table 7.1. Input elastic parameters for the soil and pile models

Element	constitutive model	V_s (m/s)	G_r *	E_r	B_r	S_u(kPa)	E_pI_p (MN.m^2)	D_p (m)
Soil	linear elastic	80	10.2	28.7	47.8	—	—	—
	nonlinear inelastic	130	27	75.7	126.2	45	—	—
Pile	linear elastic	—	—	—	—	—	343000	2.3

V_s: shear wave velocity; G: Shear modulus; E: modulus of elasticity, B: Bulk modulus; S_u: Undrained shear strength
G: Shear modulus; E: modulus of elasticity; B: Bulk modulus (Mpa)
* "r" denotes small-strain value of the parameter

Two types of displacement-controlled loading mode are applied to the pile head in the FE experiments: pseudo-static and cyclic. In the static loading, the imposed displacement is increased incrementally and the corresponding load at the pile head is recorded to

identify the ultimate lateral pile resistance as well as the lateral bearing strength envelope of the pile. In the cyclic mode, frequency content of the loading time history must sweep a wide-band frequency range to capture frequency-dependent characteristic of the soil-pile interaction. Hence, a linear chirp (Eq. 7.1) and a mono-frequency damped sine (Eq. 7.2) displacement time histories are used herein to investigate different aspects of dynamic soil-pile interaction. The former which is a sine sweep function is used to investigate linear elastic soil-pile interaction, and also discriminate influence of the soil and interface nonlinearity over a broad range of frequency. The latter time history, on the other hand, is used to characterize the nonlinear soil-pile interaction by computing the equivalent-linear pile head impedances, because the damped sine function represents realistically the displacement response of a superstructure vibrating at the fundamental frequency and damping ratio of the system, with a limited number of cycles. Moreover, with the chirp input displacement, the pile undergoes several constant-amplitude displacement cycles prior to the time of the frequency for which computation of impedances is intended, which in turn, leads to accumulation of plastic soil deformation, permanent gap and consequently degradation of lateral stiffness around the pile in the fully nonlinear interaction. Therefore, the impedances computed from result of the linear chirp excitation would not reflect realistic pile dynamic stiffness and damping ratio.

$$\gamma_{chirp}(t) = \sin\left[2\pi\left(f_0 t + \frac{\kappa}{2}t^2\right)\right] \tag{7.1}$$

$$\gamma_{damp}(t) = e^{-\lambda t}\sin\left(2\pi f_c\right) \tag{7.2}$$

In the chirp equation, f_0 denotes the lower-bound frequency in the swept frequency range, and κ denotes the rate of frequency change over duration of the time history. The linear chirp function covers a frequency range between 0.1 to 10 Hz within the duration of 10 seconds. The parameters λ and f_c denote the decay constant and excitation frequency of the damped sine function, respectively. The excitation frequency f_c varies from 0.5 to 6 Hz to cover a frequency range of interest for most infrastructure systems. Fig. 7.1 depicts time histories and Fourier transform amplitude of the prescribed linear chirp and damped sine functions.

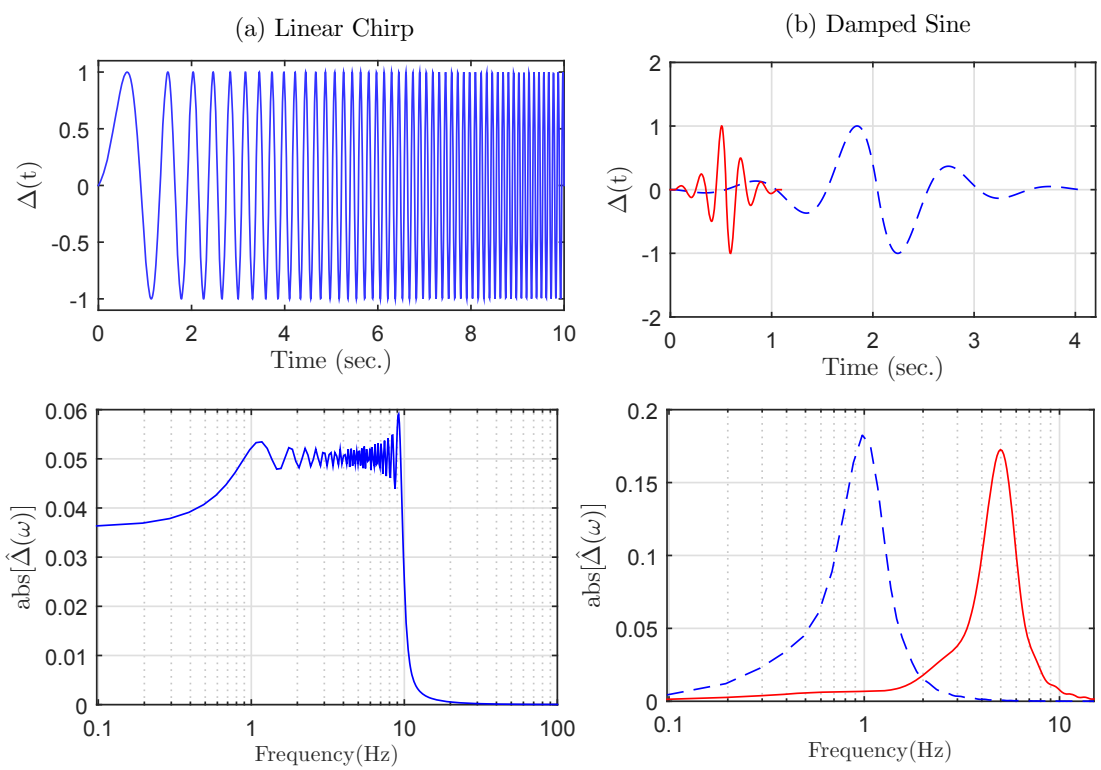

Figure 7.1. Time history and Fourier amplitude of the pile head excitations (a) Linear chirp, (b) Damped Sine

The lateral boundary of the soil domain must be treated appropriately in order to simulate damping of the outgoing waves emanated from the pile head in the far field soil and avoid their spurious reflection at the boundaries. The wave reflection highly matters in elastic interaction problems whereas in the inelastic one, a significant part of the wave energy is absorbed at the soil-pile interface with the aid of material damping as will be shown later in the following sections. In this study, the absorbing response of the unbounded soil domain is modelled by placing the lateral boundaries at a far enough radial distance from the disturbance source (pile) in conjunction with employing a type of absorbing boundary layer so-called "sponge layer" to attenuate the reflected waves back into the model. A sensitivity analysis was carried out with respect to the size of FE soil domain involving radial source to boundary distance of $10D_p$, $15D_p$ and $20D_p$ to determine the optimum size of FE domain. From results of these analyses and with due consideration to minimizing the computation effort, a radial size of $15D_p$ is adopted for all pile head dynamic analyses.

In context of the "sponge layer", which was first adopted by Varun et al. (2009) for elastic analysis of caisson foundation of bridges, attenuation of outgoing waves is enforced within the sponge region by means of Rayleigh damping which is used to prescribe artificial damping in the FE analysis. The enclosing region consists of several outermost layers of the FE domain, in which Rayleigh damping is progressively increased with increasing radial distance of the element from the pile. For the purpose of this study, four outermost boundary element layers make up the sponge region, with Rayleigh damping of 2 to 16 percent, assigned to the region following the procedure described in Torabi and Rayhani (2014). It should be noted that the natural frequency of the soil domain ($f_n =$

$v_s/4H_s$) is set as the target frequency in the Rayleigh damping formulation. Further details on the mechanism of "sponge layer" can be found in the work of Varun et al. (2009).

7.2.2. Static loading

The pile head stiffness and modulus of subgrade reaction under static loading condition are considered as benchmark data for interpretation of the dynamic behaviour. Therefore, it is essential to first conduct finite element analysis of the pile response under static lateral loading. The static analysis begins with finite element simulation of soil-pile interaction in linear elastic soil and rigid interface bonding in order to evaluate the obtained equivalent modulus of subgrade reaction with the values given by existing expressions in literature. The equivalent wavenumber at zero frequency ($\bar{\lambda}_0$) is computed for the long hinged-base and short rock-socketed piles by solving Eqs. 6.45 and 6.39, respectively, in which the real values (static condition) of the pile head displacement and force and $\hat{\phi}_{gk} = 0$ (head loading) are inserted. Table 7.2 compares the FE-based normalized Winkler modulus ($\bar{\delta}$) with those given by the formulas proposed by other researchers, which are expressed as:

$$\bar{\delta} = 4E_p I_p \bar{\lambda}^4 / E_s \tag{7.3}$$

$$\delta = 3.5\left(E_p / E_s\right)^{-0.11} \qquad \text{Syngros (2004)} \tag{7.4}$$

The comparison shown in Table 7.2 indicates that the computed moduli in this study is in close agreement with the values given by Eq. 7.4. Also, the computed moduli are consistent with the conclusion of Gazetas and Dobry (1984), suggesting a range of 1.5-2.5 for δ values for free head piles.

Table 7.2. Verification of subgrade modulus with other studies

Pile	Length	V_s (m/s)	E_p/E_s	$\hat{\delta}$	δ_{DG}	δ_S
short Fixed-tip	12	80	870	1.64	1.5-2.5	1.61
long Hinged-tip	30	130	330	1.49	1.5-2.5	1.78

$\hat{\delta}$: Modulus from this study, δ_{DG}: Dobry and Gazetas (1982), δ_S: Syngros (2004)

The static push over analysis is extended to a realistic interaction problem involving nonlinear soil and interface behaviour in order to characterize degradation of the equivalent modulus of subgrade reaction and the corresponding head impedances with increasing imposed displacement at the pile head. In nonlinear analysis, the imposed displacement at the pile head is incrementally increased until the lateral resistance of the pile reaches failure state. The failure load is determined at loading increment where tangent stiffness equals to 1% of the initial. Similar to the elastic analysis, the equivalent zero-frequency wavenumber is computed for each loading increment, and the corresponding pile head stiffnesses are computed subsequently. Fig. 7.2 shows variation of the computed static equivalent-linear subgrade modulus with pile head displacement. In this figure, modulus degradation is illustrated by normalized stiffness and displacement quantities. The subgrade modulus is normalized with respect to the soil's modulus of elasticity (E_s) and undrained shear strength (S_u), with values as shown in Table 7.1. The pile head displacement (u)is also normalized

by the parameter (u_{50}) denoting the displacement at which 50% of the failure lateral capacity of the pile is mobilized. As shown, almost 80% of the idealized elastic subgrade modulus is degraded due to pile-soil gap creation and inelastic soil behaviour around the pile shaft before 50% of the lateral capacity is mobilized.

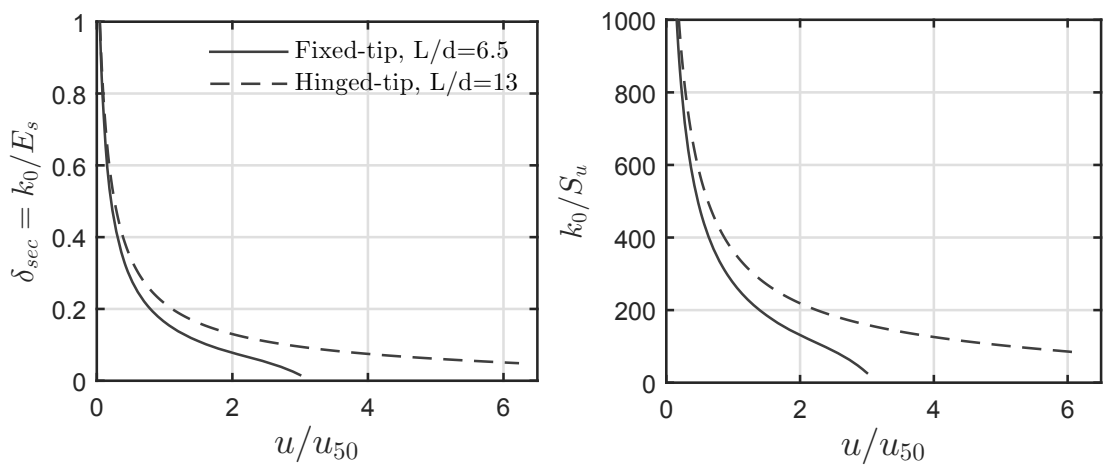

Figure 7.2. Degradation trends of average subgrade stiffness modulus with the increasing pile head stiffness

As explained in Chapter 6, representation of the lateral soil-pile interaction even in the elastic state with the equivalent homogeneous bed of independent springs is associated with error. This calibration error is expected to increase in fully inelastic soil-pile interaction where variation of the subgrade modulus along the pile length becomes progressively inhomogeneous due to inelastic soil and interface deformation. For evaluation of margin of this error, the pile head lateral force is reproduced at each lateral displacement increment by using the computed head stiffness ($\bar{k}_{uu}, \bar{k}_{u\theta}$), and compared with that from the continuum model as follows:

$$\overline{P}_H = \bar{k}_{uu}.u_p + \bar{k}_{u\theta}.\theta_p \tag{7.5}$$

$$\varepsilon_p(\%) = \frac{\overline{P}_H - P_H}{P_H} \tag{7.6}$$

where ε_p denotes the estimation error in percent, $\bar{p}_H$ and p_H denote the estimated and recorded pile head forces, respectively, which are compared schematically in Fig.7.3. As expected, the failure lateral capacity of the short rock-socketed pile is larger than that of the long hinged-tip one due to contribution of the flexural stiffness of the pile's cross section. Fig. 7.3b demonstrates variation of the estimation error with increasing imposed lateral displacement for the fully elastic rigid interface and the fully inelastic interactions of short fixed-tip and long hinged-tip piles. From the plot for elastic interaction, the estimation error solely due to the assumption of independent homogeneous Winkler spring is 5.6% and constant with the imposed displacement. For the inelastic cases, the error is shown to be influenced by the lateral pile performance such that in the 30m hinged-tip pile, the error progressively increases with increasing pile head displacement and approaches to an asymptotic value of about 10%, whereas in the 15m fixed-tip pile, the maximum error value of 10% is reached at much lower u/u_{50} ordinate, thereafter, it decreases until reaching zero at $u/u_{50} = 2.5$. This is because the surrounding soil yields at smaller head displacement in the short pile, above which the pile's flexural stiffness dominates the lateral bearing capacity mechanism. For design purposes, it is important to identify the margin of error within the range of design load which is considered as 67% of the ultimate lateral resistance of a drilled pile shaft, according to AASHTO LRFD (2012) guidelines. The specified design load limits in Fig. 7.3a indicate corresponding ε_p values of less than 10% for both the pile cases, which is an acceptable range of error.

In Fig. 7.3b, effects of the soil stiffness and inhomogeneity on the calibration error are shown and compared. As shown, soil stiffness has minor effect on the margin of error while the error shows sensitive response to the soil inhomogeneity in lower displacement values. Hence, it can be concluded that the calibration error is attributed to a great extent to the assumption of homogeneous subgrade modulus, particularly in the top few meters from the pile head where shear force gradient is high.

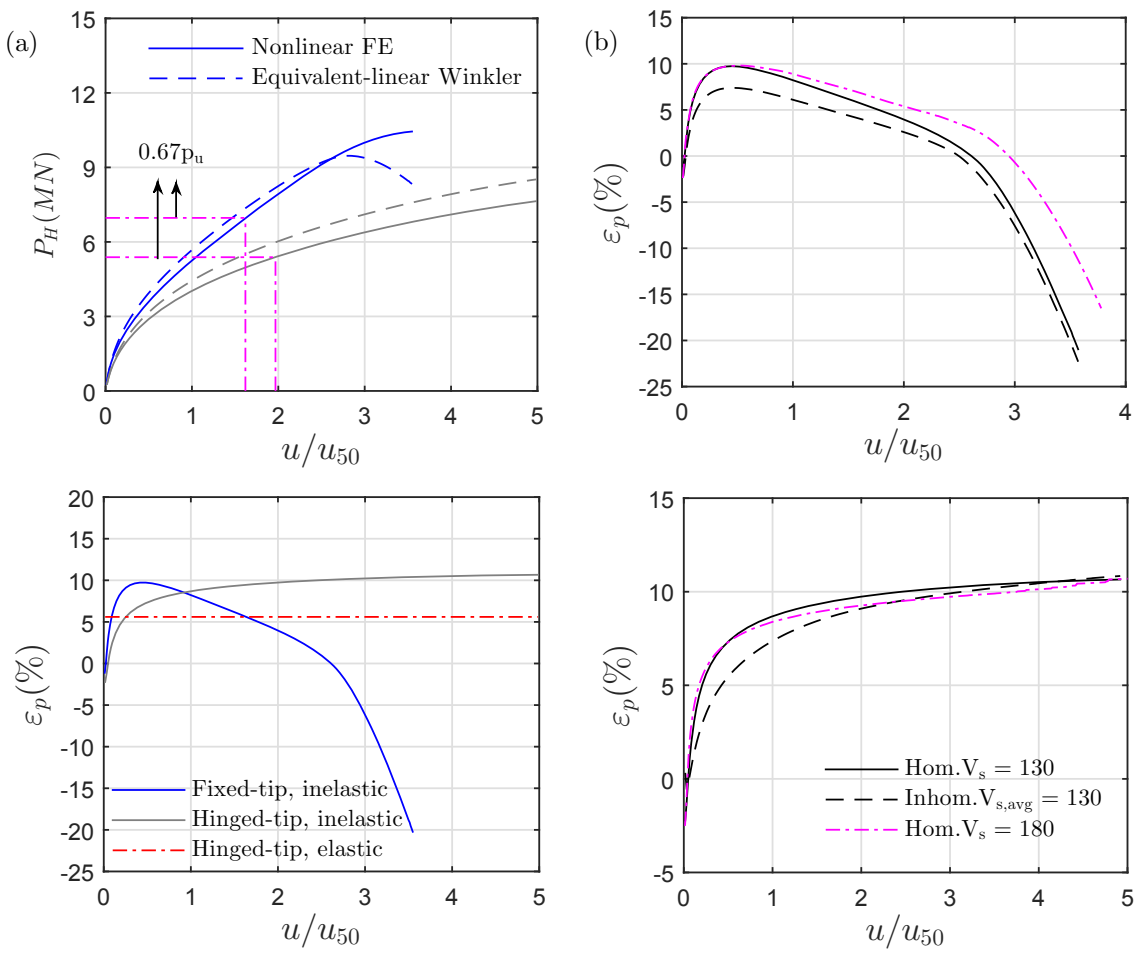

Figure 7.3. Comparison between a) the pile head forces from the nonlinear FE and the approximate average Winkler models b) the estimation error in three different configurations of soil deposit.

Fig. 7.4 demonstrates degradation of the static pile head stiffness versus lateral displacement (u/u_{50}) in the three displacement modes for the fixed-tip 15m and hinged-tip 30m piles. This plot also compares the degradation trend between two different values of soil stiffness (V_s=130 and 180 m/s). The stiffness degradation is shown by normalizing the equivalent-linear head stiffness (i.e. k_{uu}) with respect to its fully elastic counterpart ($k_{uu,e}$). In general, comparison between the degradation trends for all the modes indicate that stiffness degradation is significant in the horizontal mode for both the pile cases while in the rocking and cross-coupling modes, the fixed-tip pile exhibits considerable resistance against loss of lateral support. This implies that restraining the tip of a short pile with length less than corresponding active length significantly improves the rotational capacity of the pile. Moreover, it should be noted that the active pile length is expected to increase with further softening of the pile's lateral support. This can be justified by considering that the λL value controls the mechanism of lateral pile response and the λ value progressively decreases with evolution of soil softening and loss of interface contact. Hence, the pile must be long enough to make λL value larger than 2.5 in order to avoid rigid pile behaviour (short pile). With regard to the effect of soil stiffness, it is shown that the difference between the degradation values remain constant over the entire range of imposed head displacement. This difference is attributed to the stiffness reduction due to evolution of the pile-soil gap opening, which is independent of the soil stiffness and constant in both cases. Therefore, normalization of this reduction by the initial fully elastic stiffness which is higher for the soil with V_s=180 m/s results in lower degradation values.

The stiffness reduction trends shown in Fig. 7.4 can be interpreted as the nonlinear force-deformation element (spring) for use in the substructure analysis of a typical long

flexible pile and a short fixed-tip pile. Therefore, it would be useful to derive a functional form that best describes this stiffness softening trend mathematically. The power function has been primarily used to formulate the generic *p-y* curves for estimation of ultimate lateral pile resistance (Matlock 1970, Boulanger et. al 1999). Hence, the hyperbolic function which can be considered as a rational form of the power functions is adopted herein to model the stiffness softening trend. After trying several linear regressions on various forms of the hyperbolic function, the following forms are determined to provide the best-fit while the number of coefficients in the model are kept minimum:

$$\frac{k_{ij}}{k_{ij,e}} = \frac{1 + a_0 \left(u/u_{50}\right)^{a_1}}{a_2 + a_3 \left(u/u_{50}\right)^{a_4}} \tag{7.7}$$

$$\frac{k_{ij}}{k_{ij,e}} = \frac{1}{a_1 + a_2 \left(u/u_{50}\right)^{a_3}} \tag{7.8}$$

From the regression analysis, Eqs. 7.8 and 7.9 were determined to provide the best-fit for the fixed-tip short and hinged-tip long pile cases, respectively, with a R-square (coefficient of determination) value of 0.99. The reason for relatively different fitting functions can be justified by the fact that soil inelasticity dominates stiffness degradation in the latter case, whose stress-strain response is in turn simulated by the hyperbolic model, whereas in the former case, structural stiffness of the pile significantly contributes to the overall lateral pile stiffness.

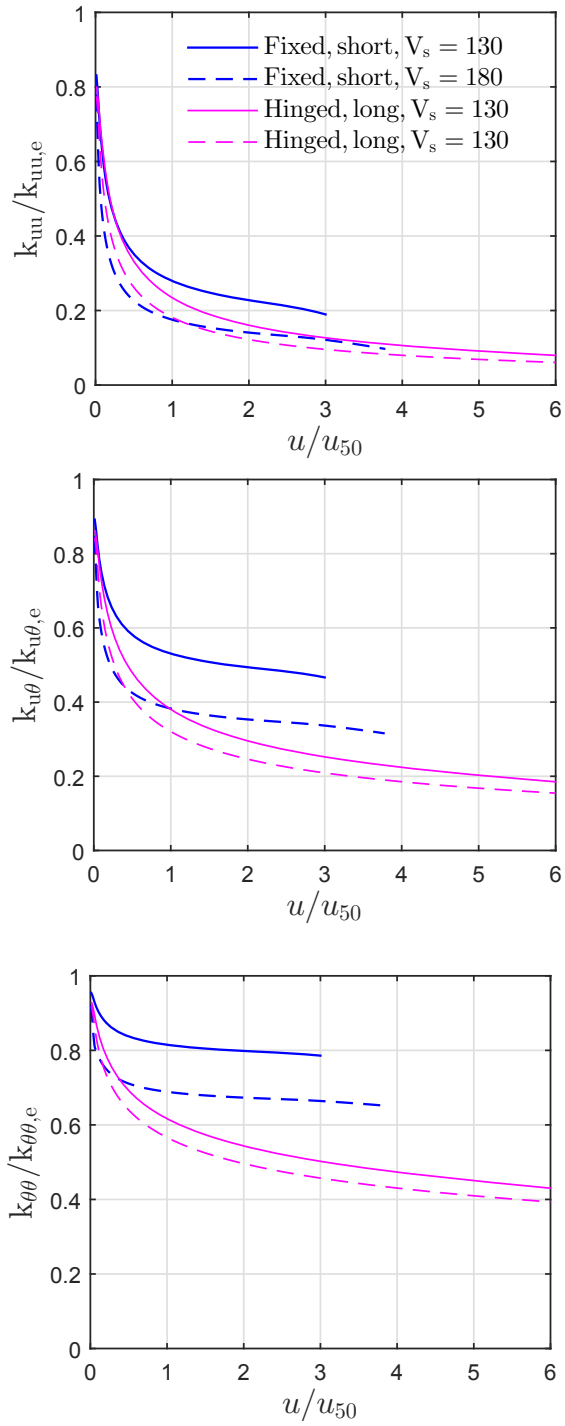

Figure 7.4. Schematic of the pile head stiffness degradation trend in two different soil and pile cases for the horizontal, rocking and cross-coupling displacement modes

7.2.3. Dynamic loading

The goal of this section is to characterize dynamic pile head impedance functions under the influence of soil and interface inelasticity. Given that the developed expressions for the trend of nonlinear stiffness degradation under monotonic loading may be used in the seismic substructure analysis, it is necessary to evaluate their appropriateness by comparing them with the frequency-dependent impedances derived from dynamic loadings. In particular, special focus is given on identifying the energy dissipation through hysteretic and radiation mechanisms which can be significant in large diameter pile shafts in soft soil. Focusing on derivation of the pile impedance functions, a massless pile is considered in numerical analysis of the pile with dynamic head loading in order to eliminate the effect of inertial forces in frequency response of the soil-pile system. Table 7.3 presents details of the displacement-controlled dynamic pile analysis.

Table 7.3. Details of analysis for dynamic characterization of pile head impedances

Input Excitation	Soil behaviour	Interface	Amplitude (m)	frequency (Hz)
Sine Sweep	linear elastic	rigid	0.01	0.1-10
	nonlinear inelastic	rigid/contact		
Mono-freq. Damped sine	nonlinear inelastic	contact	0.002-0.18	0.5-6

In all analyses, shear wave velocity of the soil deposit is 130 m/s and the pile is a RC shaft with diameter of 2.3m All analyses are conducted for the fixed-tip and hinged-tip piles in the soil deposit thickness of 15m and 30m, respectively.

7.2.3.1. Effects of soil and interface inelasticity

As the first objective in the dynamic analysis, the linear chirp excitation is applied to the free head of the pile to shed light on the role of interface and soil nonlinearity on the interaction mechanism. The pile models are identical to those in static analysis, embedded in 15m and 30m soil deposits with V_s=130m/s on an elastic bedrock. The amplitude of the linear chirp excitation is 1cm in order to induce moderate level of soil inelasticity. The obtained results are presented and discussed in the form of average EL subgrade and pile head impedances computed using Eq. 6.39 and 6.45 for the soil-pile cases including linear elastic soil with rigid interface bonding, inelastic soil with rigid interface, and inelastic soil with interface element. Fig. 7.5a, b shows comparison of the subgrade modulus (real part) and the dashpot coefficient (imaginary part) between these cases for the fixed-tip short and hinged-tip long piles, respectively. Both plots demonstrate the significant impacts of the soil and interface inelasticity on dynamic stiffness and damping characteristics of the pile. Fig. 7.5b validates the computed damping coefficient for the fully elastic case by comparing it with the analytical plain-strain model by Gazetas and Dobry (1984), which shows a good match between the two data. The comparison is shown for only the frequency range of radiation damping existence. Because the computed damping is in the soil deposit on a rigid bedrock, as opposed to the model values that are for piles in semi-infinite elastic half space in which the damping value yields to infinity at very low frequencies.

As shown in both plots, the linear elastic soil assumption leads to a noticeable overestimation of subgrade modulus and damping coefficient even under small displacement amplitude. Moreover, it causes large oscillation (peaks and valleys) at the characteristic frequencies of the soil-pile system. Basically, the frequency-domain

variation of the stiffness and damping of any SSI problem in shallow soil deposit over rigid bedrock exhibits undulation (Gazetas 1983,1984). This is resulted from resonance between the natural frequencies of the soil deposit and the loading frequency, rendered by the standing wave due to multiple reflection at bedrock and ground surfaces. As a result, vibrating foundation emanates larger amount of energy to the soil domain (radiation damping) with smaller resistance by the surrounding soil. In the soil-pile case of this study, the valleys exhibited by the stiffness and the peaks by the damping are found to occur at two characteristic frequencies of the system. The first one ($a_0 \approx 0.18$), which is shown to be identical between the two sites (15m, 30m) and the pile types, is the frequency of the soil-pile characteristic wavelength frequency, given by $\omega_\lambda = Re(\bar{\lambda}_\omega)V_s$. This frequency is a function of soil-pile relative stiffness parameter or characteristic wavenumber (λ) which controls attenuation of the dynamic excitation along the pile shaft and the soil shear wave velocity. The second one, which varies between the two soil deposits, is almost twice the first natural site period. Thus, it can be concluded that the resonance occurs at natural frequency for a combination of shear and dilational waves generated in the system due to multiple reflections. In overall, variation of the stiffness and damping exhibits fairly smooth trend without large spikes when inelastic soil and interface actions are allowed in the system.

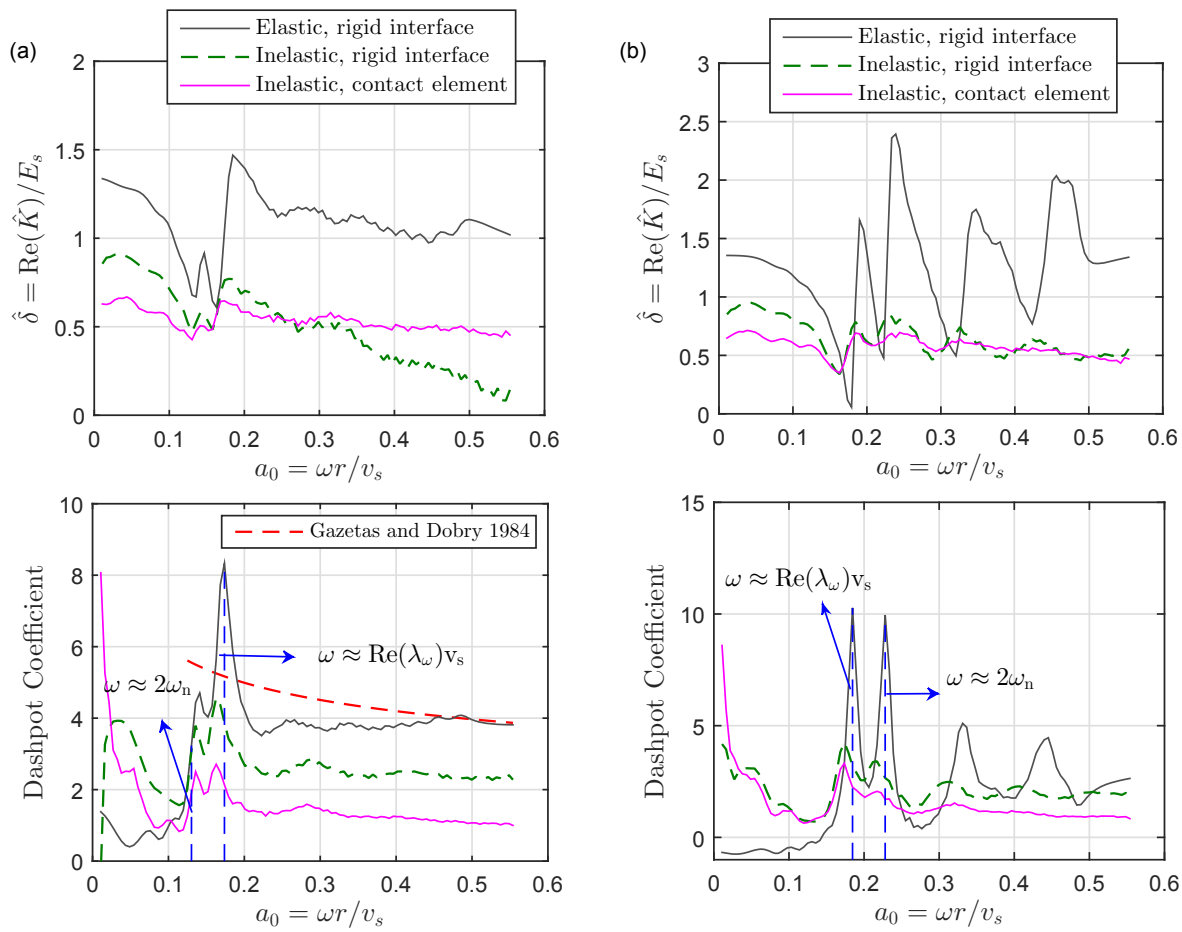

Figure 7.5. Comparison of dynamic subgrade stiffness modulus and dashpot coefficient between three different combinations of soil and interface behaviour for a) hinged-tip long and b) fixed-tip piles

In order to explore the effects of inelasticity on the pile head impedances, Figs. 7.6 and 7.7 compare the computed horizontal, rocking and cross-coupling dynamic stiffness and damping ratio of the pile head for the fixed-tip short and hinged-tip long piles, respectively. The computed parameters are defined in normalized form to be consistent with the reference solutions in literature, which are expressed for a representative horizontal mode as follows:

Horizontal mode: Dynamic stiffness= $\frac{\mathrm{Re}(\hat{K}_{uu})}{E_s d}$ (7.9)

$$\text{Damping ratio}=(D_{uu})=\frac{\mathrm{Im}(\hat{K}_{uu})}{2\,\mathrm{Re}(\hat{K}_{uu})} \tag{7.10}$$

where $\hat{K}_{ij} = k_{ij} + ic_{ij}\omega$ denotes the impedance function, E_s and d denote Young modulus of the soil and the pile diameter, respectively. The dynamic stiffness of the rocking and cross-coupling modes are normalized by d^3 and d^2, respectively, as displayed in Figs. 7.6 and 7.7. In both plots, the damping ratio of the inelastic soil with rigid soil-pile interface is shown to be notably overestimated in the frequency range where radiation damping is dominant. This indicates that the hysteretic damping is significantly overestimated by the rigid interface despite the adverse impact of the soil inelasticity on radiation damping. Moreover, these two plots demonstrate frequency range for the active damping mechanism. As shown, the natural site frequency of the shear wave which corresponds to a_0=0.6 in Fig. 7.7 and a_0=1.2 in Fig. 7.6 is the cut-off frequency for the radiation damping, below which, the vibrating pile is unable to emanate waves into the soil domain, and the frequency-independent hysteretic damping is the only acting dissipation mechanism. This is observed by comparing the damping trend of the inelastic and elastic soils. Such an observation was also reported by Gazetas (1984), but with a difference that in his work a huge jump of damping ratio occurs at the first natural site frequency for the shear wave, whereas, such a rise is observed at the frequency of the soil-pile characteristic wavenumber or the natural site frequency for combination of the shear and dilational waves, whichever is smaller.

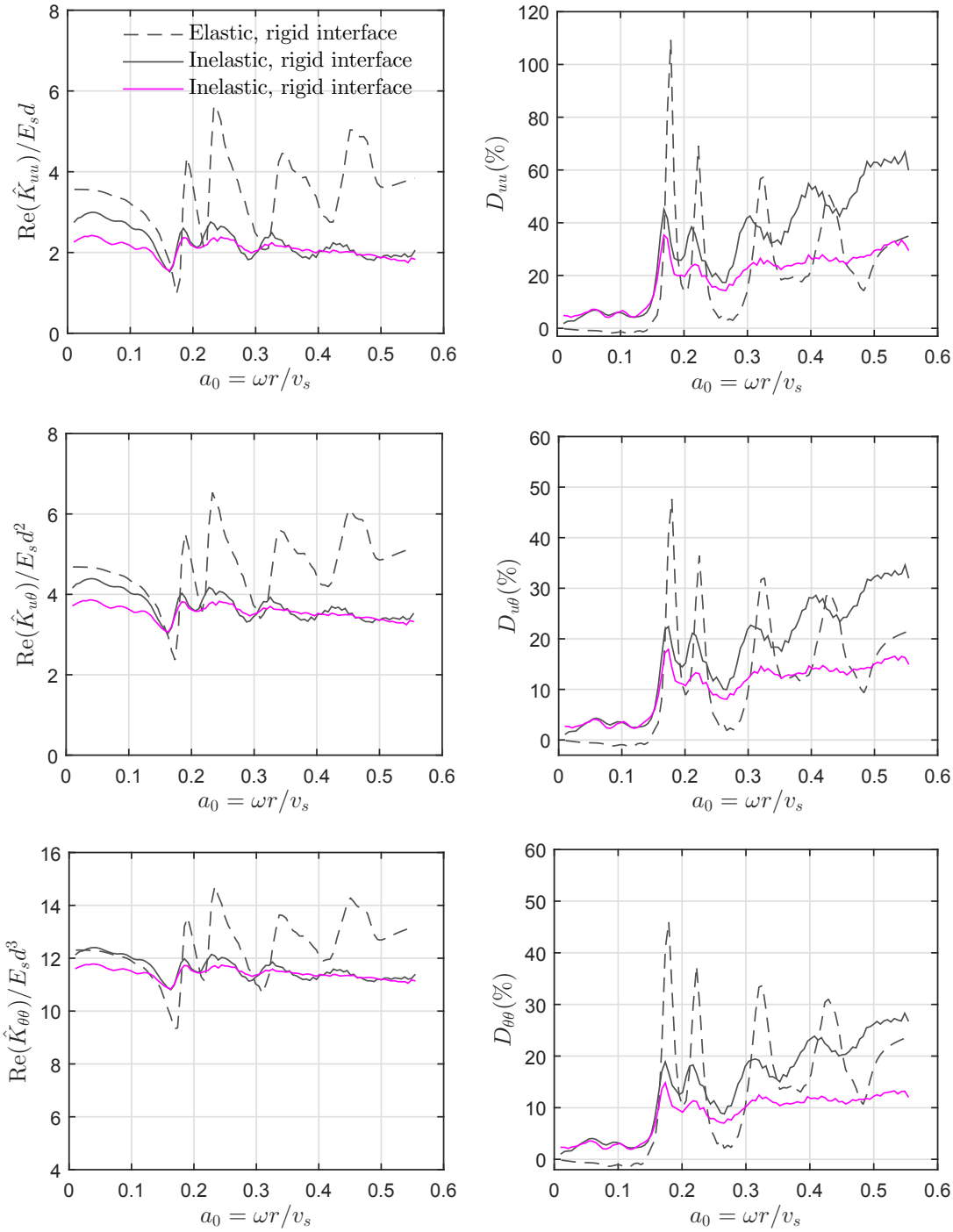

Figure 7.6. Comparison of the normalized dynamic pile head stiffness and damping ratio between three different combinations of soil and interface behaviour for horizontal, cross-coupling and rocking displacement modes in a fixed-tip short pile

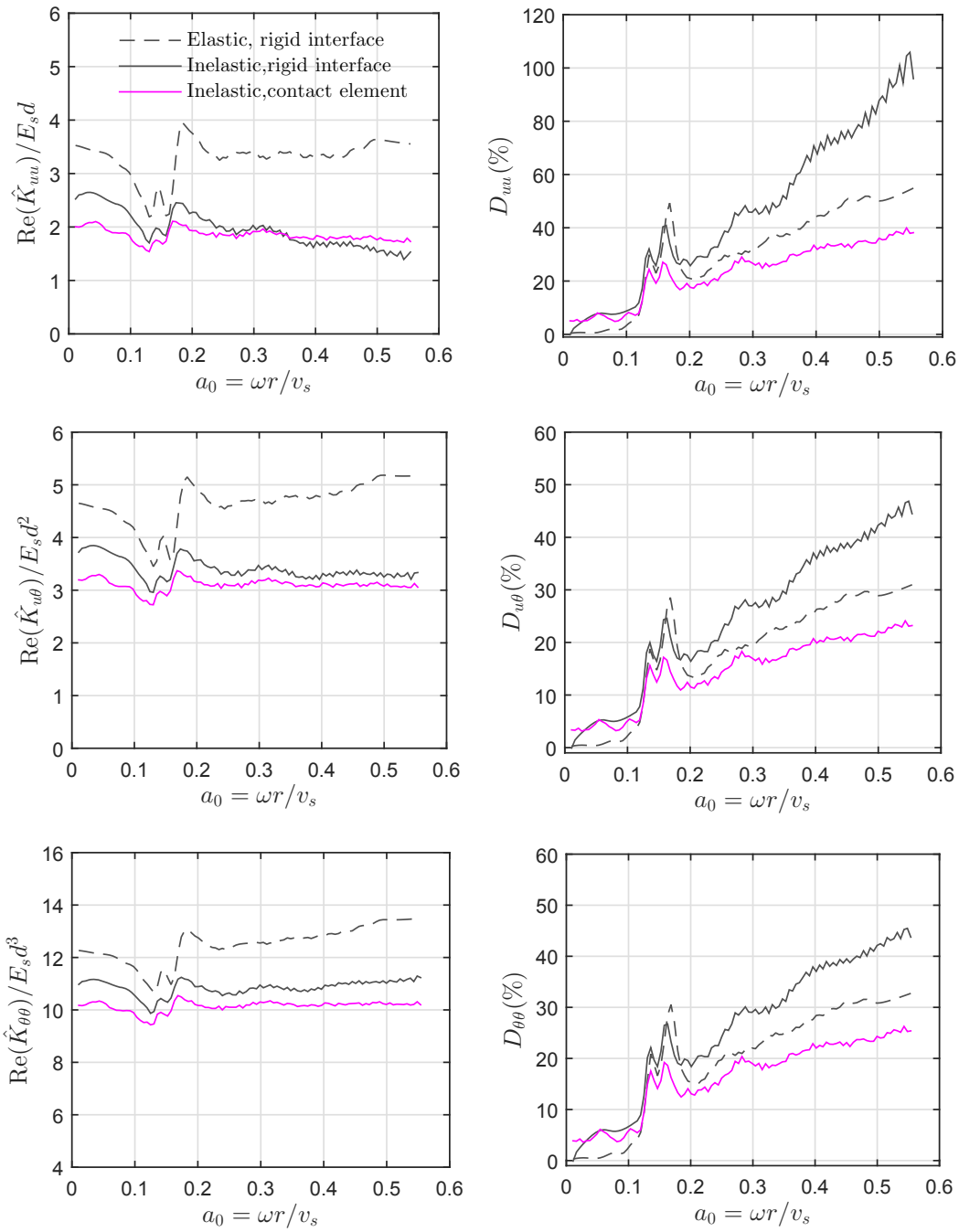

Figure 7.7. Comparison of the normalized dynamic pile head stiffness and damping ratio between three different combinations of soil and interface behaviour for horizontal, cross-coupling and rocking displacement modes in a hinged-tip long pile

7.2.3.2. Effect of inelasticity level on impedance function

In order to explore effects of level of soil inelasticity on the pile head impedance functions in frequency domain, the sine displacement excitations (Eq. 7.2) with a variety of combined loading frequency and amplitude are prescribed at the pile head. The loading frequency varies between 0.5-6 Hz, and the pile head normalized displacement (u/u_{50}) which controls the inelasticity level varies between 0.02-1.8 for the hinged-tip 30m and 0.03-2.5 for the fixed-tip 15m piles, respectively. Fig. 7.8 displays the comparison between the degradation trend of the pile head static stiffness discussed in Section 7.2.1 and those of the dynamic ones. As shown, the degradation values become less sensitive to loading frequency with increasing the level of inelasticity (u/u_{50}). A wide range of sensitivity is observed in the horizontal mode (K_{uu}) compared to the rocking one. The lower bound values of the sensitivity range, which are displayed by solid data points, correspond to the frequency of the soil-pile characteristic wavenumber (ω_λ). As explained in the previous section, this frequency is associated with local peak of the damping ratio and its corresponding minimum dynamic stiffness. In general, the static trend is shown to well represent the dynamic trend especially at higher displacement and inelasticity values.

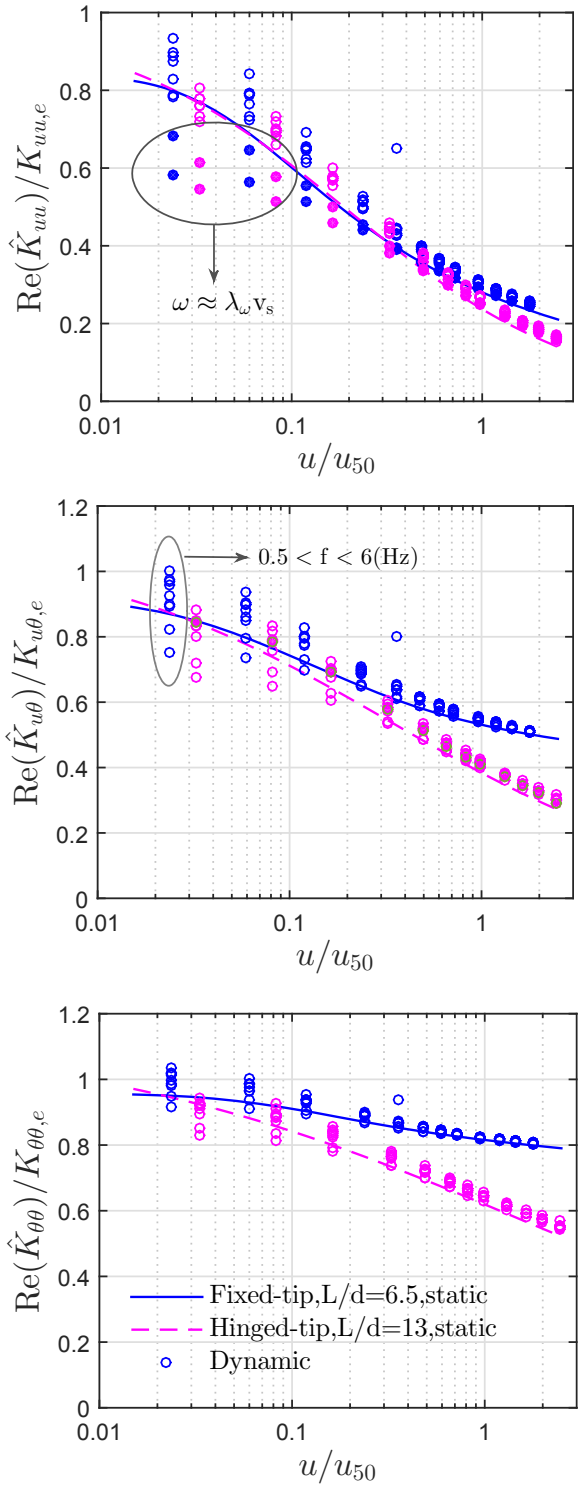

Figure 7.8. Comparison between the dynamic and static pile head stiffness degradation trends of fixed-tip short and hinged-tip long piles for the horizontal, cross-coupling and rocking modes

Fig. 7.9 shows variation of the resulting pile head damping ratio with loading frequency and amplitude. In both plots, the crucial characteristic frequencies including the natural site period for shear wave (f_n), the combined wave forms ($\sim 2f_n$), and the frequency of the characteristic wavenumber (ω_λ) are shown. As expected, the frequency-dependent radiation damping exists in a frequency range with the lower boundary value of f_n, while a jump in the damping value is observed at ω_λ and $2f_n$. This is consistent with the damping trend shown in Figs. 7.6 and 7.7. Of special interest, such a jump is shown for the lower level of the loading amplitude which induces small amount of hysteretic damping, and it vanishes as the loading amplitude increases. This is because the hysteretic damping increases with increasing inelasticity on one side, while on the radiation damping side, the inelastic deformation together with the widened interface opening suppress the radiation damping. This mechanism leads to a fairly linear variation of the pile head damping ratio with frequency at large displacement amplitudes. For clear illustration, Fig. 7.10 shows three-dimensional variation of the damping ratio with respect to frequency and amplitude of the pile head loading. As shown, the damping value at characteristic frequency of ω_λ (a_0=0.18) is significant for lower u/u_{50} values, and it decays with increasing the u/u_{50} value. In other words, the frequency-dependent characteristic of the damping is maintained over the entire frequency range of study. Moreover, the hinged-tip long pile exhibits higher damping values with increasing the u/u_{50}, compared to those of the fixed-tip short pile. This is mainly because of lower degradation of the soil-pile interaction stiffness in the fixed-tip case due to contribution of the pile's flexural stiffness.

Variation of hysteretic damping under a wide range of induced inelastic soil-pile interaction is shown in Fig. 7.10 by the damping ratio values for frequencies less than f_n.

As shown, the resulting maximum hysteretic damping is 7% for the long hinged-tip pile, while this value is 5% for the fixed-tip short pile. This slightly higher damping value of the long pile is attributed to the fact that in the case of long pile, the pile energy is mainly transmitted to the surrounding soil domain, and hence, it undergoes larger deformations. In overall, the maximum damping ratio for both the pile cases in the given frequency range (0.5-6 Hz) is shown to be less than 30%. In order to quantify the damping coefficient, Fig. 7.11 shows variation of the normalized dashpot coefficient for representative horizontal mode with the loading frequency under five levels of inelastic interaction. This coefficient is normalized with respect to Young's modulus of the soil (Gazetas 1984), and determined as follows:

$$C_{uu} = \frac{\mathrm{Im}(\hat{K}_{uu})}{\omega} \tag{7.10}$$

As shown, the dashpot coefficients for both pile cases under imposed displacement level of higher than u/u_{50}=0.5 yield to relatively frequency-independent dashpot coefficients between 1.5 and 2 MPa.s.

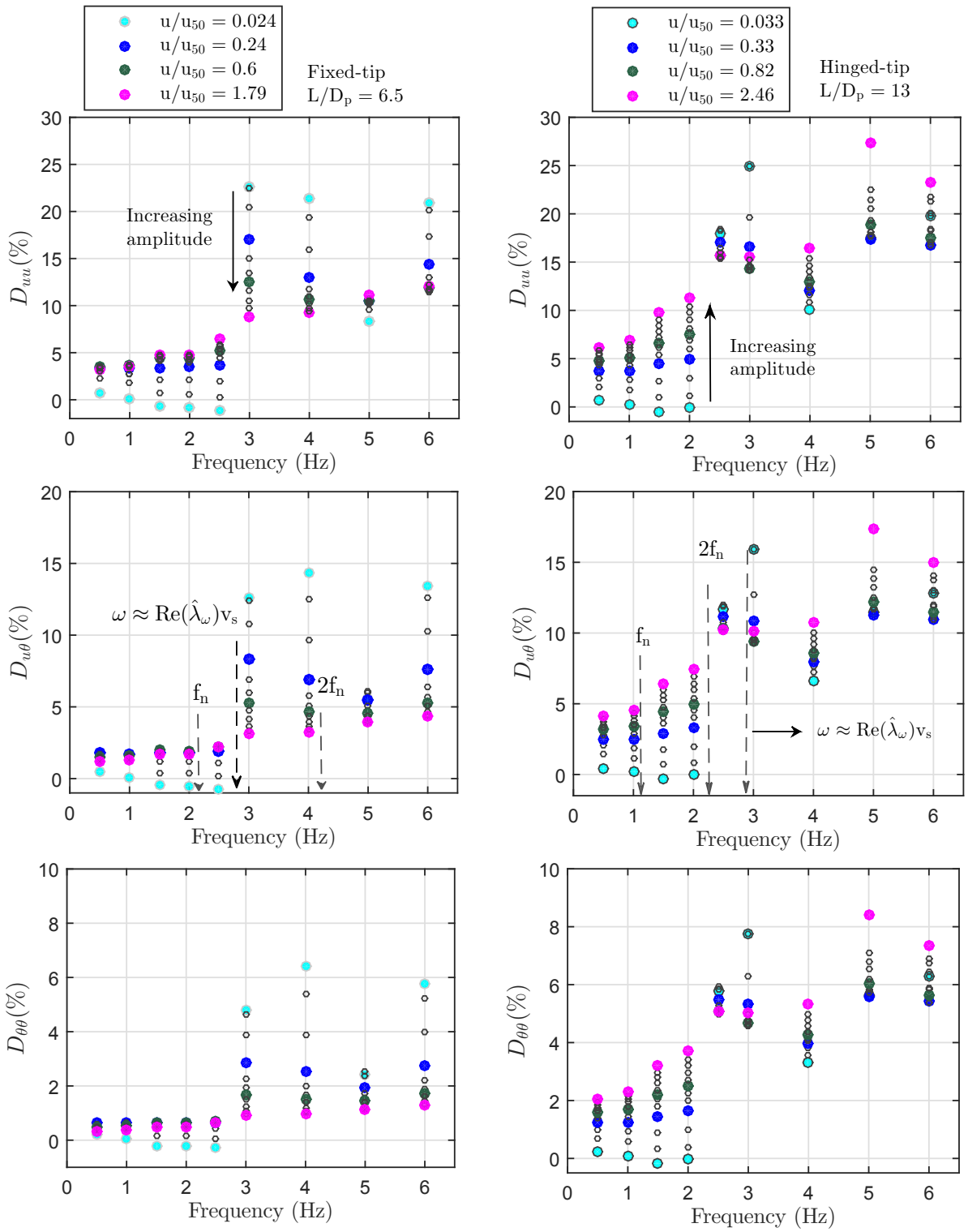

Figure 7.9. Frequency-domain variation of the pile head damping ratio under various inelasticity levels for two pile cases

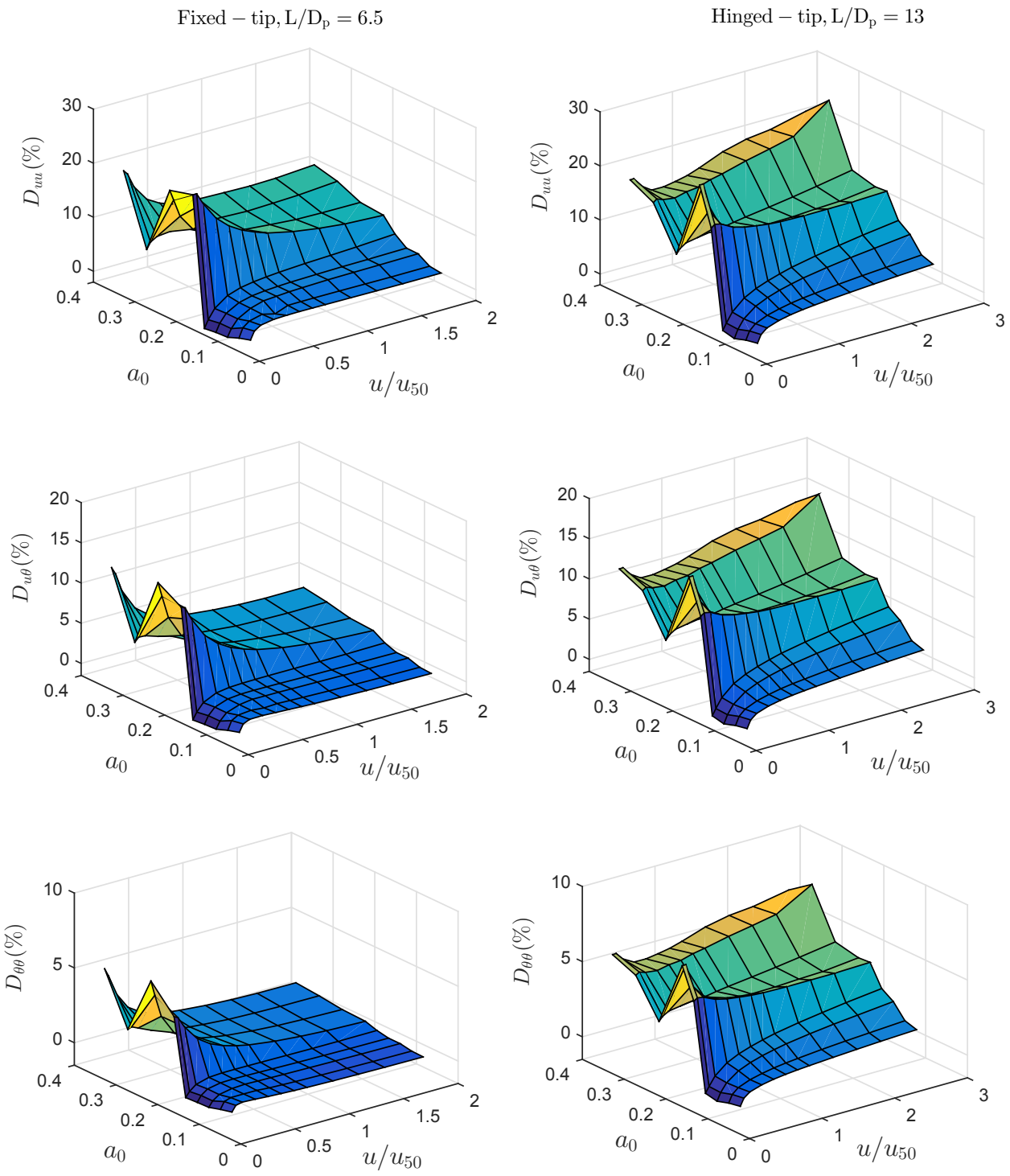

Figure 7.10. 3D variation of the pile head damping ratio with the frequency and pile head displacement for two pile cases

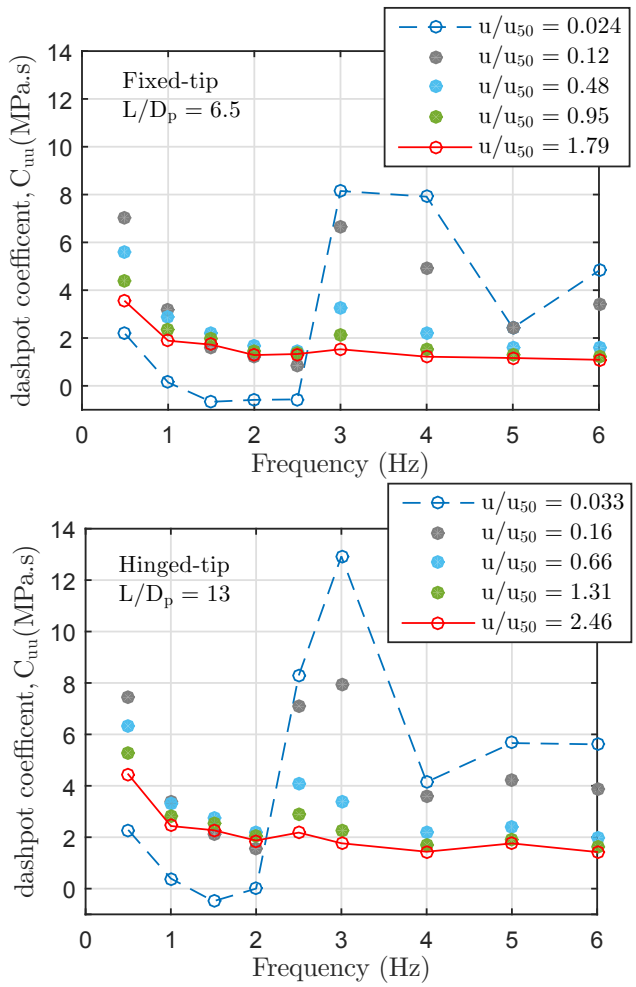

Figure 7.11. Frequency-domain variation of the pile head dashpot coefficient under various inelasticity levels for two pile cases

7.2.3.3. Effect of elastic soil stiffness on damping

In order to evaluate effect of soil stiffness on the soil-pile damping, Fig. 7.12 shows comparison between variations of the subgrade dashpot coefficient for the soil with small-stain V_s of 130 and 180 m/s. Fig. 7.12 shows the comparison in two different pile types for the minor and major inelasticity levels, respectively. Similar to the previous analysis, the inelasticity level is measured by the normalized pile head displacement (u/u_{50}). As shown,

the influence of inelasticity level is constrained to a very small displacement level, and mainly shifts the characteristic frequency of maximum radiation damping. This is because of change in the relative soil-pile stiffness, resulting in lower characteristic wavelength (higher frequency) in the soil medium with the higher V_s value. The effects of soil stiffness on the system damping (Fig. 7.12 c, d) is shown to vanish with increasing inelasticity level even at the u/u_{50} values of less than 1. This can be attributed to the interface gap opening and inelastic soil deformation which together suppress the pile radiation damping.

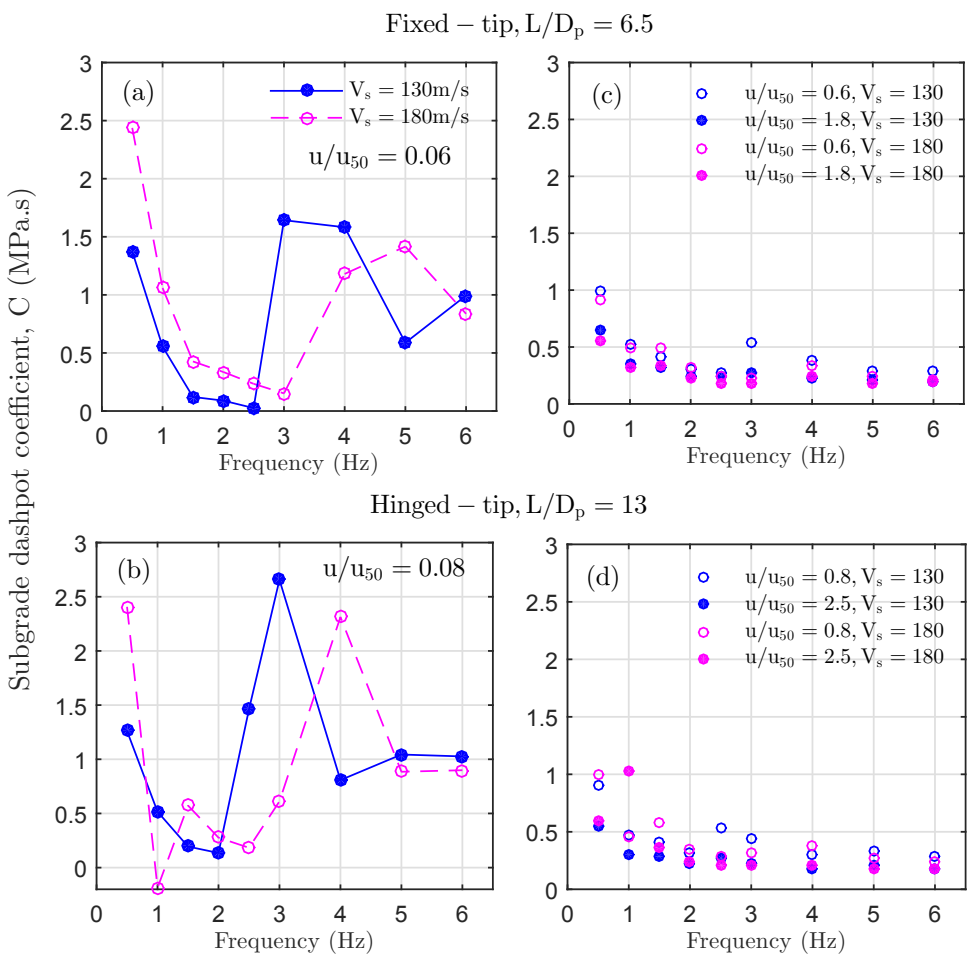

Figure 7.12. Effect of elastic small-strain soil stiffness on the subgrade dashpot coefficient

7.3. Computation of impedance functions: earthquake loading

In the previous section, the pile head impedance functions were computed under controlled static and dynamic loads prescribed at the pile head. This section describes computation of the average EL impedances under the earthquake excitation prescribed at the base of the soil domain using the closed-form back-calculating method. In other words, the impedance functions are derived for the coupled inelastic soil-pile-structure interaction resulted from propagation of seismic waves through the soil deposit and the consequent kinematic and inertial interactions. Moreover, reliability of the estimated impedances which are derived based on the assumption of representative homogenous bed of viscoelastic Winkler elements are examined. The impedances are estimated using results from the SPSI continuum models discussed in Chapter 5. These finite element models involve a 17m rock-socketed pile and a 30m hinged-tip pile in soil profiles with inhomogeneous soil stratification, which are subjected to twelve earthquake motions of various intensity levels (Table 5.3). The EL subgrade impedances are computed by solving Eqs. 6.39 and 6.45 at a given frequency for the short socketed and long hinged tip piles, respectively. Given that the frequency-domain formulation of the dynamic soil-pile interaction allows for superposition of the kinematic and inertial interaction effects, results from the continuum analysis of the only kinematic and the coupled inertial and kinematic interactions can be directly inserted in Eqs. 6.38 and 6.44.

In the first step, reliability of the computed impedances is evaluated by calculating the residual percentage between the pile head shear forces given by the computed impedance ($\hat{\bar{V}}(\omega_V)$) and from the continuum analysis ($\hat{V}(\omega_V)$). This is done at frequency (ω_V) of the maximum pile head shear force as follows:

$$\varepsilon_V = \frac{\hat{\bar{V}}(\omega_V) - \hat{V}(\omega_V)}{\hat{V}(\omega_V)} \tag{7.11}$$

in which,

$$\hat{\bar{V}}(\omega_V) = \hat{\bar{S}}_{uu}(\omega_V).\hat{u}(\omega_V) + \hat{\bar{S}}_{u\theta}(\omega_V).\hat{\theta}(\omega_V) \tag{7.12}$$

where $\hat{\bar{S}}_{uu}(\omega_V)$ and $\hat{\bar{S}}_{u\theta}(\omega_V)$ denote the computed horizontal and cross coupling average impedances, respectively. $\hat{u}(\omega_V)$ and $\hat{\theta}(\omega_V)$ denote the displacement and rotation of pile head from the continuum model. Fig. 7.13 shows distribution of the force prediction residuals in percent, given by the above equation for all the 96 soil-pile-structure cases under a wide range of maximum ground displacement response. A shown, in overall, 78% of the cases exhibits residual values within a range of $\pm$ 20% which is considered an acceptable range for inelastic problems. In detail, 52% of them shows residuals less than 10%.

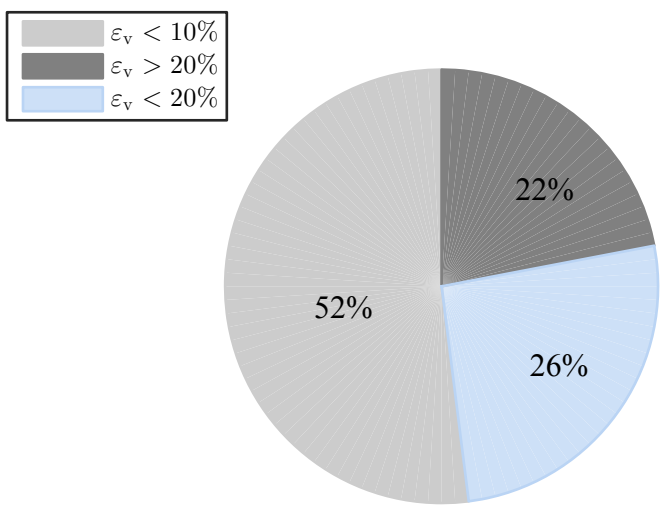

Figure 7.13. Distribution of force prediction residuals computed for all the SPSI cases under earthquake loadings

In order to identify the main influential factor in prediction reliability, Fig. 7.14a and b show two different illustrations of the computed residuals. In Fig. 7.14a, the residuals are compared based on the type of pile shaft, while the height of pier column is the basis of comparison in Fig. 7.14b, which in turn represents approximately two different frequency range of vibration. As shown, while almost equal number of the cases form each pile type exhibits residual values out of the $\pm$ 20% range in Fig. 7.14a, majority of these cases are shown in Fig. 7.14b to correspond to the superstructure with column height of 10m. More importantly, only seven of the 10m cases under $u_{g,max}$ values of greater than 0.1m exhibit residuals within the $\pm$ 20% range. The reason for such a large prediction residual can be justifiable by how variation of the pile stiffness with depth is included in the back-calculation procedure, because it largely depends on the pile stiffness value. This matters in the cases of this study, in which pile behaviour is modelled inelastic by nonlinear beam-column elements accounting for stiffness degradation. Thus, for simplicity, the average secant EI values within top 15m of the pile is used in the computations. Through the sensitivity analysis, it was concluded that non-uniform distribution of the pile stiffness in the above mentioned long period structures, which results from the stiffness degradation of the shaft under large displacement demand of the near-fault motion, can be the main cause undermining the prediction accuracy. The reason for such an impact is coincidence of the SPSI-induced lengthened period of the structure with the natural period range of site response, at which the maximum ground displacement response occurs.

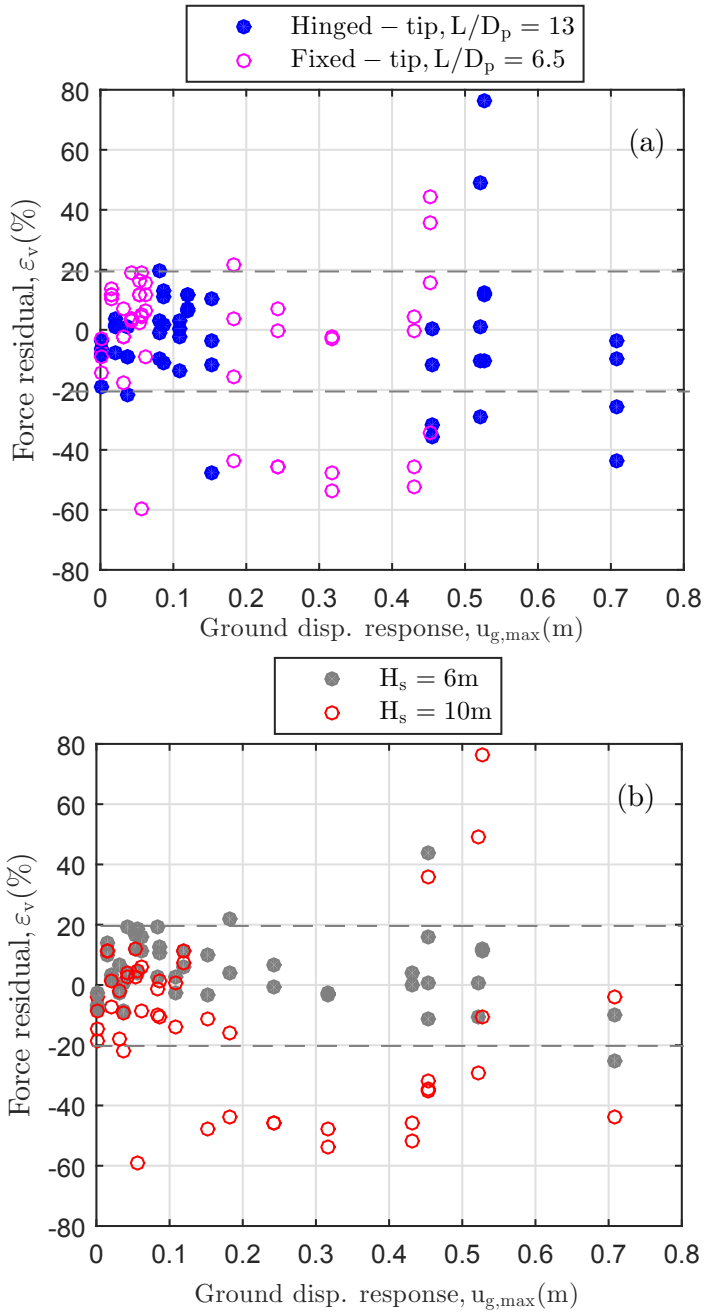

Figure 7.14. Force residuals computed for various SPSI cases under earthquake loadings, and compared based on a) pile type b) height of pier column

Fig. 7.15 shows the estimated average EL subgrade stiffness and damping coefficients computed for the cases with a prediction residual less than 20%. A sharp loss of stiffness is shown at small ground displacement levels, which is caused by spread of the interface gap opening along the pile shaft. The stiffness degradation continues at lower rate with increasing ground displacement level until it reaches the asymptotic $\hat{\delta}$ value of 0.1 at very large demands. The displayed subgrade damping values for a given ground displacement level shows a wide range variation with increasing the displacement level up to a displacement level of about 0.12m above which the dashpot coefficient fluctuates mainly within the range between 0.5 and 1.5 MPa.s. This indicates that under lower free field ground displacements which are associated with lower inelasticity level, dashpot coefficient may exhibit frequency-dependent behaviour. Moreover, the variation range of damping values for the hinged-tip long pile under strong near fault motions is shown to be smaller than that of the fixed-tip short pile.

Fig. 7.16 and 7.17 show the computed average EL pile head stiffness and damping, respectively, based on the back-calculated subgrade impedances. The dynamic spring coefficients for the three vibration modes are shown in normalized form as:

Horizontal: $\mathrm{Re}(\hat{\bar{K}}_{uu})/E_s\, D_p$

Rocking: $\mathrm{Re}(\hat{\bar{K}}_{u\theta})/E_s\, D_p^2$

Cross-coupling: $\mathrm{Re}(\hat{\bar{K}}_{\theta\theta})/E_s\, D_p^3$

In Fig. 7.16, the best-fitting trend from nonlinear regression analysis is also plotted for each vibration mode to show the average degradation trend of the pile head stiffness as the free field ground displacement increases. Unlike the presented spring coefficients, the absolute

values of the dashpot coefficients are shown in Fig. 7.18. This is because the damping trend of the pile becomes independent of the elastic soil parameters even under a moderate level of inelastic soil-pile interaction. As a conclusion, the presented average trends in Figs. 7.16 and 7.17 can be useful for determination of appropriate impedance values based on the maximum ground surface displacement in the free field soil for substructure analysis of the RC pile shaft.

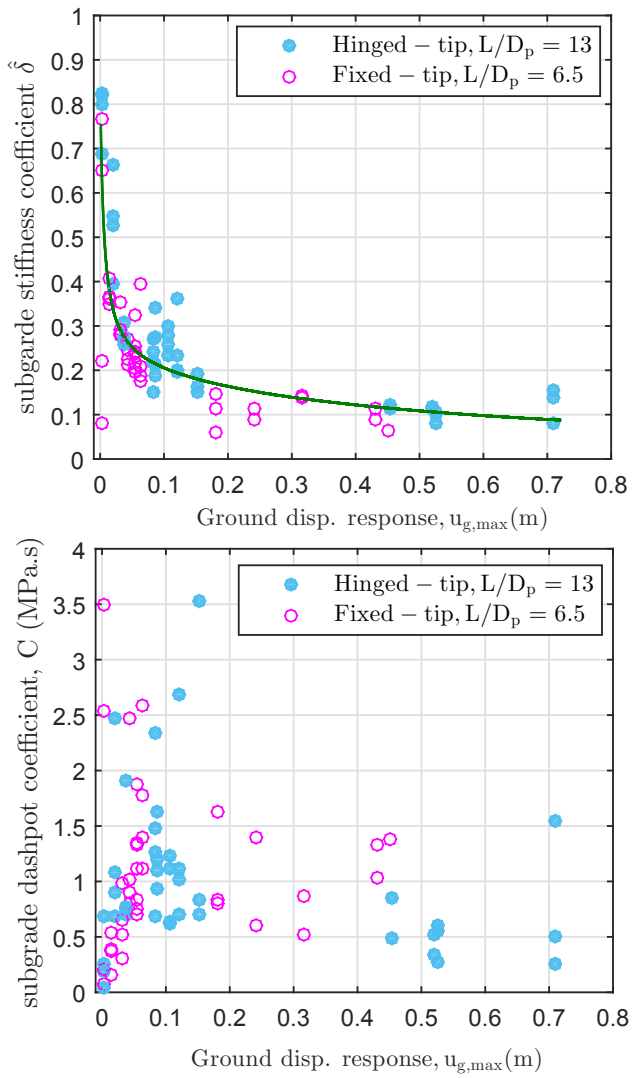

Figure 7.15. Variation of the average EL subgrade stiffness and damping coefficients of all the SPSI cases with maximum ground surface displacement

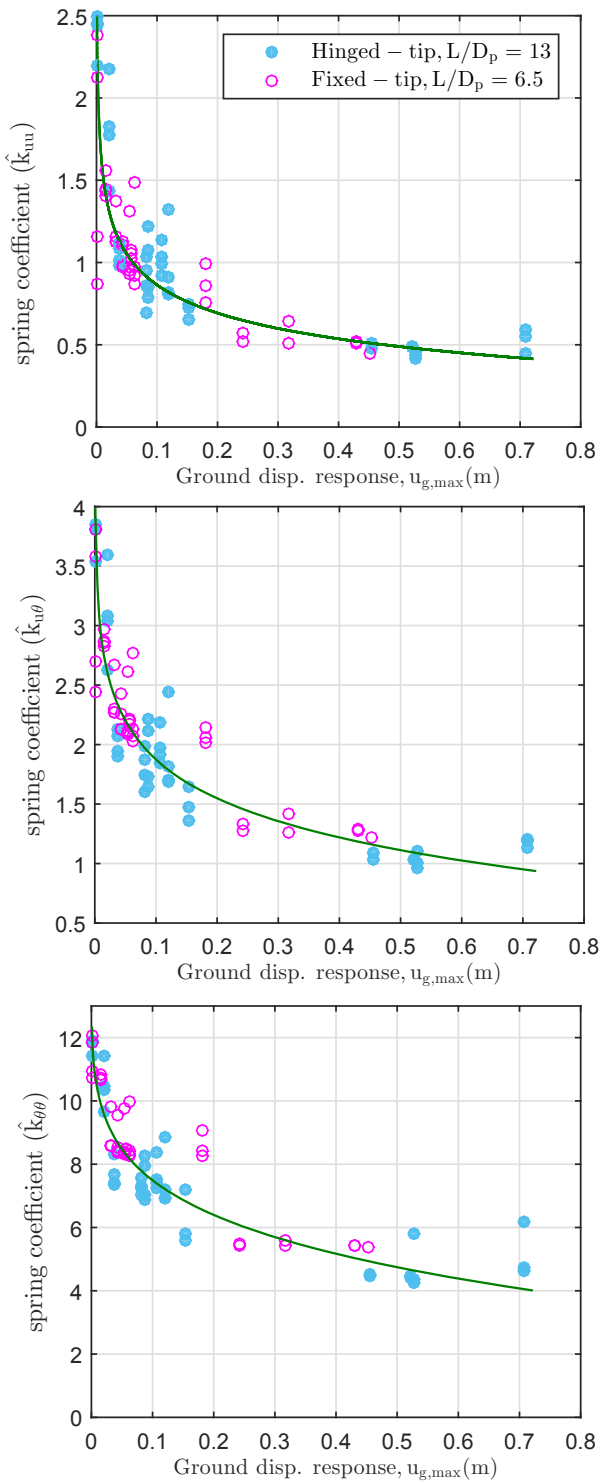

Figure 7.16. Variation of the average EL pile head stiffness of all the SPSI cases with maximum ground surface displacement

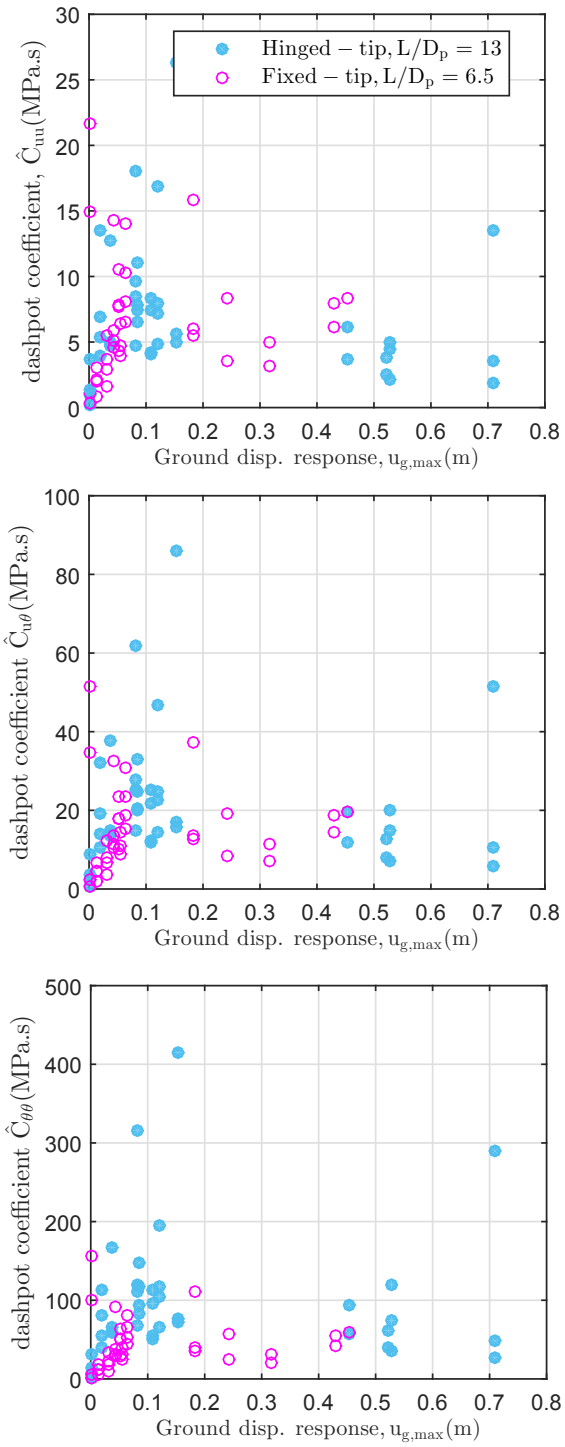

Figure 7.17. Variation of the average pile head dashpot coefficients of all the SPSI cases with maximum ground surface displacement

Chapter 8 : Summary, Conclusions and Recommendations for Future Research

8.1. Summary and Conclusions

In practice, seismic soil-structure interaction (SSI) analysis of pile supported bridges is commonly carried out using either the generic *p-y* curves whose accuracy has been seriously cast doubt, or the substructure method which requires dynamic soil-pile interaction properties (impedance functions). Current approaches for estimation of the pile head impedance functions are based on the linear elastic soil-pile interaction which is not adequate for inelastic interaction problems, or linearization of the *p-y* curves which is associated with serious uncertainties. On the other hand, although decent efforts have been devoted on SSI analysis of the RC shaft supported bridges using the beam-on-dynamic-Winkler-foundation (BDWF), there is a lack of fully nonlinear analysis using the high fidelity continuum modelling approach. Therefore, this thesis aims to overcome the

limitations of substructure method by developing a hybrid framework with the continuum modelling as the solution core. In the following, summary of the steps taken to achieve this goal along with the main findings are provided.

In Chapter 4, a procedure for calibration of dynamic strength properties of Leda Clay in eastern Canada was developed based on combination of geophysical and laboratory experiment results in order to provide a realistic soil deposit for seismic SSI analysis. This procedure mainly involved calibrating existing equations in literature, by relating the strength parameters to in-situ stress state and stress history of the soil. The calibrated equation for small-strain shear modulus was successfully verified by conducting site response analysis for a site with deep Leda Clay deposit. A series of relatively low-amplitude input and output ground motions, suitable for verification of small-strain soil response, were used for verification of the model. These motions were recorded at two nearby sites during the 2010 Val-des-Bois earthquake striking Ottawa area. The shear wave velocity profile given by the calibrated shear modulus equation was shown to be consistent with the velocity range obtained from field geophysical experiments.

Chapter 5 presented evaluation of the seismic response of a typical highway bridge supported by a reinforced concrete extended type II pile shaft in soft clay using a fully coupled nonlinear soil-pile-structure interaction analysis. The main goal was to evaluate seismic response of the bridge which is designed following current state of practice design procedures. This is accomplished by conducting three-dimensional numerical simulations of the soil-pile-structure system developed in the framework of OpenSees finite element program. The fully nonlinear analysis was performed by utilizing an elasto-plastic constitutive soil model for soft clay and the elasto-perfectly plastic contact elements which

allows for realistic simulation of the radiation damping as well as modulus of soil-pile interaction. The reliability of the finite element model in simulating nonlinear soil-structure interaction problems was successfully verified using two sets of centrifuge test results. A parametric study was also conducted to investigate effects of the SPSI phenomenon in two practical foundation cases involving short rock-socketed and long hinged-tip piles supporting four structural cases. Each case was subjected to a suite of twelve earthquake motions comprised of far-fault and near-fault ground motions. The free field soil curvature, structural drift ratio and bending moment profiles were used to evaluate performance of the system and design adequacy. The drift values indicated that except for very strong near-fault motions, majority of the cases experienced residual drifts less than the code-specified value. The excessive drift ratio is attributed to a significant shear failure at the boundary of soil stiffness contrast due to a long period velocity pulse existing in the time history of the near-fault motions. It was also shown that although the superstructure with deck-column kinematic constraint experiences in general lower level of the imposed drift, there might be cases with excessive residual drifts due to coincidence of the flexible-base period of the bridge with large spectral acceleration of the free field soil. The soil curvature was shown to be directly related to the transient drift through inducing the pile head rotation, and is the dominant factor in near fault ground motions. Finally, evaluation of bending moment profiles along the pile shaft indicated that the long-hinged tip pile is not susceptible to plastic hinge formation as the induced maximum bending moment of all input motions is 25% less than the plastic moment capacity of the pile shaft. On the other hand, in case of the short fixed-tip pile, a plastic hinge with lengths between 2-5m was shown to be developed in the pile shaft under moderate to strong near-fault motions. Hence, it can be

concluded that although socketed-pile shafts may excel in enhancing the displacement response of the structure and provide higher lateral pile capacity, their structural integrity is very likely to be endangered under strong near-fault motions due to nonlinear soil-pile interaction. Therefore, pile structural failure appears to be the dominant criterion in seismic design of the socketed shafts in seismically active regions.

Chapter 6 presented a hybrid numerical-analytical approach that was devised to compute the average equivalent-linear (EL) pile head impedance functions. The goal was to take the advantages of both the rigorous time-domain continuum SSI analysis and the frequency-domain substructure formulation in order to improve accuracy of the substructure analysis for inelastic SPSI problems. A new polynomial representation of the pile head impedance matrix in the Winkler viscoelastic medium was derived using the infinite series expansion in order to reduce functional complexities of existing impedance functions. The procedure of computing the EL impedances from the complex-valued equations was presented for two practical RC shaft cases under the controlled pile head and earthquake loadings.

Chapter 7 presented characterization of the inelastic pile head impedance functions which are derived following the hybrid approach proposed in Chapter 6. The equivalent-linear impedances were computed for the short rock-socketed and the long hinged-tip pile cases. A comprehensive characterization was conducted for elastic piles in a homogeneous soil deposit under the controlled static and dynamic pile head loadings of various amplitudes and frequencies in order to capture the coupling between the frequency-dependent and inelastic aspects of the impedances. In the last step, the proposed hybrid

approach was applied to results from the continuum analysis of kinematic and inertial SPSI due to passage of earthquake waves through the soil domain

Results from the static analyses indicate that the prediction residual of pile head lateral force by the hybrid method does not exceed 10% pile head displacement in both homogeneous and inhomogeneous soil deposits. Moreover, the normalized pile head stiffness degradation trends with increasing pile head displacement and their corresponding best-fit functional forms for the three displacement modes were developed, which can be used as a nonlinear force-deformation element in the substructure analysis.

Inelastic dynamic analysis using the sine sweep function at the pile head showed that inclusion of inelastic soil and interface (gapping) deformations significantly reduces the computed spectral stiffness and damping compared to those of fully elastic soil-pile model. The comprehensive dynamic characterization of the inelastic pile head impedances showed that due to relatively frequency-independent behaviour of the dynamic stiffness, the static degradation trend can be used as a reasonable average trend for the dynamic stiffness one. As for the damping component, the analyses revealed that two characteristic frequencies including the natural site frequency for combination of the waves and the frequency of the soil-pile characteristic wavenumber dominate the spectral damping values in the case of soil over a rigid bedrock. These frequencies were also shown to be the onset frequency of major radiation damping in the system. Furthermore, the dashpot coefficient was shown to be independent of frequency and inelasticity level from a moderate to high inelasticity level, and yields a constant value. This is indicative of a suppressed radiation damping due to plastic soil and interface deformation which reduce amount of energy emanating to the soil domain.

Finally, the hybrid method was also applied to the SPSI systems subjected to base earthquake excitations with a wide range of resulting free field ground displacement in order to recover the average EL impedances under the coupled kinematic and inertial interactions. The reliability evaluation of the computed impedances showed that varying flexural stiffness along the pile shaft due to stiffness degradation is the main uncertainty factor. Thus, it was shown that if an accurate pile stiffness is used in the back-calculation process, the pile head shear force and bending moment could be predicted by recovered impedances with a deviation range of $\pm 10\%$. The constructed dynamic subgrade stiffness degradation trend with the free field ground displacement revealed that the pile head inertial forces mainly govern the pile head stiffness degradation. In other words, the EL subgrade stiffness under strong near-fault motions is fairly insensitive to their large imposed ground displacements, and yields to a value corresponding to the design load in the static push over analysis. Thus, knowing the design factor of safety for lateral pile capacity can provide a measure for estimation of the ultimate EL subgrade stiffness for design SSI analysis. Because, it determines the relative magnitude of potential maximum inertial forces that are mobilized under design earthquake loads with respect to the ultimate lateral capacity of the pile.

8.2. Recommended Future Research

As explained, this thesis aimed to develop a fully inelastic continuum model of soil-pile-structure interaction for the RC shaft-supported bridges, and combine it in a hybrid framework to enhance accuracy of the substructure analysis for inelastic SPSI problems. While this research focused on the application of the proposed hybrid method for a limited

soil-pile cases, the followings are proposed as potential future research subjects on inelastic soil-pile interaction.

- To generalize the applicability of the stiffness degradation trends for use in substructure analysis, further study is needed using the proposed hybrid method to derive the trends for different soil-pile cases in end-bearing piles such as: various pile diameter and soil stiffness, which together determine design factor of safety, various level of soil deposit inhomogeneity and fixed head RC piles which are commonly used in practice for wide span bridges.
- The similar polynomial representation of the pile head impedance functions can be derived for frictional piles (floating pile) which are the foundation case where rigid bedrock is not available. The hybrid method can be applied to a group of frictional piles to investigate the group effect on the pile head impedances, which requires inelastic continuum modelling of the group pile under seismic and cyclic loadings.
- Performing static and cyclic field pile head loading experiments in lieu of the continuum models in order to provide more realistic pile head displacements and forces for use in the hybrid method. The computed impedances would reflect realistic pile head stiffness and damping which in turn can be compared with those from continuum models.

Bibliography

AASHTO. (2012). *LRFD Bridge Design Specifications*: American Association of State Highway and Transportation Officials, Washington D.C., USA.

Alavi, B., & Krawinkler, H. (2000). *Consideration of near-fault ground motion effects in seismic design.* Paper presented at the Proceedings of the 12th World Conference on Earthquake Engineering.

Anastasopoulos, I., Sakellariadis, L., & Agalianos, A. (2015). Seismic analysis of motorway bridges accounting for key structural components and nonlinear soil–structure interaction. *Soil Dynamics and Earthquake Engineering, 78*, 127-141.

API. (2007). *Recommended practice for planning, designing, and constructing fixed offshore platforms,* American Petroleum Institute. Section 6.8 Soil Reaction for Laterally Loaded Piles.

Badoni, D., & Makris, N. (1996). Nonlinear response of single piles under lateral inertial and seismic loads. *Soil Dynamics and Earthquake Engineering, 15*(1), 29-43.

Baker, J. W. (2007). Quantitative classification of near-fault ground motions using wavelet analysis. *Bulletin of the Seismological Society of America, 97*(5), 1486-1501.

Bathe, K.-J. (2007). Conserving energy and momentum in nonlinear dynamics: a simple implicit time integration scheme. *Computers & structures, 85*(7), 437-445.

Bertero, V. V., Mahin, S. A., & Herrera, R. A. (1978). Aseismic design implications of near□fault San Fernando earthquake records. *Earthquake Engineering & Structural Dynamics, 6*(1), 31-42.

Bielak, J., Loukakis, K., Hisada, Y., & Yoshimura, C. (2003). Domain reduction method for three-dimensional earthquake modeling in localized regions, Part I: Theory. *Bulletin of the Seismological Society of America, 93*(2), 817-824.

Blaney, G. W., Kausel, E., and Roesset, J. M. (1976). *Dynamic Stiffness of Piles*. Paper presented at the Second International Conference on Numerical Methods in Geomechanics, Vol. II, Virginia Polytechnic Institute and State University, Blacksburg, Va., June, 1976, pp. 1001-1012.

Boulanger, R. W., Curras, C. J., Kutter, B. L., Wilson, D. W., & Abghari, A. (1999). Seismic soil-pile-structure interaction experiments and analyses. *Journal of Geotechnical and Geoenvironmental Engineering, 125*(9), 750-759.

Brandenberg, S. J., Boulanger, R. W., Kutter, B. L., & Chang, D. (2007). Static pushover analyses of pile groups in liquefied and laterally spreading ground in centrifuge tests. *Journal of Geotechnical and Geoenvironmental Engineering, 133*(9), 1055-1066.

Canadian Foundation Engieering Manual (CFEM) (2006). *Section 18.5 Lateral Pile Deflections*.

Caltrans. (2013). *Seismic Design Criteria, version 1.7,* California Department of Transportation.

Cheng, Z., & Jeremić, B. (2009). Numerical modeling and simulation of pile in liquefiable soil. *Soil Dynamics and Earthquake Engineering, 29*(11), 1405-1416.

Cox, W. R., Reese, L. C., & Grubbs, B. R. (1974). *Field testing of laterally loaded piles in sand.* Paper presented at the Offshore Technology Conference.

Crawford, C. (1961). Engineering studies of Leda clay. *Soils in Canada: Royal Society of Canada Special Publication, 3*, 200-217.

Crow, H., Hunter, J., & Motazedian, D. (2011). Monofrequency in situ damping measurements in Ottawa area soft soils. *Soil Dynamics and Earthquake Engineering, 31*(12), 1669-1677.

Curras, C. J., Boulanger, R. W., Kutter, B. L., & Wilson, D. W. (2001). Dynamic experiments and analyses of a pile-group-supported structure. *Journal of Geotechnical and Geoenvironmental Engineering, 127*(7), 585-596.

Dafalias, Y., & Popov, E. (1975). A model of nonlinearly hardening materials for complex loading. *Acta mechanica, 21*(3), 173-192.

Dafalias, Y. F., & Manzari, M. T. (2004). Simple plasticity sand model accounting for fabric change effects. *Journal of Engineering mechanics, 130*(6), 622-634.

Darendeli, M. B. (2001) Development of a new family of normalized modulus reduction and material damping curves. PhD Thesis, Univ. of Texas at Austin, Austin, Texas.

DEEPSOIL V.6.1. Computer Software for Seismic Site Response analysis, Univ. of Illinois at Urbana-Champaign. http://deepsoil.cee.illinois.edu.

Demers, D., & Leroueil, S. (2002). Evaluation of preconsolidation pressure and the overconsolidation ratio from piezocone tests of clay deposits in Quebec. *Canadian Geotechnical Journal, 39*(1), 174-192.

Dickenson, S. E. (1994). *Dynamic response of soft and deep cohesive soils during the Loma Prieta earthquake of October 17, 1989.* (PhD Thesis), University of California, Berkeley.

Dobry, R., Vicente, E., O'Rourke, M., & Roesset, M. (1982). Horizontal stiffness and damping of single piles. *Journal of Geotechnical and Geoenvironmental Engineering, 108*(GT3).

D'ONOFRIO, A., Silvestri, F., & Vinale, F. (1999). Strain rate dependent behaviour of a natural stiff clay. *Soils and foundations, 39*(2), 69-82.

El Naggar, M., & Novak, M. (1995). Nonlinear lateral interaction in pile dynamics. *Soil Dynamics and Earthquake Engineering, 14*(2), 141-157.

Elgamal, A., Yan, L., Yang, Z., & Conte, J. P. (2008). Three-dimensional seismic response of Humboldt Bay bridge-foundation-ground system. *Journal of Structural Engineering, 134*(7), 1165-1176.

Elgamal, A., Yang, Z., Parra, E., & Ragheb, A. (2003). Modeling of cyclic mobility in saturated cohesionless soils. *International Journal of Plasticity, 19*(6), 883-905.

Fan, K. (1992). *Seismic response of pile foundations evaluated through case histories.* (PhD Thesis), State University of New York at Buffalo.

Finn, W. L. (2005). A study of piles during earthquakes: issues of design and analysis. *Bulletin of Earthquake Engineering, 3*(2), 141-234.

Gazetas, G. (1983). Analysis of machine foundation vibrations: state of the art. *International Journal of Soil Dynamics and Earthquake Engineering, 2*(1), 2-42.

Gazetas, G. (1984). Seismic response of end-bearing single piles. *International Journal of Soil Dynamics and Earthquake Engineering, 3*(2), 82-93.

Gazetas, G., & Dobry, R. (1984). Simple radiation damping model for piles and footings. *Journal of Engineering mechanics, 110*(6), 937-956.

Gazioglu, S. M., & O'Neill, M. (1984). *Evaluation of p-y relationships in cohesive soils*. Analysis and design of pile foundations, 192-213.

Gerolymos, N., & Gazetas, G. (2005). Phenomenological model applied to inelastic response of soil-pile interaction systems. *Soils and foundations, 45*(4), 119-132.

Gu, Q., Conte, J., Yang, Z., & Elgamal, A. (2011). Consistent tangent moduli for multi-yield-surface J2 plasticity model. *Computational Mechanics, 48*(1), 97-120.

Hardin, B. O., & Drnevich, V. P. (1972). Shear modulus and damping in soils: measurement and parameter effects. *Journal of Soil Mechanics & Foundations Div, 98*(sm6).

Hilber, H. M., Hughes, T. J., & Taylor, R. L. (1977). Improved numerical dissipation for time integration algorithms in structural dynamics. *Earthquake Engineering & Structural Dynamics, 5*(3), 283-292.

Hunter, J. A., Burn, R. A., Good, R.L., Aylsworth, J.M., Pullan, S.E., Perret, D., and Douma, M. (2007). *Borehole Shear Wave Velocity Measurements of Champlain Sea Sediments in the Ottawa-Montreal Region.* Open File 5345, Geological Survey of Canada.

Hutchinson, T., Boulanger, R., Chai, Y., & Idriss, I. (2004). *Inelastic seismic response of extended pile shaft supported bridge structures*. Report PEER 2002/14, Pacific Earthquake Engineering Research Center. University of California, Berkeley.

IIankatharan, M. (2008). *Centirfuge Modeling of Soil-Pile-Bridge Systems with Numerical Simulations Accounting for Soil-Container-Shaker Interaction.* (PhD thesis), University of California, Davis.

Japanese Road Association (JRA) (1996). *Design Specifications of Highway Bridges. Part V: Seismic Design*. Tokyo, Japan.

Jeremic, B., Jie, G., Preisig, M., & Tafazzoli, N. (2009). Time domain simulation of soil-foundation-structure interaction in non-uniform soils. *Earthquake Engineering & Structural Dynamics, 38*(5), 699.

Jeremić, B., Kunnath, S., & Xiong, F. (2004). Influence of soil–foundation–structure interaction on seismic response of the I-880 viaduct. *Engineering Structures, 26*(3), 391-402.

Joyner, W. B., & Chen, A. T. (1975). Calculation of nonlinear ground response in earthquakes. *Bulletin of the Seismological Society of America, 65*(5), 1315-1336.

Kagawa, T., & Kraft, L. M. (1980). Lateral load-deflection relationships of piles subjected to dynamic loadings. *Soils and foundations, 20*(4), 19-36.

Kagawa, T., & Kraft, L. M. (1981). Dynamic characteristics of lateral load□deflection relationships of flexible piles. *Earthquake Engineering & Structural Dynamics, 9*(1), 53-68.

Kausel, E. (2010). Early history of soil–structure interaction. *Soil Dynamics and Earthquake Engineering, 30*(9), 822-832.

Kausel, E., Whitman, R. V., Morray, J. P., & Elsabee, F. (1978). The spring method for embedded foundations. *Nuclear Engineering and Design, 48*(2), 377-392.

Kaynia, A. M. (1982). *Dynamic stiffness and seismic response of pile groups.* (PhD Thesis), Massachusetts Institute of Technology.

Khaheshi Banab, K., Kolaj, M., Motazedian, D., Sivathayalan, S., Hunter, J. A., Crow, H. L., Pugin, J-M.A., Brooks G.R., Pyne, M. (2012). Seismic site response analysis for Ottawa, Canada: A comprehensive study using measurements and numerical simulations. *Bulletin of the Seismological Society of America, 102*(5), 1976-1993.

Kokusho, T., Yoshida, Y., Esashi, Y. (1982). Dynamic properties of soft clay for wide strain range. *Soils and foundations, 22*(4), 1-18.

Kondner, R. L. (1963). Hyperbolic stress-strain response: cohesive soils. *Journal of the soil mechanics and foundations division, ASCE, 89*(1), 115-143.

Kramer, S. L. (1996). *Geotechnical earthquake engineering*: Prentice Hall, Englewood Cliffs, N.J.

Kwok, A. O., Stewart, J. P., Hashash, Y. M., Matasovic, N., Pyke, R., Wang, Z., & Yang, Z. (2007). Use of exact solutions of wave propagation problems to guide implementation of nonlinear seismic ground response analysis procedures. *Journal of Geotechnical and Geoenvironmental Engineering, 133*(11), 1385-1398.

Kwon, O.-S., & Elnashai, A. S. (2008). Seismic analysis of meloland road overcrossing using multiplatform simulation software including SSI. *Journal of Structural Engineering, 134*(4), 651-660.

Ladd, C. C. (1991). Stability evaluation during staged construction. *Journal of Geotechnical Engineering, 117*(4), 540-615.

Lam, I. P., Law, H. K., & Martin, G. R. (2007). *Bridge Foundations: Modeling Large Pile Groups and Caissons for Seismic Design*. Retrieved from

Lefebvre, G., Bozozuk, M., Philibert, A., & Hornych, P. (1991). Evaluating K o in Champlain clays with hydraulic fracture tests. *Canadian Geotechnical Journal, 28*(3), 365-377.

Lefebvre, G., & Pfendler, P. (1996). Strain rate and preshear effects in cyclic resistance of soft clay. *Journal of Geotechnical Engineering, 122*(1), 21-26.

Leroueil, S., Tavenas, F., Samson, L., & Morin, P. (1983). Preconsolidation pressure of Champlain clays. Part II. Laboratory determination. *Canadian Geotechnical Journal, 20*(4), 803-816.

Ljung, L. (1987). *System Identification: Theory for the user*: Prentice Hall, Englewood Cliffs, NJ.

Makris, N., Badoni, D., Delis, E., & Gazetas, G. (1994). Prediction of observed bridge response with soil-pile-structure interaction. *Journal of Structural Engineering, 120*(10), 2992-3011.

Mander, J. B., Priestley, M. J., & Park, R. (1988). Theoretical stress-strain model for confined concrete. *Journal of Structural Engineering, 114*(8), 1804-1826.

Manzari, M. T., & Dafalias, Y. F. (1997). A critical state two-surface plasticity model for sands. *Géotechnique, 47*(2), 255-272.

Margason, E. (1975). *Pile bending during earthquakes*. Paper presented at the Lecture ASCE/UC-Berkeley seminar on design construction & performance of deep foundations.

Matlock, H. (1970). *Correlations for design of laterally loaded piles in soft clay*. Offshore Technology in Civil Engineering's Hall of Fame Papers from the Early Years, 77-94.

Matlock, H., & Foo, S. H. (1978). *Simulation of lateral pile behavior under earthquake motion.* Paper presented at the From Volume I of Earthquake Engineering and Soil Dynamics--Proceedings of the ASCE Geotechnical Engineering Division Specialty Conference, June 19-21, 1978, Pasadena, California. Sponsored by Geotechnical Engineering Division of ASCE in cooperation with:.

McClelland, B. (1956). Soil modulus for laterally loaded piles. *Journal of the Soil Mechanics and Foundations division, 82*(4), 1-22.

McKenna, F. a. F., G. (2001). *The OpenSees command language manual, Version 1.2*: Pacific Earthquake Engineering Research Center, University of California, Berkeley, CA. http://opensees.berkeley.edu.

Mitchell, R. J. (1970). On the yielding and mechanical strength of Leda clays. *Canadian Geotechnical Journal, 7*(3), 297-312.

Mroz, Z. (1967). On the description of anisotropic workhardening. *Journal of the Mechanics and Physics of Solids, 15*(3), 163-175.

Murchison, J. M., & O'Neill, M. W. (1984). *Evaluation of py relationships in cohesionless soils.* Paper presented at the Analysis and design of pile foundations.

Mylonakis, G. (1995). *Contributions to static and seismic analysis of piles and pile-supported bridge piers.* (PhD Thesis), State University of New York at Buffalo.

Mylonakis, G., & Gazetas, G. (1999). Lateral vibration and internal forces of grouped piles in layered soil. *Journal of Geotechnical and Geoenvironmental Engineering, 125*(1), 16-25.

Mylonakis, G., & Gazetas, G. (2000). Seismic soil-structure interaction: beneficial or detrimental? *Journal of Earthquake Engineering, 4*(03), 277-301.

Mylonakis, G., Nikolaou, A., & Gazetas, G. (1997). Soil-pile-bridge seismic interaction: kinematic and inertial effects. Part I: soft soil. *Earthquake Engineering & Structural Dynamics, 26*(3), 337-359.

Mylonakis, G., Syngros, C., Gazetas, G., & Tazoh, T. (2006). The role of soil in the collapse of 18 piers of Hanshin Expressway in the Kobe earthquake. *Earthquake Engineering & Structural Dynamics, 35*(5), 547-575.

N. NIST. Soil-Structure-Interaction for Building Structures (NIST GCR 12-917-21). National Institute of Standards and Technology, Gaithersburg, MD 20899, September 2012.

Nogami, T., & Konagai, K. (1988). Time domain flexural response of dynamically loaded single piles. *Journal of Engineering mechanics, 114*(9), 1512-1525.

Nogami, T., Otani, J., Konagai, K., & Chen, H.-L. (1992). Nonlinear soil-pile interaction model for dynamic lateral motion. *Journal of Geotechnical Engineering, 118*(1), 89-106.

Novak, M. (1974). Dynamic stiffness and damping of piles. *Canadian Geotechnical Journal, 11*(4), 574-598.

Novak, M., & Nogami, T. (1977). Soil□pile interaction in horizontal vibration. *Earthquake Engineering & Structural Dynamics, 5*(3), 263-281.

Pandit, S. M. (1991). *Modal and spectrum analysis: data dependent systems in state space*: Wiley, New York.

Parra-Colmenares, E. J. (1996). *Numerical modeling of liquefaction and lateral ground deformation including cyclic mobility and dilation response in soil systems.* (PhD Thesis), Dept. of Civil Engineering, Rensselaer Polytechnic Institute, Troy, NY.

Pender, M. (1993). Aseismic pile foundation design analysis. *Bulletin of the New Zealand National Society for Earthquake Engineering, 26*(1), 49-160.

Petek, K. A. (2006). *Development and application of mixed beam-solid models for analysis of soil-pile interaction problems.* (PhD Thesis), University of Washington.

Prevost, J. (1978). Plasticity theory for soil stress-strain behavior. *Journal of the Engineering Mechanics Division, 104*(5), 1177-1194.

Prevost, J. H. (1985). A simple plasticity theory for frictional cohesionless soils. *International Journal of Soil Dynamics and Earthquake Engineering, 4*(1), 9-17.

Prévost, J. H. (1977). Mathematical modelling of monotonic and cyclic undrained clay behaviour. *International Journal for Numerical and Analytical Methods in Geomechanics, 1*(2), 195-216.

Quigley, R. M., Gwyn, Q., White, O. L., Rowe, R. K., Haynes, J. E., & Bohdanowicz, A. (1983). Leda clay from deep boreholes at Hawkesbury, Ontario. Part I: Geology and geotechnique. *Canadian Geotechnical Journal, 20*(2), 288-298.

Rahmani, A., Taiebat, M., Finn, W. L., & Ventura, C. E. (2016). Evaluation of substructuring method for seismic soil-structure interaction analysis of bridges. *Soil Dynamics and Earthquake Engineering, 90*, 112-127.

Rasmussen, K. K. (2012). *An Investigation of Monotonic and Cyclic Behaviour of Leda Clay.* (M.Sc. Thesis), The University of Western Ontario.

Rathje, E. M., Abrahamson, N. A., & Bray, J. D. (1998). Simplified frequency content estimates of earthquake ground motions. *Journal of Geotechnical and Geoenvironmental Engineering, 124*(2), 150-159.

Rayhani, M., & El Naggar, M. (2007). Centrifuge modeling of seismic response of layered soft clay. *Bulletin of Earthquake Engineering, 5*(4), 571-589.

Reece, L., Cox, W., & Koop, F. (1975). *Field testing and analysis of laterally loaded piles in stiff clay.* Paper presented at the 7th offshore technology conference.

Reese, L. C., & Welch, R. C. (1975). Lateral Loading of Deep Foundations in Stiff Clay. *Journal of the Geotechnical Engineering Division, 101*(7), 633-649.

Roesset, J. M. (1980). *Stiffness and Damping Coefficients of Foundations*. Paper presented at the Special Technical Publication on Dynamic Response of Pile Foundations: Analytical Aspects, ASCE, O'Neill and Dobry.

Schmidt, B. (1966). Earth pressures at rest related to stress history. *Canadian Geotechnical Journal, 3*(4), 239-242.

Sheahan, T. C., Ladd, C. C., & Germaine, J. T. (1996). Rate-dependent undrained shear behavior of saturated clay. *Journal of Geotechnical Engineering, 122*(2), 99-108.

Soga, K. (1994). *Mechanical behavior and constitutive modelling of natural structured soils.* (PhD Thesis), University of California, Berkeley.

Song, S., Chai, Y., & Budek, A. (2006). Methodology for preliminary seismic design of extended pile shafts for bridge structures. *Earthquake Engineering & Structural Dynamics, 35*(14), 1721-1738.

Stokoe, K. H., Darendeli M.B., Menq F.Y. (1998). *Summary of laboratory test results, ROSRINE data dissemination workshop*. Paper presented at the University of Southern California, Los Angeles, CA, 15th December, p 129.

Syngros, K. C. (2004). *Seismic response of piles and pile-supported bridge piers evaluated through case histories.* (PhD Thesis), The City University of New York.

Taciroglu, E., Rha, C., & Wallace, J. W. (2006). A robust macroelement model for soil–pile interaction under cyclic loads. *Journal of Geotechnical and Geoenvironmental Engineering, 132*(10), 1304-1314.

Torabi, H., & Rayhani, M. T. (2014). Three dimensional Finite Element modeling of seismic soil–structure interaction in soft soil. *Computers and Geotechnics, 60*, 9-19.

Trochanis, A. M., Bielak, J., & Christiano, P. (1991). Three-dimensional nonlinear study of piles. *Journal of Geotechnical Engineering, 117*(3), 429-447.

Vaid, Y., Robertson, P., & Campanella, R. (1979). Strain rate behaviour of Saint-Jean-Vianney clay. *Canadian Geotechnical Journal, 16*(1), 34-42.

Varun, Assimaki, D., & Gazetas, G. (2009). A simplified model for lateral response of large diameter caisson foundations—Linear elastic formulation. *Soil Dynamics and Earthquake Engineering, 29*(2), 268-291.

Viggiani, G., & Atkinson, J. (1995). Stiffness of fine-grained soil at very small strains. *Géotechnique, 45*(2), 249-265.

Wang, S., Kutter, B. L., Chacko, M. J., Wilson, D. W., Boulanger, R. W., & Abghari, A. (1998). Nonlinear seismic soil-pile structure interaction. *Earthquake spectra, 14*(2), 377-396.

Wilson, D. W. (1998). *Soil-pile-superstructure interaction in liquefying sand and soft clay.* (PhD Thesis), University of California, Davis.

Wolf, J. P. (1985). *Dynamic soil-structure interaction*: Prentice Hall, Englewood Cliffs, N.J.

Wolf, J. P. (1989). Soil-structure-interaction analysis in time domain. *Nuclear Engineering and Design, 111*(3), 381-393.

Yamada, S., Hyodo, M., Orense, R. P., & Dinesh, S. (2008). Initial shear modulus of remolded sand-clay mixtures. *Journal of Geotechnical and Geoenvironmental Engineering, 134*(7), 960-971.

Yang, Z., Elgamal, A., & Parra, E. (2003). Computational model for cyclic mobility and associated shear deformation. *Journal of Geotechnical and Geoenvironmental Engineering, 129*(12), 1119-1127.

Yoshimura, C., Bielak, J., Hisada, Y., & Fernández, A. (2003). Domain reduction method for three-dimensional earthquake modeling in localized regions, part II: Verification and applications. *Bulletin of the Seismological Society of America, 93*(2), 825-841.

Zafir, Z. (2002). *Seismic Foundation Stiffness For Bridges.* Paper presented at the Deep Foundations 2002: An International Perspective on Theory, Design, Construction, and Performance.

Zhang, J., & Makris, N. (2002). Kinematic response functions and dynamic stiffnesses of bridge embankments. *Earthquake Engineering & Structural Dynamics, 31*(11), 1933-1966.

Appendix A: Derivation of Closed-form Pile Head Impedance Functions

In this section, the sample procedures for derivation of the closed-form pile head impedance functions are presented. The derivation is based on closed-from simultaneous solution of the force-deformation matrix for two sets of boundary condition at the pile head, which include unit displacement due to pure horizontal lateral force and unit rotation due to pure bending moment at the pile head. Derivation begins with the solution for dynamic equilibrium differential equation of beam on viscoelastic Winkler medium for only the pile head loading:

$$u(z) = e^{\lambda z}(A_1 \cos(\lambda z) + A_2 \sin(\lambda z)) + e^{-\lambda z}(A_3 \cos(\lambda z) + A_4 \sin(\lambda z)) \tag{A.1}$$

$$\theta(z) = \frac{\partial u}{\partial z} = \lambda \begin{bmatrix} e^{\lambda z}[A_1(\cos(\lambda z) - \sin(\lambda z)) + A_2(\cos(\lambda z) + \sin(\lambda z))] \\ -e^{-\lambda z}[A_3(\cos(\lambda z) + \sin(\lambda z)) - A_4(\cos(\lambda z) - \sin(\lambda z))] \end{bmatrix} \tag{A.2}$$

$$M(z) = -E_p I_p \frac{\partial u^2}{\partial z^2} = 2\lambda^2 \begin{bmatrix} +e^{\lambda z}\left[A_1 \sin(\lambda z) - A_2 \cos(\lambda z)\right] \\ -e^{-\lambda z}\left[A_3 \sin(\lambda z) - A_4 \cos(\lambda z)\right] \end{bmatrix} \tag{A.3}$$

$$V(z) = -E_p I_p \frac{\partial u^3}{\partial z^3} = 2\lambda^3 \begin{bmatrix} +e^{\lambda z}[A_1(\cos(\lambda z) + \sin(\lambda z)) - A_2(\cos(\lambda z) - \sin(\lambda z))] \\ -e^{-\lambda z}[A_3(\cos(\lambda z) - \sin(\lambda z)) + A_4(\cos(\lambda z) + \sin(\lambda z))] \end{bmatrix} \tag{A.4}$$

A.1. Free head, hinged-tip pile:

For the case of pure horizontal force at the pile head, the force-deformation equilibrium is:

$$\begin{bmatrix} S_{uu} & S_{u\theta} \\ S_{u\theta} & S_{\theta\theta} \end{bmatrix} \begin{Bmatrix} u_{0,F} \\ \theta_{0,F} \end{Bmatrix} = \begin{Bmatrix} V_{0,F} \\ M_{0,F} \end{Bmatrix} \tag{A.5}$$

where,

$$u_{0,F} = 1 \text{ , } V_{0,F} = -E_p I_p \frac{\partial u^3}{\partial z^3}\Big|_{z=0} \text{ , } \theta_{0,F} = \frac{\partial u}{\partial z}\Big|_{z=0} \text{ , } M_{0,F} = 0 \tag{A.6}$$

$$u(z = L) = 0 \text{ , } M(z = L) = 0$$

Applying the above boundary conditions to Eq.A1-A5 and simplifying them yield to:

$$S_{uu} - S_{\theta\theta}\theta_{0,F}^2 = V_{0,F} \tag{A.7}$$

$$\theta_{0,F} = \lambda(2A_1 + 2A_2 - 1) \tag{A.8}$$

$$V_{0,F} = 2E_p I_p \lambda^3 \left(2A_2 - 2A_1 + 1\right) \tag{A.9}$$

where,

$$\theta_{0,F} = \lambda \frac{\sinh(2\lambda L) + \sin(2\lambda L)}{\cos(2\lambda L) - \cosh(2\lambda L)} \tag{A.10}$$

$$V_{0,F} = 2E_p I_p \lambda^3 \frac{\sin(2\lambda L) - \sinh(2\lambda L)}{\cos(2\lambda L) - \cosh(2\lambda L)} \tag{A.11}$$

Similarly, the force-deformation equilibrium of Eq.A.5 is considered for the case of pure bending moment and resultant unit rotation with the following boundary conditions:

$$V_{0,M} = 0 \ , \ \theta_{0,M} = 1 \ , \ M_{0,M} = -E_p I_p \frac{\partial u^2}{\partial z^2}\Big|_{z=0} \tag{A.12}$$

$$u(z = L) = 0 \ , \ M(z = L) = 0$$

Again, applying the boundary conditions of Eq. A.1-A5 to Eqs. A.1 and A.2:

$$S_{\theta\theta} - S_{uu} u_{0,M}^2 = M_{0,M} \tag{A.13}$$

$$u_{0,M} = A_1 + A_3 \tag{A.14}$$

$$M_{0,M} = 2E_p I_p \lambda^2 \left(A_2 - A_4 \right) \tag{A.15}$$

where,

$$u_{0,M} = \frac{1}{2\lambda} \frac{\sinh(2\lambda L) + \sin(2\lambda L)}{\cos(2\lambda L) + \cosh(2\lambda L)} \tag{A.16}$$

$$M_{0,M} = E_p I_p \lambda \frac{-\sin(2\lambda L) + \sinh(2\lambda L)}{\cos(2\lambda L) + \cosh(2\lambda L)} \tag{A.17}$$

Finally, solving Eq. A.7 and Eq. A.13 simultaneously yields to:

$$S_{uu} = \frac{V_{0,F} + M_{0,M} \theta_{0,F}^2}{1 - u_{0,M}^2 \theta_{0,F}^2} \tag{A.18}$$

and substituting the functional forms of the parameters in Eq. A.18, the impedance functions for the horizontal mode becomes:

$$S_{uu} = 4E_p I_p \lambda^3 \frac{\cos(2\lambda L) + \cosh(2\lambda L)}{-\sin(2\lambda L) + \sinh(2\lambda L)} \tag{A.19}$$

The rocking and cross-coupling impedances can be determined readily by inserting the above horizontal impedance and Eqs. A.16, A.17, A.8 in Eqs A.13 and A.5.

A.2. Fixed-head, hinged-tip pile:

In this case, the boundary condition of pure horizontal force and its resultant unit displacement is enough to derive impedance function matrix. Thus, the force-deformation matrix of Eq. A.5 must be solved for the following boundary conditions:

$$u_{0,F} = 1 \ , \ V_{0,F} = -E_p I_p \frac{\partial u^3}{\partial z^3}\Big|_{z=0} \ , \ \theta_{0,F} = 0 \tag{A.20}$$

$$u(z = L) = 0 \ , \ M(z = L) = 0$$

Applying the above boundary conditions to Eq.A1-A5 and simplifying them yield to:

$$S_{uu} = V_{0,F} \tag{A.21}$$

$$\theta_{0,F} = \lambda(2A_1 + A_2 + A_4 - 1) \tag{A.22}$$

$$V_{0,F} = 4E_p I_p \lambda^3 \left(1 - 2A_1\right) \tag{A.23}$$

where,

$$A_1 = \frac{e^{2\lambda L}\sin(2\lambda L) + e^{-\lambda L} + e^{\lambda L}\cos(2\lambda L)}{2e^{\lambda L}\sin(2\lambda L) + e^{-\lambda L} - e^{3\lambda L}} \tag{A.24}$$

Substituting Eq.A.24 into Eq.A.23 yields to:

$$S_{uu} = 4E_p I_p \lambda^3 \frac{\cos(2\lambda L) + \cosh(2\lambda L)}{-\sin(2\lambda L) + \sinh(2\lambda L)} \tag{A.25}$$

which is similar to the horizontal impedance of the free head pile. Thus, it can be concluded that the pile head impedance functions do not depend on the pile head boundary conditions and are controlled by the ones at the pile tip.